Université du Québec
à Rimouski

INFLUENCE DE LA VARIABILITÉ SPATIALE DES PROPRIÉTÉS MÉCANIQUES DE LA NEIGE SUR LE DÉCLENCHEMENT D'AVALANCHE

Thèse présentée

dans le cadre du programme de Doctorat sur mesure en Géographie - Science de la Neige

en vue de l'obtention du grade de Philosophiae Doctor (Ph.D.)

PAR

©FRANCIS MELOCHE

Septembre 2024

Composition du jury :

Alexandre Roy, président du jury, Université du Québec à Trois-Rivières

Francis Gauthier, directeur de recherche, Université du Québec à Rimouski

Alexandre Langlois, codirecteur de recherche, Université de Sherbrooke

Johan Gaume, collaborateur, École polytechnique fédérale de Zürich ETHZ

Alec van Herwijnen, examinateur externe, Institut fédérale de recherche sur la neige et les avalanche SLF

Dépôt initial le 21 mars 2024 Dépôt final le 5 septembre 2024

À mes parents qui m'ont transmis la curiosité et l'amour de la neige, merci.

REMERCIEMENTS

J'aimerais commencer par remercier ceux qui sont là depuis le tout début, mes parents. Cela peut sembler banal mais vous n'avez jamais mentionné le moindre doute sur mon choix de carrière de faire de la recherche en Géographie. Il y a souvent du doute et un syndrome d'imposteur qui s'installent lorsqu'on fait une thèse de doctorat, votre support inconditionnel en tant que parent a fait une énorme différence et je vous en remercie. J'aimerais remercier mon directeur de recherche Francis Gauthier, tu as vu au-delà de mon dossier académique et a cru en ma curiosité et ma passion et je t'en remercie. Je sais que parfois tu as le rôle du méchant quand tu corriges mes articles et que tu trouves cela difficile, mais je sais qu'au final tu as toujours fait cela pour m'aider à m'améliorer et tu es en grande partie responsable du scientifique je suis devenue aujourd'hui. Je remercie également mon co-directeur Alexandre Langlois avec qui j'ai partagé de nombreuses campagnes de terrain mémorables. Je me sentais parfois seul à travailler sur la neige à l'UQAR, mais tu m'as toujours fait sentir comme un membre de ton équipe à Sherbrooke et cela me touche énormément. J'aimerais remercie un autre "co-directeur non-officiel" Johan Gaume, je n'aurais jamais pensé que j'aurais travaillé avec toi lorsque j'ai commencé ma thèse. C'était un rêve scientifique de venir travailler à Lausanne et à Davos. Il a souvent fallu que je me pince pour réaliser que j'étais bien à Lausanne à travailler avec ton équipe. J'en dois une à Francis là-dessus car c'est toi qui m'a poussé à écrire à Johan au départ. Ce stage doctoral a complètement changé ma vie dans plusieurs sphères, tant scientifique que personnel. J'en profite également pour remercier les membres de *SLAB* à Lausanne et d'*ALMO* à Davos, notamment, Louis Guillet, Lars Blatny, Bertil trottet, Hugo Rousseau, Thomas Pauze et Roxanne Fayant, Grégoire Bobillier, Michi Kyburz, Camille Huitorel, Philipp Friess, Lara Roffmann et Hervé Vicari. Vous m'avez accueillie dans votre équipe de "matheux" sans aucun jugement et répondue à mes innombrables questions. Je me souviendrais toujours d'une phrase qui m'a rendu pas mal fier «Pour un géographe... tu fais pas mal de math». J'aimerais également remercier tous mes collègues du LGGRM à Rimouski, notamment Tom Birien, François Truchon, Benjamin Imbach, Matteo Arnaldi et

Jacob Laliberté qui m'ont aidé sur de nombreuses campagnes de terrain en Gaspésie, mais également les autres collègues au labo Alexi, Yan, Chloé, Corentin, Julie, Natalie, Jeanne, Lancelot, Félix, Marie-Pier et Clara. Une mention spéciale à mon éternel collègues Tom Birien, avec qui nous avons commencé au stade de nouveaux étudiants à la maîtrise jusqu'à être des vieux meubles du labo qui ont subi 6 déménagements de bureaux à l'UQAR. Nos nombreuses discussions sur la vie et nos recherches m'ont toujours fait plaisir et motivé à continuer dans des moments difficiles. Je remercie aussi tous les collègues du *GRIMP* à Sherbrooke, le *avalanche crew*, Jean-Benoit Madore, Paul Billecocq, Alex Blanchette, Antoine Rolland et William Durand. J'ai partagé avec vous des campagnes de terrain mémorables au BC. Je vous remercie d'avoir donner votre maximum pour mes manips difficiles à Fidelity, et les petites *hit the deck* sur la terrasse. Je veux faire une mention spéciale à mon frère jumeau Julien Meloche, alumni du GRIMP, ce fût un plaisir de partager avec toi notre expérience de thèse de doctorat, on a pu faire des terrains et une conférence ensemble. Je me sens priviliégié d'avoir pu partager ces moments avec toi et de pouvoir t'appeler pour des conseils. Je remercie également tous mes amis qui m'ont fait décrocher pendant cette thèse et surtout montrer qu'il y a autre chose dans la vie que la variabilité spatiale de la neige, merci à J-C, Jacob, Éli, Vince, Félix, Alexi, Imbo, Cod, Jérôme, Denys, Louis et Chuck. Je termine en remerciant mon amoureuse et partenaire de vie, Laura, ton support a fait la différence et partager cela avec toi me remplit de bonheur. Merci à tous.

AVANT-PROPOS

Ce sujet scientifique m'habitait depuis déjà plusieurs années avant le début de cette thèse. Je raconte donc dans cette section ma petite histoire sur ce sujet qui est devenu mon projet de doctorat. C'est lors de mon cours *niveau 1 professionnel opération avalanche* de l'Association Canadienne des Avalanches qu'une question m'est venu à l'esprit : Comment la stabilité est influencée la variabilité spatiale de la neige ? Je ne pouvais pas concevoir que mes collègues de classe à 5 m à coté de moi avait un *snowpit* complètement différent du mien. J'étais comme on dit par chez nous "hooké" par cette question scientifique. J'étais en deuxième année de baccalauréat en géographie et je convoitais déjà faire une maîtrise recherche sur le sujet. Je me rappelle être tombé sur un article scientifique intitulé "*Evaluation of slope stability with respect to snowpack spatial variability*" par un dénommé Johan Gaume... j'ai absolument rien compris de l'article et des formules, mais j'avais un *feeling* que c'était vraiment de la bonne science. Je ne me doutais absolument pas que 7 ans plus tard, je serais dans son laboratoire à Lausanne pour travailler sur ma thèse avec lui (Merci Johan). Je me rappelle finir mon baccalauréat et aller voir Francis Gauthier dans son bureau à Rimouski pour le convaincre que j'allais faire une maîtrise sur mon sujet préféré. Après une conversation de 30 minutes sur le vélo de montagne à Bromont, Francis m'a gentiment fait comprendre que c'est bien beau aimer un sujet mais si t'a pas d'argent... bein tu feras pas grand chose ! Il m'a ensuite gentiment proposé un *deal* de faire une maîtrise sur un sujet mandaté par le Ministre des Transports du Québec et Avalanche Québec. Il y avait un peu de variabilité spatiale, mais pas tant que ça finalement. À ta défense Francis, ce sujet était parfait pour moi à la maîtrise, car il m'a permis d'apprendre à faire de la science, faire plein d'erreurs et travailler en prévision des avalanches chez Avalanche Québec. Après ma maîtrise, j'étais maintenant rendu un adulte et prêt à m'attaquer à mon sujet préféré... la variabilité spatiale de la neige et les avalanches, bonne lecture !

RÉSUMÉ

Les avalanches de neige représentent le risque naturel le plus mortel au Canada. La compréhension du manteau neigeux pour prédire les avalanches est primordiale, mais la variabilité spatiale des propriétés mécaniques de la neige ajoute une complexité qui rend difficile la prévision des avalanches de neige. Les processus mécaniques menant à une avalanche sont bien connus de la communauté scientifique, mais les effets de la variabilité spatiale sur les mécanismes de déclenchement et de formation des avalanches demeurent inconnus. Cette thèse vise à comprendre l'influence de la variabilité spatiale des propriétés mécaniques de la neige sur le danger d'avalanche, qui se décline en deux composantes : la probabilité de déclenchement par skieur et la taille de probable de l'avalanche.

Le premier chapitre vise à mesurer et estimer la variabilité spatiale des propriétés mécaniques de la neige à l'aide des mesures *in-situ* de la variabilité spatiale de la neige sur différents sites d'études au Canada. Des modèles prédictifs spatiaux s'appuyant sur des indicateurs microtopographiques et microclimatiques pour générer des cartes haute-résolution des propriétés mécaniques et d'indices de stabilité de la neige.

Le deuxième chapitre vise à estimer l'influence de la variabilité spatiale de l'épaisseur de la plaque sur les deux composantes du danger d'avalanche. Une approche statistico-mécanique a permis de calculer la probabilité de déclenchement par skieur en fonction de différentes variations spatiales de l'épaisseur de la plaque. En s'appuyant sur ces divers patrons spatiaux d'épaisseur de plaque, une méthode numérique a été utilisée pour simuler la propagation dynamique de la fissure dans la neige et ainsi estimer la taille d'une avalanche.

Le dernier chapitre vise à comprendre l'effet de l'hétérogénéité spatiale de la couche faible sur la propagation dynamique des fissures et la taille finale de l'avalanche. La même méthode numérique utilisée au chapitre deux nous permettra de lier différents scénarios d'hétérogénéité de la résistance de la couche faible à la distance de propagation de la fissure en 2D et 3D à l'échelle d'une pente.

Cette thèse contribue à améliorer la compréhension de l'effet de la variabilité spatiale de la neige sur le danger d'avalanche.

Mots clés : Neige, avalanche, variabilité spatiale, danger d'avalanche, probabilité de déclenchement par skieur, taille de l'avalanche, propagation des fissures.

ABSTRACT

Snow avalanches represent the deadliest natural hazard in Canada. Understanding the snowpack to predict avalanches is crucial, but the spatial variability of snow mechanical properties adds complexity, making snow avalanche forecasting challenging. While the mechanical processes leading to avalanches are well-known, the effects of spatial variability on avalanche triggering and propagation mechanisms remain unknown. This thesis aims to comprehend the influence of snow spatial variability on avalanche hazard, which manifests in two components : the probability of triggering by a skier and the potential avalanche size.

The first chapter aims to measure and estimate the spatial variability of snow using *in-situ* measurements across various study sites in Canada. Spatial predictive models will utilize microtopographic indicators to generate high-resolution maps of snow mechanical properties and stability.

The second chapter aims to assess the influence of the slab thickness spatial variability on both components of the avalanche hazard. A statistical-mechanical approach will calculate the skier-triggering probability based on different spatial variations of slab thickness. A mechanical numerical method will simulate dynamic crack propagation with the same slab thickness variations to estimate avalanche size.

The final chapter aims to understand the effect of weak layer spatial heterogeneity on dynamic crack propagation and, ultimately, the final avalanche size. The same numerical method used in chapter two, will be used to link different scenarios of weak layer resistance heterogeneity to the crack propagation distance in 2D and 3D at the scale of a slope. Our work contributes to enhancing the understanding of the effect of spatial variability of snow snow mechanical properties on avalanche hazard.

Keywords : Snow, avalanche, spatial variability, avalanche hazard, skier-triggering probability, avalanche size, crack propagation.

TABLE DES MATIÈRES

LISTE DES TABLEAUX

LISTE DES FIGURES

LISTE DES ABRÉVIATIONS

AR22-PP	Échantillonnage à l'Arête de Roc le 25 Février 2022.
CT	*Compression Tests*.
DAMPM	*Depth-Averaged Material-Point-Method*.
DEM	*Discrete Element Method*.
DF	*Defragramented Precipitation Particles*.
DSM	*Digital Surface Model*.
DSM$_{snow}$	*Digital Snow Surface Model*.
DTM	*Digital Terrain Model*.
ECDF	*Experimental cumulative Density function*.
EP20-DF	Échantillonnage à l'Épaule du Mur le 25 Février 2022.
EP19-FC	Échantillonnage à l'Épaule du Mur le 25 Février 2022.
FEM	*Finite-Element Method*.
FC	*Faceted Crystals*.
GAM	*General Additive Model*.
GRF	*Gaussian Random Field*.
GNSS	*Global Navigation Satelitte System*.
JBC22-SH	Échantillonnage à *Jim Bay Corner* le 19 Janvier 2022.
JBC22-PP	Échantillonnage à *Jim Bay Corner* le 24 Janvier 2022.
LiDAR	*Light Detection and Ranging*.
MPM	*Material-Point-Method*.
MAE	*Mean Average Error*.
PP	*Precipation Particles*.
PST	*Propagation Saw Test*.
QGIS	*Quantum Geographic information System*.

RH22-PP Échantillonnage à *Round Hill* le 27 Janvier 2022.

RMSE *Root Mean Square Error*.

SAGA *System for Automated Geoscientific Analyses*.

SH *Surface Hoar Crytals*.

SMP *SnowMicroPen*.

SPI *Skier Propagation Index*.

TPI *Topographic Position Index*.

UAV *Unmaned Aerial Vehicule*.

VRM *Vector Ruggedness Measure*.

LISTE DES SYMBOLES

A_{cross} *Skier cross-slope amplitude radius.*

a *Weak layer Crack length.*

a_c *Weak layer Critical crack length.*

$\dot{a}$ *Weak layer Crack speed.*

α_i *angle defining the area of stress from the surface beneath the skier to the weak layer.*

b *basis expansion of the spline function.*

β *Ratio between the tensile and compressive resistance.*

C_{wl} *Weak layer cohesion.*

cov *Gaussian Covariance function.*

c_s *Shear wave speed of the slab.*

c_p *Elastic wave speed of the slab.*

D *Slab thickness.*

D_e *Multilayered Slab thickness* proposé par Monti et al. (2016)

$\overline{D}$ *Mean Slab thickness.*

D_{wl} *Weak layer thickness.*

d *Distance between observations (SMP measurements).*

$d_{fractal}$ *Dimension fractal.*

E *Slab Elastic modulus.*

E' *Effective Slab Elastic modulus.*

E_{wl} *Weak layer Elastic modulus.*

ϵ *Slab Thickness Correlation length.*

F *SMP parameters Peak force.*

g *Gravitational acceleration.*

G *Slab Shear modulus.*

G_{wl} *Weak layer Shear modulus.*

γ *Modified Cam-Clay yield surface.*

h *Particle height.*

$_i$ *Response variable iterator.*

$_j$ *Covariates iterator.*

$_k$ *order of the basis expansion of spline function.*

k_x *dynamic tensile stress slope.*

k_f *quasi-static tensile stress slope.*

K_{wl} *Weak layer stiffness.*

L *SMP parameters Element length.*

L *SMP parameters Element length.*

L_{wl} *SMP parameters Element length of the weak layer.*

L_0 *SMP parameters Critical Element length.*

L_t *Tensile Length.*

L_{ss} *Steady-State Length.*

L_{ca} *Crack Arrest Length.*

Λ *Characteristic length of the slab/weak layer System.*

Λ_{ava} *Characteristic length of the avalanche.*

λ *integration constant in the analytical solution Annexe IV.*

l_{sk} *Skier crack length.*

$\sum \frac{\hat{l}_x}{l_x}$ *Skier cross-slope amplitude radius.*

M *Cohesionless Critical State Line.*

N *Number of observations (SMP measurements).*

η *weigth parameter of the spline function in GAM.*

ω *Richter et al. (2019) parametrisation in critical crack length computation a_c.*

p *Pressure.*

p_0 *Consolidation Pressure.*

ϕ *Snow internal friction angle.*

ψ *Slope angle.*

ψ_{snow} *Snow surface angle.*

ϕ *Snow internal friction angle.*

q *Deviatoric or Von Mises stress.*

R *Load applied by a standing skier on the snow in N.*

R^2 *Regression coefficient.*

R_{down} *Skier down-slope radius.*

ρ *Slab Density.*

ρ_{wl} *Weak layer Density.*

ρ_{ice} *Ice Density.*

$\mathbf{Sl}_i$ *Slab layers.*

S_D^2 *Slab Thickness spatial variance.*

S_D *Slab Thickness standard deviation.*

S *undimensional number "strain".*

s *smooth or spline function.*

σ_{micro}^{th} *Snow microstructural strength.*

σ_{macro}^{th} *Snow macrostructural strength.*

σ_{zz} *Normal stress applied by the slab weight.*

σ_{xx} *Tensile stress in the downslope direction (x).*

σ_t *Slab Tensile strength.*

t *Time dimension.*

τ *Shear stress due to the slab weight.*

τ_{xz} *Shear stress in the downslope direction (x).*

$\Delta\tau$ *Shear stress applied by the skier.*

τ_p *Weak layer shear strength.*

τ_r *Residual stress.*

T_{wl} *undimensional number "weak layer relative slow down".*

u *particle displacement.*

u_c *Critical particle displacement.*

u_r *Residual particle displacement.*

v *Particle velocity in downslope direction.*

V *Omnidirectional Experimental Variogram.*

ΔV *Slope of the log-log Experimental Variogram.*

ν *Poisson's ratio.*

X *Covariates.*

x *Physical dimension representing the up and down slope direction.*

ξ *Vector parameter for parametric component in GAM function.*

Y *Response Variable in spatial analysis.*

y *Physical dimension representing the cross-slope direction.*

Z *Row of model matrix for any strictly parametric component in GAM function.*

z *Physical dimension representing the slab thickness direction.*

ζ *SMP parameters deflection at Peak force.*

INTRODUCTION GÉNÉRALE

Danger et formation des avalanches

Les avalanches de neige représentent un risque naturel pour les infrastructures et les amateurs de sports récréatifs en montagne à travers le monde (Stethem *et al.*, 2003). Elles peuvent être divisées en différents types, notamment les avalanches humides ou sèches, ainsi que celle sous forme de neige sans cohésion ou de plaques (Schweizer *et al.*, 2003). Cependant, les avalanches de plaques de neige sèche sont les plus destructrices et les plus difficiles à prévoir (Techel *et al.*, 2016). Ces dernières sont responsables de la majorité des accidents mortels d'avalanches (McClung et Schaerer, 2006). Plusieurs éléments doivent être présents pour qu'une avalanche de plaque survienne. Premièrement, une couche de neige poreuse avec une faible cohésion doit se former dans le manteau neigeux. Cette couche faible peut être composée de différents cristaux tels que des particules de neige de précipitation lors d'une chute de neige, de cristaux à faces planes, de givre de profondeur ou de surface. Bien que ces cristaux se forment par divers processus thermodynamiques dans le manteau neigeux ou dans l'atmosphère, ils partagent tous une caractéristique commune : une résistance au cisaillement relativement plus faible que les autres cristaux constituant le manteau neigeux (Schweizer *et al.*, 2003). Les cristaux à faces planes et le givre de surface représentent des déclenchements des avalanches de plaque les plus meurtriers et sont responsables de plus de la moitié des accidents d'avalanche (McClung et Schaerer, 2006). Ensuite, cette couche faible doit être en-dessous d'une plaque de neige où les cristaux ont un lien cohésif entre eux, comme par exemple une plaque de neige ventée où le transport par le vent a provoqué un lien cohésif entre les cristaux. Cette stratigraphie spécifique doit être présente sur une pente inclinée, puis un élément déclencheur doit provoquer la rupture de la couche faible enfouie sous la plaque de neige cohésive. Ce déclenchement peut être provoqué par un skieur, une précipitation additionnelle (sous forme solide ou liquide) ou des explosifs, appliquant une augmentation des contraintes en cisaillement sur la couche faible jusqu'à sa rupture. Si la

longueur de la rupture dans la couche faible - ou la fissure - dépasse une longueur critique, la fissure peut se propager d'elle-même à travers la pente, entraînant le déclenchement et le glissement de la plaque (Figure 1) (Schweizer *et al.*, 2016). Ce processus mécanique de déclenchement d'une fissure dans la couche faible, ainsi que sa propagation sur l'ensemble de la pente, constitue un processus mécaniques multi-échelle, allant de la microstructure des cristaux de neige jusqu'à la taille d'un versant. (Schweizer *et al.*, 2016).

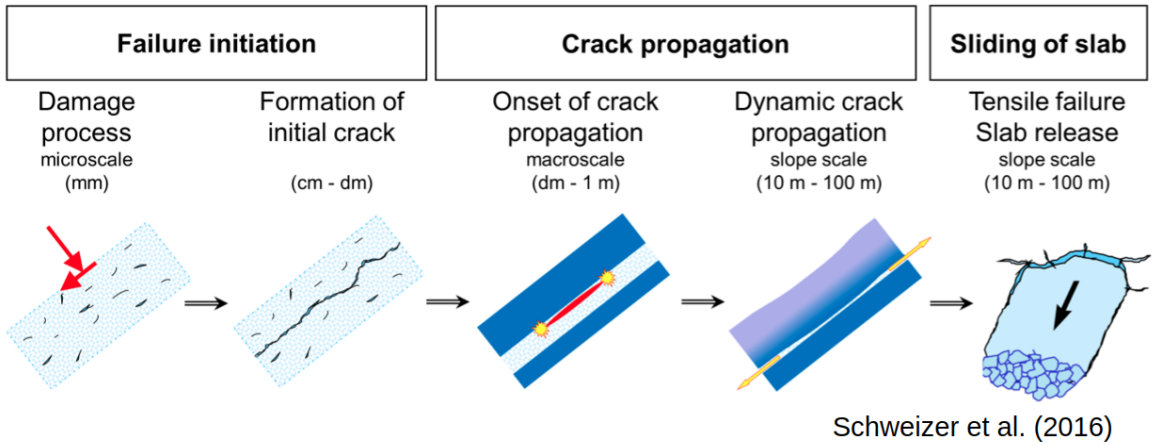

FIGURE 1 – Modèle conceptuel de formation d'une avalanche représentant les différents processus mécaniques : 1) contraintes en compression et cisaillement sur la couche faible, 2) rupture initiale et apparition de la fissure dans la couche faible, 3) longueur critique de la fissure et début de propagation, 4) propagation dynamique de la fissure le long de la pente, et 5) apparition d'une fracture en tension dans la plaque et libération de la plaque. Cette figure est issus de Schweizer *et al.* (2016).

Afin de protéger et d'avertir les amateurs de sport en montagne au danger d'avalanches, des services de prévision communiquent le danger d'avalanche quotidiennement. Statham *et al.* (2018) ont proposé un modèle conceptuel afin de mieux prédire et communiquer le danger d'avalanche pour les prévisionnistes, guides de montagnes et amateurs de sports en montagne. Ce modèle conceptuel est basé sur deux composantes principales : la probabilité (aléa) et la taille de l'avalanche (conséquence). La combinaison de ces deux composantes donne le danger d'avalanche en Amérique du Nord (Statham *et al.*, 2018). La terminologie est légèrement différente en Europe, où elle est basée sur trois composantes : la probabi-

lité de déclenchement d'une avalanche, la fréquence spatiale des points de déclenchement et la taille de l'avalanche (Techel *et al.*, 2020). Les prévisionnistes et les guides utilisent principalement des observations d'avalanches et des tests de stabilité de la neige pour obtenir des informations sur la probabilité de déclenchement d'une avalanche, que ce soit par un skieur ou naturellement. Des tests répétés à de nombreux endroits les aident à obtenir des informations sur la distribution spatiale de l'instabilité (Schweizer *et al.*, 2008a). Cependant, la nature ponctuelle des observations disponibles sur les propriétés du manteau neigeux rend la prévision des avalanches complexe (Hägeli et McClung, 2004). La deuxième composante principale du danger d'avalanche est la taille de l'avalanche, directement liée aux conséquences. Les prévisionnistes tentent de prédire la taille possible de l'avalanche en estimant l'épaisseur de la plaque et la propension à la propagation de la fissure dans la couche faible. Des études ont montré que les propriétés mécaniques de la neige sont très variables dans l'espace (p. ex. : Schweizer *et al.*, 2008a), ce qui devrait influencer les différents processus mécaniques multi-échelles nécessaires à la formation d'une avalanche, de la rupture de la couche faible, à la propagation dynamique jusqu'au détachemenent de la plaque. Cette complexité rend l'évaluation du risque d'avalanche difficile, tant pour les amateurs de montagnes et les prévisionnistes d'avalanches.

Variabilité spatiale de la neige

Le sujet de la variation spatiale de la neige a été étudié depuis plusieurs décennies. La variabilité spatiale des propriétés de la neige est bien documentée dans les études climatiques (p. ex. : Harper et Bradford, 2003), la dynamique des glaciers (p. ex. : Pulwicki *et al.*, 2018), l'hydrologie de la neige (p. ex. : Deems *et al.*, 2006), la météorologie en montagne (p. ex. : Mott *et al.*, 2011), le pergélisol (p. ex. : Wirz *et al.*, 2011), et les avalanches (p. ex. : Schweizer *et al.*, 2008a). De nombreuses études se sont penchées sur la distribution spatiale de la hauteur de la neige et de son équivalent en eau pour soutenir les modèles hydrologiques (p. ex. : Deems *et al.*, 2006; Grünewald *et al.*, 2010; Schirmer *et al.*, 2011; Winstral *et al.*, 2002). La

plupart de ces études utilisent la géostatistique pour expliquer, comprendre et modéliser la variabilité spatiale de la neige. La géostatistique est basée sur l'utilisation du variogramme, mettant en relation la variance et la distance entre les observations d'une variable spatiale. Le variogramme peut démontrer de l'autocorrélation spatiale lorsque la variance augmente en fonction de la distance, jusqu'à ce que cette variance se stabilise après une certaine distance. On définit la distance d'autocorrélation comme étant la distance à laquelle la variance se stabilise (Figure 2). Un patron spatial d'une variable est donc défini par la variance spatiale et la distance d'autocorrélation (ou l'échelle) représentées dans un variogramme. Les études mentionnées ci-dessus ont utilisé le variogramme à diverses échelles pour comprendre la variabilité spatiale de la neige.

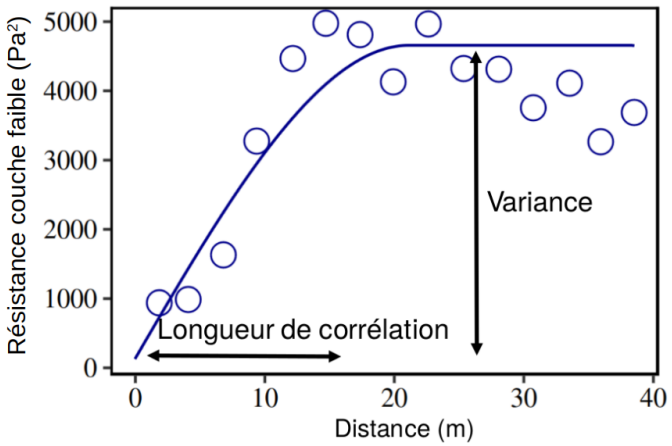

FIGURE 2 – Variogramme expérimental (cercles) et variogramme théorique (ligne) de la résistance au cisaillement de la couche faible. L'axe des abscisses représente la distance entre chaque observation d'un échantillonnage. La variance représente la différence des valeurs au carré entre chaque observation. La variance et la distance d'autocorrélation décrivant le patron spatial sont représentées avec des flèches.

Le point commun des résultats de ces études est que la variabilité spatiale de la neige est présente à différentes échelles spatiales, partant du massif montagneux (1-10 km) jusqu'à l'échelle de la pente (1-10 m), et même à l'échelle de la microstructure (1-10 mm). Cette variabilité spatiale multi-échelle est principalement causée par les processus météorologiques,

également multi-échelles, par exemple la redistribution de la neige par le vent sur une pent sous le vent (échelle du massif), et la redistribution causée par la recirculation du vent autour d'un rocher ou des arbres (échelle de la pente). Certains chercheurs ont approfondi l'étude de cette variabilité multi-échelle (Deems *et al.*, 2006; Mott *et al.*, 2011; Schirmer et Lehning, 2011; Trujillo *et al.*, 2007). Ils ont analysé les propriétés d'échelle et la dimension fractale de la hauteur de neige. L'idée sous-jacente aux propriétés d'échelle et à la dimension fractale est que plusieurs échelles peuvent définir un patron spatial plutôt qu'une seule échelle comme dans un variogramme. La dimension fractale caractérise également la rugosité d'un patron spatial à travers de multiples échelles. Ces chercheurs ont comparé la dimension fractale de la hauteur de neige avec celle de la topographie et de la végétation, démontrant un lien spatial entre ces trois variables. Cependant, aucune étude n'a exploré la dimension fractale des propriétés mécaniques de la neige. La plupart des études se sont basées sur le LiDAR ou des relevés manuels de sondes à neige pour estimer la hauteur de neige. Cependant, celle-ci n'est pas un indicateur suffisant pour décrire les conditions nécessaires à la formation d'une avalanche. La mesure *in-situ* des propriétés mécaniques de la neige est plus complexe que la mesure de la hauteur de neige, mais les propriétés mécaniques sont de meilleurs indicateurs de la stabilité de la neige pouvant mener à la formation d'une avalanche.

Mesure *in-situ* de la stabilité de la neige

Il existe plusieurs méthodes pour mesurer les propriétés mécaniques de la neige pouvant décrire sa stabilité. Des mesures directes en cisaillement de la couche faible donnent une indication quantitative de la «force» ou résistance de la couche faible susceptible de former une avalanche. Conway et Abrahamson (1984) ont effectué plusieurs mesures de la résistance au cisaillement d'une couche faible le long d'une couronne d'avalanche. Ils ont mis en évidence des zones de déficit, où la résistance au cisaillement de la couche faible était significativement plus faible que dans les zones environnantes le long de la couronne. L'idée de zones faibles ou de points faibles a initié de nombreuses études au cours des deux

dernières décennies (Schweizer *et al.*, 2008a). Des tests *in-situ* de stabilité ont également été développés pour évaluer la stabilité du manteau neigeux (p. ex. : Jamieson, 1999). Ces tests sont aujourd'hui largement utilisés dans l'industrie des avalanches pour évaluer la stabilité de la neige, et ultimement le danger d'avalanche. Ils fournissent une évaluation semi-quantitative de l'interaction mécanique entre la plaque cohésive et la couche faible. Certaines études ont examiné la variabilité spatiale de plusieurs tests de stabilité de la neige sur une pente propice aux avalanches (Kronholm et Schweizer, 2003; Birkeland, 2001; Campbell et Jamieson, 2007). Les résultats de ces études ont démontré une variation dans les résultats des tests, avec une variation des distances de corrélation d'environ 5 à 20 m. Cependant, ces tests de stabilité de la neige ne fournissent pas d'informations sur les propriétés mécaniques de la plaque et de la couche faible. De plus, ces tests prennent du temps, ce qui entraîne une couverture d'échantillonnage spatiale limitée pour l'analyse statistique, avec environ 30 mesures couvrant 20 m pour ces études (Kronholm et Schweizer, 2003; Birkeland, 2001; Campbell et Jamieson, 2007).

Des instruments tels que le pénétromètre à neige haute résolution appelé *SnowMicroPen* (SMP) peuvent mesurer avec une grande précision certaines propriétés mécaniques de la neige, caractérisant adéquatement la plaque ainsi que la couche faible (Proksch *et al.*, 2015; Löwe et van Herwijnen, 2012; Johnson et Schneebeli, 1999; Reuter *et al.*, 2019). Le traitement des trois paramètres de base du signal SMP (*Penetration force* F, *element length* L et *deflection at rupture* ζ) permet de calculer plusieurs propriétés mécaniques de la neige, telles que la masse volumique ρ, la résistance au cisaillement τ et le module élastique E (Figure 3). Le SMP permet un échantillonnage rapide des propriétés mécaniques de la neige pour plusieurs emplacements sur une pente propice aux avalanches (Bellaire et Schweizer, 2011; Feick *et al.*, 2007; Lutz *et al.*, 2007; Landry *et al.*, 2004; Kronholm, 2004; Lutz et Birkeland, 2011; Reuter *et al.*, 2016). Ces études se sont principalement concentrées sur les propriétés de la couche faible, notamment l'épaisseur et la résistance, en utilisant le variogramme pour estimer le patron spatial des propriétés mécaniques de la couche faible. Elles ont démontré des distances de corrélation allant de 1 à 15 m avec une étendue d'échantillonnage spatiale

d'environ 20 à 40 m. Cependant, les distances de corrélation étaient presque la moitié de l'étendue de la couverture d'échantillonnage, ce qui pourrait biaiser l'estimation de la longueur de corrélation (Skøien et Blöschl, 2006; Kronholm et Birkeland, 2007). Reuter *et al.* (2016) ont utilisé une couverture spatiale plus importante avec une étendue d'environ 500 m, et ont signalé des distances de corrélation de 5 à 25 m, avec une exception de 68 m.

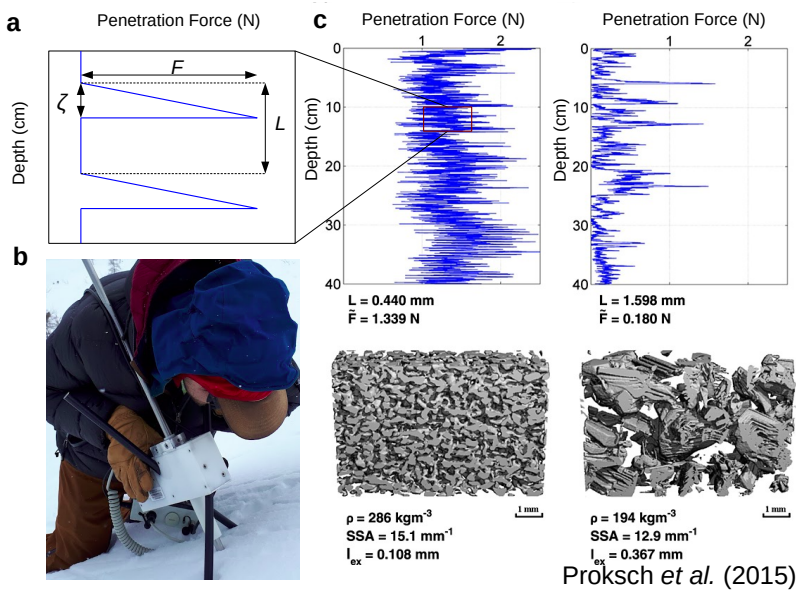

FIGURE 3 – Pénétromètre à neige haute-résolution ou *SnowMicroPen* SMP. a) représentation schématique des trois paramètes principaux du signal SMP : *Penetration Force F*, *Element length L* et *deflection at rupture* ζ. b) SMP sur le terrain. c) Exemple de profil de résistance pour des cristaux de regel (gauche) et des givres de profondeur (droite) issus de Proksch *et al.* (2015).

Kronholm (2004) et Bellaire et Schweizer (2011) ont démontré que les patrons spatiaux de la couche faible et de la plaque peuvent avoir des distances de corrélation différentes pour le même échantillonnage. Ce résultat montre que les processus météorologiques responsables de la mise en place de la couche faible et de la plaque sont différents, résultant en un patron spatial également différent. Cependant, l'étendue spatiale de l'échantillonnage de la neige était relativement petite, seulement deux fois la longueur de corrélation mesurée, et cela pourrait affecter l'estimation de la longueur de corrélation (p. ex. : Dale et Fortin,

2014; Skøien et Blöschl, 2006). Cette question devrait être approfondie avec une étendue d'échantillonnage spatiale d'au moins 3 à 5 fois supérieur à la longueur de corrélation attendue de 20 m (Dale et Fortin, 2014), afin d'améliorer la prise en compte de la variabilité de la neige dans les modèles mécaniques.

Modélisation géostatistique

Les patrons spatiaux des propriétés de la neige peuvent être expliqués et estimés par des modèles statistiques utilisant des variables spatiales exploratoires. Cette technique est appelée krigeage avec *drift* externe, combine des variables spatiales exploratoires et le variogramme pour interpoler et cartographier une variable environnementale (**?**). Plusieurs études ont utilisé le krigeage pour interpoler et cartographier la stabilité de la neige, tels que les résultats des tests de stabilité de la neige, les propriétés mécaniques dérivées du SMP et des indices de stabilité (Birkeland, 2001; Mullen et Birkeland, 2008; Reuter *et al.*, 2015a; Schweizer et Kronholm, 2007). Ces études ont démontré que la stabilité ponctuelle de la neige peut être estimée spatialement à l'aide d'indicateurs topographiques tels que l'orientation, l'élévation et l'angle de pente à l'échelle du massif. Ces indicateurs capturent les interactions complexes entre les processus météorologiques et les caractéristiques du terrain, telles que la déposition de la neige par le vent et l'influence du rayonnement solaire sur la neige entre différentes pentes (Reuter *et al.*, 2016). Cependant, des résidus spatiaux autocorrélés persistent après l'utilisation de modèles statistiques incorporant des indicateurs topoclimatiques, indiquant une variabilité résiduelle non-expliquée. Cette variabilité spatiale résiduelle pourrait être attribuée à d'autres phénomènes spatiaux à une échelle plus petite, comme par exemple l'ombrage du relief avoisinant ou des arbres.

Certains chercheurs ont réussi à expliquer et à estimer la variabilité spatiale de la hauteur de neige sur des pentes relativement homogènes, où l'orientation et l'élévation restaient relativement constants (p. ex. : Deems *et al.*, 2006; Grünewald *et al.*, 2010; Pulwicki *et al.*, 2018; Revuelto *et al.*, 2020; Meloche *et al.*, 2022; Trujillo *et al.*, 2007; Winstral *et al.*, 2002).

Ils ont utilisé dans leurs études des indicateurs microtopographiques tels que la forme de la pente (indice de position topographique TPI), l'indice de végétation et des indices microclimatiques tels que l'exposition au vent (indice Winstral) ou le potentiel de rayonnement solaire. Guy et Birkeland (2013) ont relié ces paramètres microtopographiques à des zones potentielles de déclenchement, caractérisées par la présence de cristaux de givre de profondeur. Cependant, la présence de cristaux de givre de profondeur est insuffisante pour caractériser la stabilité de la neige, qui nécessite plus d'informations sur les propriétés mécaniques de la plaque et de la couche faible. Reuter *et al.* (2016) ont lié la stabilité de la neige, à partir de propriétés mécaniques de la neige dérivées du SMP, avec des indicateurs topographiques à l'échelle d'une cuve alpine (100-500 m). Alors que les études spatiales précédentes explorent des relations linéaires entre la stabilité de la neige et les indicateurs topographiques, Reuter *et al.* (2016) suggèrent que la relation entre la stabilité de la neige et les indicateurs topographiques pourrait être non linéaire.

Influence sur le danger d'avalanche

Déclenchement d'avalanche

L'étude de Conway et Abrahamson (1984) a également démontré une possible influence de zones faibles sur le déclenchement d' une avalanche. Deux décennies plus tard, Kronholm et Schweizer (2003) ont proposé un modèle conceptuel pour expliquer l'effet de la variation spatiale sur la stabilité de la pente. Une variation à courte distance pourrait avoir un effet stabilisateur sur le manteau neigeux, tandis qu'une variation à longue distance pourrait avoir un effet de "*knock-down*" sur la stabilité de la pente, causant un déclenchement de la pente même si la stabilité moyenne est au-dessus du seuil de rupture. Cependant, des investigations supplémentaires à travers des modèles mécaniques étaient nécessaires pour tester ce modèle conceptuel. Plusieurs études ont simulé artificiellement des patrons spatiaux de la couche faible dans des modèles mécaniques afin d'expliquer l'effet de la variabilité spatiale de la

couche faible sur la stabilité de la pente (Gaume *et al.*, 2014, 2013; Kronholm *et al.*, 2004; Schweizer *et al.*, 2008a; Fyffe et Zaiser, 2004).

Tout d'abord, certaines études ont utilisé des modèles à automates cellulaires pour montrer l'effet de la variance des valeurs de résistance au cisaillement sur la stabilité de la pente (Fyffe et Zaiser, 2004; Kronholm et Birkeland, 2005; Faillettaz *et al.*, 2004). Des variances élevées des valeurs de résistance au cisaillement créent plus de zones faibles et facilitent la rupture générale de la pente, même avec des zones fortes en résistance au cisaillement. Cependant, ces modèles tiennent compte que de l'état des cellules voisines et la redistribution élastique à grande échelle ne peut pas être prise en compte. L'influence de la longueur de corrélation sur la stabilité ne peut pas être explorée avec cette méthode numérique. La méthode des éléments finis (FEM) peut représenter la redistribution élastique à grande échelle et a été utilisée pour expliquer l'influence de la longueur de corrélation sur la stabilité de la pente (p. ex. : Mackenzie *et al.*, 1994). Gaume *et al.* (2013) ont démontré dans quelle mesure la redistribution élastique de la plaque pourrait lisser l'hétérogénéité de la couche faible. Leur étude a montré que si la longueur de corrélation est plus petite que la longueur élastique caractéristique du système, celui-ci se comporte comme dans un cas homogène. En revanche, lorsque la longueur de corrélation est plus grande que cette longueur élastique, le lissage ne se produit pas et la pente est plus susceptible de rompre, illustrant ainsi l'effet *knock-down* (Figure 4) (Gaume *et al.*, 2014).

Les études s'appuyant sur la FEM ont principalement examiné la variation spatiale de la cohésion de la couche faible et son impact sur le déclenchement naturel d'une avalanche, qui implique un chargement plus progressif à l'échelle de la pente par rapport au déclenchement par un skieur (p. ex. : Monti *et al.*, 2016). De plus, il est bien établi que la hauteur de la neige varie considérablement dans les zones montagneuses (p. ex. :, Deems *et al.*, 2006; Winstral *et al.*, 2002; Mott *et al.*, 2011; Grünewald *et al.*, 2013; Schirmer *et al.*, 2011; Hubbard *et al.*, 2018), en particulier dans les zones de départ d'avalanches (Miller *et al.*, 2022). La variabilité spatiale de l'épaisseur de la plaque devrait être liée à la variation spatiale de la hauteur de la

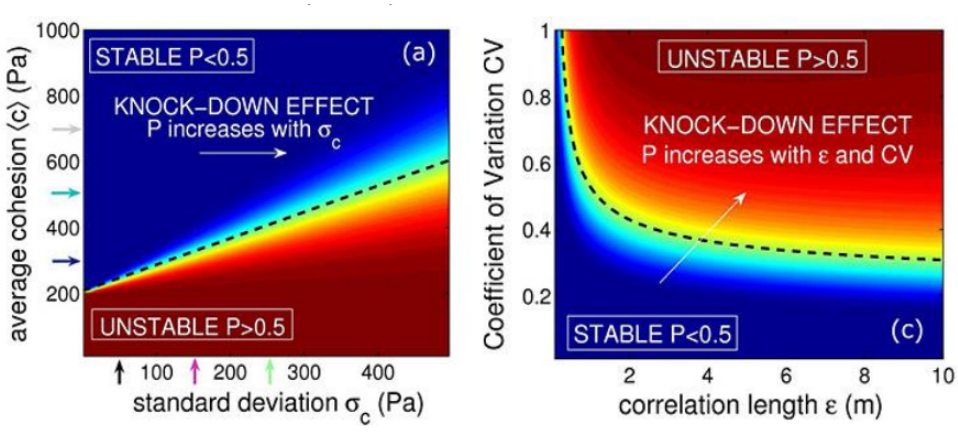

FIGURE 4 – Influence de la variabilité spatiale de la cohésion (résistance) de la couche faible sur la probabilité de déclenchement naturel issus de simulations réalisées avec la méthode des éléments finis. Les couleurs représentent la probabilité de déclenchement naturel. La variabilité spatiale est définie selon trois paramètres, la cohésion moyenne, le coefficient de variation et la longueur de corrélation. Cette figure a été adapté de Gaume *et al.* (2014), certains éléments ont été retiré par simplicité.

neige. Par conséquent, cette variation de l'épaisseur de la plaque devrait influencer la probabilité de déclenchement d'une avalanche par un skieur sur l'ensemble d'une pente. Pour les cas homogènes, l'influence de l'épaisseur de la plaque sur le déclenchement par un skieur a été analysée en fonction d'une approche basée sur l'analyse des contraintes et des résistances (Föhn, 1987; Monti *et al.*, 2016; Habermann *et al.*, 2008), ainsi que la propension à la propagation des fissures dans la couche faible (Heierli *et al.*, 2008; Gaume *et al.*, 2017). Cependant, à ce jour, il n'existe pas d'étude sur l'effet de la variation spatiale de l'épaisseur de la plaque sur la probabilité de déclenchement par un skieur et la propagation de fissures dans la couche faible. Il est important de noter que la variabilité de l'épaisseur de la plaque devrait également avoir un impact sur la taille potentielle de l'avalanche. Les propriétés de la plaque, principalement l'épaisseur et la masse volumique, sont des facteurs clés de la propagation des fissures (McClung, 1981; Heierli *et al.*, 2008; Gaume *et al.*, 2017). La variation spatiale devrait affecter les contraintes de la plaque et pourrait favoriser l'arrêt de la propagation causé par une fracture en tension dans la plaque (perpendiculaire à la couche faible). Il est nécessaire de poursuivre les études sur ce sujet, ce qui pourrait mener à des estimations plus précises de la

taille de l'avalanche, une information cruciale pour la prévision des avalanches et la gestion des risques.

Taille de l'avalanche

De nombreuses études se sont concentrées sur l'initiation de la rupture et l'évaluation de la longueur critique de la fissure dans la couche faible nécessaire pour débuter une propagation (p. ex. : Föhn, 1987; McClung, 1981; Heierli *et al.*, 2008; Gaume *et al.*, 2017). La mesure de cette longueur critique peut être réalisée grâce un test mécanique surnommé *propagation saw test* PST (Gauthier et Jamieson, 2008), fournissant des informations cruciales pour la prévision des avalanches. Cependant, estimer les conséquences de l'avalanche, déterminées par la superficie de propagation de la fissure, est beaucoup plus difficile à estimer car les processus mécaniques impliquées ne sont pas entièrement compris. Récemment, la recherche sur les avalanches de neige s'est tournée vers la propagation dynamique des fissures, visant à améliorer les prédictions de la taille des avalanches (Bobillier *et al.*, 2021; Bergfeld *et al.*, 2023; Trottet *et al.*, 2022). Une approche prometteuse dans ce domaine a été présentée par Veitinger *et al.* (2016), qui a utilisé un cadre probabiliste pour prédire les zones potentielles de libération d'avalanches en se basant sur des caractéristiques topographiques et des cartes d'hauteur de neige. Bien que cette méthode fournisse des résultats intéressants et semble prometteuse pour des applications opérationnelles, elle manque d'éléments mécaniques pour comprendre pleinement la propagation dynamique des fissures. Il est donc nécessaire de poursuivre les recherches dans ce domaine en intégrant davantage d'éléments mécaniques pour améliorer la compréhension de la propagation des fissures et, par conséquent, affiner les prédictions de la superficie de propagation déterminant la taille des avalanches. Cette approche pourrait conduire à des avancées significatives dans la prévision des avalanches et dans la réduction des risques associés.

Mode de propagation des fissures dans la neige

La compréhension de la propagation des fissures dans les avalanches de plaques de neige sèche a évolué au fil du temps. Initialement, la propagation des fissures dans les avalanches de plaques de neige sèche était comprise avec un mode de fracture en cisaillement (mode II) dans la couche faible (Figure 5) (McClung, 1981). Cependant, ce modèle de propagation en cisaillement n'explique pas la propagation de fissures sur le plat, ni les observations d'avalanches déclenchées à distance depuis le plat. Johnson (2000) s'est penché sur cette problématique et a observé un changement dans l'épaisseur de la couche faible lors de la propagation sur le plat, indiquant que la couche faible s'effondre lors de la propagation de la fissure dans la couche faible. Cette observation a conduit à la proposition d'une théorie selon laquelle la propagation de fissures sur le plat nécessite une contrainte en compression venant de la plaque causé par l'effondrement de la couche faible. De plus, il a suggéré que l'effondrement de la couche faible provoque une flexion dans la plaque et que la vitesse de propagation est alors gouvernée par l'onde de flexion se propageant dans la plaque. Lors de mesures de vitesse de propagation faites par deux auteurs (Johnson *et al.*, 2004; van Herwijnen, 2005), ceux-ci ont confirmé cet effondrement de la couche faible. Ces connaissances ont mené à l'introduction d'un test mécanique de la neige appelé le *Propagation saw test* (PST) (Figure 6-a) (Gauthier et Jamieson, 2008). Ce test a mis en évidence le rôle significatif de l'effondrement de la couche faible et la flexion subséquente de la plaque dans la formation de l'avalanche. Pour mieux reproduire les mesures de PST sur le terrain, ainsi que les observations de déclenchement à distance sur le plat des avalanches, Heierli *et al.* (2008) a proposé une formule analytique décrivant un mode de propagation nommé *anticrack*. Ce terme provient d'un mode de fracture en compression précédemment observés dans d'autres contextes, tels que les calcaires hautement dissous (Fletcher et Pollard, 1981), dans les *superheated glaciers* (Knight et Knight, 1972), et les tremblements de terre de zone de subduction profonde (Green *et al.*, 1990). Ce mode de fracture dans la neige représente la perte volumétrique due à l'effondrement de la couche faible ce qui engendre la flexion de la plaque, concentrant

les contraintes aux extrémités de la fissure, pour ainsi soutenir la propagation. Ce modèle représente un mode de propagation de la fissure avec une tension de fermeture (anti-mode I) par opposition à un mode de fracture d'ouverture en tension (mode I) (Figure 5).

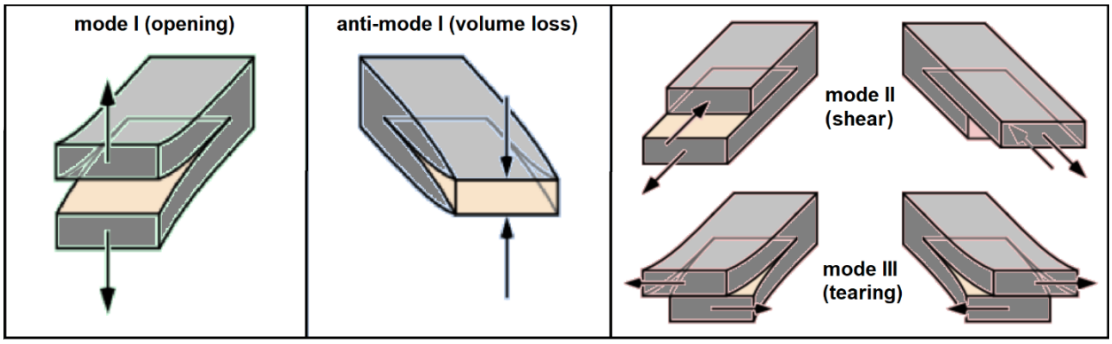

FIGURE 5 – Différents mode de fracture pour la propagation des fissures, mode I overture en tension, anti-mode I fermeture en tension, mode II cisaillement, et mode III déchirement rotationel. Cette image a été adaptée par Ron Simenhois du site https ://www.naturalfractures.com/1.1.1.htm).

Les régimes de vitesse des ondes de propagation donnent des information sur le mode de propagation. Des mesures ont été réalisé lors de l'élaboration de la théorie *anticrack* par Johnson (2000) et van Herwijnen (2005). Les mesures de Johnson (2000) ont révélé une vitesse de propagation sur le plat d'environ 20 m s^{-1}, alors que van Herwijnen (2005) rapporte des vitesses de propagation de l'ordre de 30 m s^{-1}. Ces vitesses de propagation se situent dans un régime de vitesse de propagation Sub-Rayleigh, sous la vitesse des ondes de cisaillement. Une décennie plus tard, Hamre *et al.* (2014) ont mesuré des vitesses de propagation de fissures en utilisant une analyse vidéo d'avalanches réelles, ils rapportent des vitesses mesurées allant de 15 à 428 m s^{-1} mais concentrées autour de 50 à 125 m s^{-1}. Les mesures de vitesse de propagation au plat correspondent aux mesures les plus basses rapportées par Hamre *et al.* (2014), mais les vitesses élevés (> 100 m s^{-1}), qui se situe au-dessus de la vitesse des ondes de cisaillement, demeurent inexpliquées.

Les études menées par Bobillier *et al.* (2021) ont fourni des détails micro-mécaniques concernant la propagation dynamique des fissures. Ils ont simulé des PST de 5 m de long à

plat et en pente (Figure 6-b), afin d'observer les dommages à micro-échelle engendrés par les contraintes en compression, ainsi que l'atteinte d'une vitesse de propagation constante. La vitesse de fissure observée (40 m s^{-1}) dans la simulation correspondait à la plage inférieure des vitesses rapportées par Hamre *et al.* (2014). Ils ont noté que les contraintes au début du PST étaient à la fois en cisaillement et en compression (théorie *anticrack*). Cependant, un changement de contrainte a été observé pour les PST en pente, où la contrainte en cisaillement augmentait à mesure que la vitesse de propagation approchait un régime permanent (vitesse constante). En complément à ces simulations, Bergfeld *et al.* (2021) ont réalisé des PST réels de 10 m de long sur le plat pour mesurer la propagation dynamique des fissures. Leurs vitesses de propagation étaient dans la même plage que Bobillier *et al.* (2021) et la plage inférieure (environ 50 m s^{-1}) mesurée par Hamre *et al.* (2014). Cependant, la plus grande vitesse de propagation (> 100 m s^{-1}) n'était toujours pas expliquée, ce qui est critique puisque cette vitesse est associée à des mesures sur des vidéo d'avalanches réelles, et non des PST réalisés ou simulés sur le plat. Des méthodes numériques plus avancées étaient nécessaires pour simuler ces vitesses élevées (> 100 m s^{-1}), observées sur des avalanches réelles.

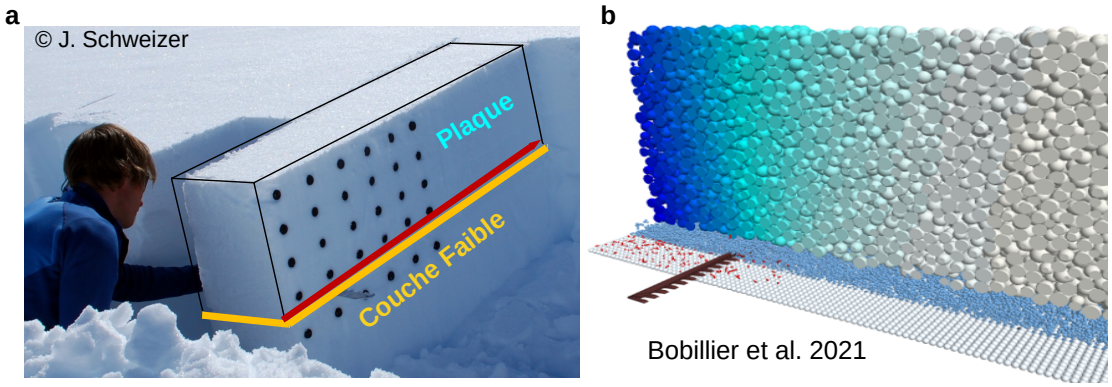

FIGURE 6 – Test de propagation de la scie ou *Propagation saw test* PST : a) PST réalisé sur le terrain et b) PST simulé numériquement avec la méthode des éléments discrets (DEM) issus de Bobillier *et al.* (2021).

Méthode numérique

Plusieurs méthodes numériques ont été utilisées pour modéliser le début et la propagation dynamique des fissures. Premièrement, la méthode des éléments discrets (DEM) a pu représenter l'effondrement volumétrique de la couche faible (*anticrack*), et par le fait même la propagation sur le plat (Gaume *et al.*, 2017; Bobillier *et al.*, 2021). Cependant, cette méthode numérique est lourde en temps de calcul, menant à des temps de calcul d'une dizaine de jours pour simuler un PST de 10 m de long, ce qui rends difficile voir impossible une analyse de sensibilité. Il existe d'autres méthodes plus efficace en temps de calcul, notamment la *Material Point-Method* (MPM). Cette méthode est une combinaison de techniques eulériennes (calcul en grille) et lagrangiennes (calcul sur particules). Elle permet de simuler la transition solide-fluide et la propagation des fissures dans un matériau granulaire (Sulsky *et al.*, 1994), avec un temps de calcul plus réaliste (quelques heures). Récemment, Gaume *et al.* (2019) ont complété cette méthode en introduisant un comportement élastoplastique avec un nouveau modèle constitutif de la neige pouvant représenter le comportement mécanique de la plaque et de la couche faible. Cette avancée permet la simulation de divers processus mécaniques dans une avalanche de plaque : la rupture et l'affaissement de la couche faible, la propagation dynamique de la fissure, les fractures en tension de la plaque, et finalement l'écoulement de la plaque sur la pente. Trottet *et al.* (2022) ont utilisé cette méthode numérique en plus d'une analyse vidéo d'avalanche de neige à grande échelle (Simenhois *et al.*, 2023) pour approfondir les résultats de Bobillier *et al.* (2021). Ils ont simulé des PST de 30 m de long, à la fois sur un terrain plat et incliné, et ont remarqué une transition du mode de fracture *anticrack* (anti-mode I) à un mode de fracture en cisaillement (mode II). Ce régime de propagation dit *supershear* a également été observé en mécanique des tremblements de terre (Xia *et al.*, 2004). Ce régime est caractérisé par un mode de fracture qui se produit en cisaillement (mode II) à une vitesse de propagation supérieure à la vitesse d'onde de cisaillement (de la plaque). Les valeurs de vitesse de fissure en mode *supershear* correspondaient à la plage de vitesse de fissure supérieure (> 100 m/s) observée par Hamre *et al.* (2014). Trottet *et al.*

(2022) ont constaté que cette transition se produit généralement à un angle de pente supérieur à l'angle de frottement de la neige ($\phi \approx 27°$) et une distance de propagation d'au moins trois à cinq mètres. Ces deux modèles de propagation qui semblaient être en opposition, sont donc complémentaires pour expliquer la propagation des fissures dans la neige. Le modèle *anti-crack* explique la propagation sur le plat à des vitesses Sub-Rayleigh, mais aussi en pente lorsque la fissure est en dessous de la *super critical crack length*, qui est la taille critique, dite *supershear* lorsque le mode de fracture passe en mode II, d'environ trois à cinq mètres. Au-delà de cette taille sur une pente, le mode de fracture transitionne vers du cisaillement pure, à des vitesses plus élevés que les ondes de cisaillement en se rapprochant aux vitesses des ondes élastiques. Un modèle de propagation en cisaillement pur, tel que proposé au départ par McClung (1981), semble suffisant pour simuler les avalanches sur une pente inclinée. Les avalanches déclenchées sur le plat ou à un angle inférieur à l'angle de frottement de la neige ($\phi \approx 27$), est expliqué par la théorie *anticrack* basée sur l'effondrement de la couche faible.

Arrêt de propagation de la fissure

La compréhension de la propagation dynamique des fissures continue d'évoluer avec le développement des mesures novatrices permettant la mesure des contraintes sur PST (Bergfeld *et al.*, 2021), ainsi qu'avec une modélisation numérique réaliste et précise. Cependant, peu d'études se sont concentrées sur l'éventuel arrêt de la propagation des fissures, lié à l'apparition d'une fracture en tension de la plaque menant au relâchement complet de la plaque. Une plus grande connaissance de la fracture en tension de la plaque et de son impact sur l'arrêt de la propagation des fissures est cruciale pour estimer la taille finale de l'avalanche. Gaume *et al.* (2015a) ont utilisé la méthode des éléments finis pour explorer comment l'hétérogénéité de la couche faible pourrait provoquer une fracture en tension de la plaque pendant la propagation dynamique des fissures. Bien qu'ils aient supposé qu'une fracture en tension de la plaque puisse être un indicateur d'un arrêt de propagation de la fissure, la méthode utilisé par Gaume *et al.* (2015a) ne peut pas réprésenter explicitement l'arrêt de la propagation de

la fissure dans la couche faible menant au relâchement de la plaque. En utilisant la MPM, l'étude de Trottet *et al.* (2022) a permis de démontrer l'effet des fractures en tension dans la plaque sur la vitesse de propagation des fissures. Ils ont rapporté que les fractures de la plaque pourraient limiter la vitesse de propagation d'atteindre la vitesse caractéristique du régime *supershear*, si celles-ci se produisent pendant le régime de transition entre la propagation de fissure *anticrack* et la vitesse propagation lié au *supershear*. Il est nécéssaire d'investiguer si plusieurs fractures de plaque pourraient potentiellement ralentir la vitesse de propagation et provoquer l'arrêt, sans aucun changement dans le système au niveau de l'angle de pente et/ou des propriétés de la neige. Cependant, Trottet *et al.* (2022) ont également montré que lorsque la propagation de la fissure est en régime *supershear*, à une vitesse de propagation approximativement équivalente à la vitesse des ondes élastiques de la plaque, les fractures en tension de la plaque n'ont aucune influence sur la vitesse de propagation de la fissure. Ce résultat pourrait potentiellement indiquer que la propagation de fissure en régime *supershear* ne pourrait être arrêtée que si un changement se produit dans le système, soit la topographie, soit une hétérogénéité dans les propriétés de la neige. Des travaux supplémentaires sont nécessaires pour tester cette hypothèse. Il est impératif de comprendre les causes d'arrêt de la propagation en régime *supershear*, puisque ce régime est probablement responsable des avalanches de grande magnitude.

Problématique et objectif de recherche

L'objectif principal de cette thèse est de comprendre l'influence de la variabilité spatiale des propriétés mécaniques de la neige sur les deux composantes principales du danger d'avalanches : soit la probabilité de déclenchement par skieur et la taille de l'avalanche. Malgré de nombreuses études qui ont mesuré la variabilité spatiale de diverses propriétés mécaniques et d'indices de stabilité, une meilleure compréhension nécessite des mesures terrain à fine résolution, notamment pour comparer les patrons spatiaux des propriétés mécaniques de la plaque et de la couche faible. De plus, la modélisation spatiale avec des indicateurs micro-

topographiques représente une avenue prometteuse pour améliorer notre compréhension et notre capacité à modéliser la variabilité spatiale des propriétés mécaniques. Bien que l'influence de la variabilité spatiale de la résistance de la couche faible sur le déclenchement naturel ait été démontrée, aucune étude n'a encore exploré son effet sur le déclenchement par un skieur, en particulier en ce qui concerne la variation des propriétés de la plaque. De plus, aucune étude n'a démontré l'influence de la variabilité spatiale des propriétés mécaniques de la neige sur la propagation dynamique des fissures, qui mène ultimement à l'estimation de la taille finale de l'avalanche. Le dernier aspect de ce travail est basé sur l'hypothèse suivante, dérivée de Trottet *et al.* (2022), selon laquelle il n'y a que deux facteurs qui peuvent arrêter une propagation dynamique en régime *supershear* : 1) une hétérogénéité interne dans le manteau neigeux, 2) une variation externe telle que la topographie. Par conséquent, le dernier aspect de cette thèse s'intéresse à l'effet de l'hétérogénéité spatiale de la résistance de la couche faible sur l'arrêt complet de la propagation de la fissure dans cette couche.

Compte tenu des éléments mentionnés précédemment, cette thèse se décompose en trois objectifs spécifiques, chacun correspondant à un chapitre distinct :

1. Mesurer et estimer la variabilité spatiale de diverses propriétés mécaniques et indices de stabilité de la neige ;
2. Estimer l'influence de la variabilité spatiale de l'épaisseur de la plaque sur les deux composantes du danger d'avalanche ;
3. Comprendre l'effet de l'hétérogéinité spatiale de la résistance au cisaillement de la couche faible sur la propagation dynamique des fissures.

Chaque chapitre constitue un article scientifique répondant à un objectif spécifique de recherche. Une conclusion synthétise les résultats des chapitres, discute du fil conducteur de la thèse et répond à l'objectif principal de la thèse.

ARTICLE 1

VARIABILITÉ SPATIALE DES PROPRIÉTÉS MÉCANIQUES DE LA NEIGE À L'ÉCHELLE DE LA PENTE: IMPLICATION POUR LA MODÉLISATION MÉCANIQUE DE LA NEIGE

1.1 Résumé en français du premier article

Les avalanches de neige représentent un danger pour les infrastructures et les amateurs d'activités en montagne. Évaluer le risque d'avalanche est difficile en raison du manque d'observations sur les propriétés mécaniques de la neige et de la stabilité générale. La variabilité spatiale de ces propriétés complique la prise de décision en terrain avalancheux. Bien que les modèles de couverture de neige fournissent une simulation précise des propriétés mécaniques à une résolution d'environ 100 m, évaluer la variabilité à une échelle de pente (5-50 m) reste essentiel. Cet article explore les liens entre les propriétés mécaniques de la neige et les indicateurs microtopographiques, pouvant décrire la forme et la rugosité du terrain, et également les zones affectées par la radiation solaire ou le vent. Six échantillonages spatiales ont été menés au Canada afin de mesurer la variabilité spatiale de la neige. Les propriétés mécaniques de la neige ont été mesurées à partir d'un pénétromètre à haute résolution *SnowMicroPen* (SMP), puis des indices de stabilité ponctuelle ont été dérivés. Des vols de drone ont été effectués sur les sites d'étude pour générer des modèles 3D. Les indicateurs microtopographiques ont été calculés à partir de ces modèles 3D de la topographie. La comparaison des variogrammes et dimensions fractales a révélé des similitudes entre l'épaisseur de la plaque et la densité de celle-ci, mais différente de la résistance de la couche faible et des indices de stabilité. Les propriétés mécaniques de la neige, y compris la stabilité, ont été spatialement modélisées à l'aide de modèles GAM (*Generalized Additives Models*) avec des indicateurs microtopographiques comme covariées. Les résultats suggèrent que ces indica-

teurs peuvent estimer la variation spatiale des propriétés mécaniques, mais pas de la stabilité. La sélection des indicateurs microtopographiques était spécifique à chaque échantillonnage et chaque propriété, rendant l'extrapolation impossible. Une observation importante est qu'il y une différence entre le patron spatial de la plaque et de la couche faible pour un même échantillonnage. Ce résultats est à prendre en compte dans la modélisation mécanique de la neige.

Ce premier article, intitulé "*Snow mechanical properties variability at the slope scale: implication for snow mechanical modeling*", fut corédigé par moi-même ainsi que par mon directeur Francis Gauthier et mon codirecteur Alexandre Langlois de l'Université de Sherbrooke. Il fut accepté pour publication dans sa version finale en Février 2024 par les éditeurs de la revue *The Cryosphere*. Ma contribution en tant que premier auteur a été de conceptalisé la recherche à partir d'un état de l'art, du développement de la méthode et des résultats de recherche. Francis Gauthier et Alexandre ont contribué significativement aux développement de la recherche avec de nombreux conseils. Ils ont également contribué à la rédaction et la correction de l'article. Une version abrégée de cet article a été présentée à l'assemblée générale annuelle de *European Geophysical Union* à Vienne (Autriche) au printemps 2022, et également dans la revue *The Avalanche Journal* à l'hiver 2024.

1.2 Snow mechanical properties variability at the slope scale: implication for snow mechanical modeling

1.3 Introduction

Snow avalanches represent a natural hazard to infrastructure and backcountry recreationists across mountainous areas all across the world (Stethem *et al.*, 2003; Techel *et al.*, 2016). Snow avalanches can be divided into different types: wet, dry, non-cohesive or slab avalanches. However, dry-snow slab avalanches are the most difficult to predict and are responsible for the most fatalities (Techel *et al.*, 2016). They require a shear crack usually initiated by a person or new snowfall in a weak porous layer underneath a cohesive snow slab. Then, the crack must reach a critical size in order to self-propagate across the slope for a slab avalanche to occur. Practitioners and forecasters estimate the probability and size of an avalanche from point-scale information on weak layers and slab properties across different scales. However, the sparse nature of available observations on snowpack properties makes the forecasting of slab avalanches difficult (Hägeli and McClung, 2004). The snow spatial variability at different scales also adds complexity to this challenging task by adding uncertainty on whether the properties measured in the field are representatives of the slab and weak layer system (Schweizer *et al.*, 2008a).

The spatial variability of snow properties is well documented in climate studies (e.g. Harper and Bradford, 2003), glacier dynamics (e.g. Pulwicki *et al.*, 2018), snow hydrology (e.g. Deems *et al.*, 2006), mountain meteorology (e.g. Mott *et al.*, 2011), permafrost (e.g. Wirz *et al.*, 2011) and snow (e.g. Schweizer *et al.*, 2008a). Numerous studies have investigated the spatial distribution of snow depth and its water equivalent to support hydrological models (e.g. Deems *et al.*, 2006; Grünewald *et al.*, 2010; Schirmer *et al.*, 2011; Winstral *et al.*, 2002). Some researchers went further to estimate and analyze the spatial pattern of snow depth (Deems *et al.*, 2006; Mott *et al.*, 2011; Schirmer and Lehning, 2011; Trujillo *et al.*, 2007). They analyzed the scaling properties and the fractal dimension of the snow

depth, which can be estimated with the slope of a log-log variogram or with the periodogram of the spatial signal. The idea behind the scaling properties and fractal dimension is that many scales can define a spatial pattern instead of one scale like the correlation length in a variogram. Fractal dimension also characterizes the roughness or smoothness of a spatial pattern across multiple scales. These researchers compared the fractal dimension of snow depth with the fractal dimension of topographic indicators and vegetation. However, no studies have explored the fractal dimension of snow mechanical properties. Most studies have relied on LiDAR or manual snow probe surveys to estimate snow depth. However, snow depth is not a sufficient indicator of the conditions required for snow avalanches to occur.

There are more effective indicators, such as snow stability tests, to estimate the conditions for snow avalanches. These tests are widely used in the avalanche industry to assess snow stability and, ultimately, snow avalanche hazard. These tests provide a qualitative evaluation of the mechanical interaction between the cohesive slab and the weak layer. Some studies investigated the variability of several snow stability tests on an avalanche-prone slope (Kronholm and Schweizer, 2003; Birkeland, 2001; Campbell and Jamieson, 2007). They demonstrated a variation in the test results and spatial patterns with variograms and correlation distances around 5-20 m. However, these snow stability tests do not provide information on the snow mechanical properties of the slab and the weak layer. Additionaly, these tests are time-consuming, leading to limited spatial sampling density and extent for statistical analysis, around 30 m measurements covering 20 m. To address this limitation, the high-resolution snow micro-penetrometer (SMP) was used to characterize the mechanical and structural properties of the snow, including slab and weak layer thickness, density, elastic modulus, and microstructural strength of the weak layer (Proksch *et al.*, 2015; Löwe and van Herwijnen, 2012; Johnson and Schneebeli, 1999). Several studies characterized stability based on snow mechanical properties of the slab and the weak layer (Föhn, 1987; Gaume and Reuter, 2017; Reuter *et al.*, 2015b; Monti *et al.*, 2016; Schweizer and Reuter, 2015; Reuter and Schweizer, 2018; Rosendahl and Weißgraeber, 2020). Gaume and Reuter (2017) proposed a stability index that accounts for both failure initiation and propagation propensity, using an analytical

method applicable to SMP profiles.

The SMP was used in snow spatial studies because it can rapidly and accurately measure the mechanical properties of the snow relevant to snow stability on a slope prone to avalanche (Bellaire and Schweizer, 2011; Feick *et al.*, 2007; Kronholm and Schweizer, 2003; Landry *et al.*, 2004; Lutz *et al.*, 2007; Lutz and Birkeland, 2011). These studies reported spatial patterns of weak layer properties with correlation distances ranging from 0.5 to 20 m. However, the sampling density of the survey was between 20 to 50 SMP measurements depending on the studies and the spatial extent was covering 20 to 50 m. Reuter *et al.* (2016) used stability metrics based on SMP-derived snow mechanical properties to show spatial patterns of snow stability with a higher sampling density and extent compared to the other studies. The correlation distance obtained from this study was still in the same range as the others with some exceptions between 40 and 60 m. The differences in spatial patterns of snow instability among surveys were attributed to various meteorological processes interacting with the terrain and snow cover (e.g. Schweizer *et al.*, 2008a; Reuter *et al.*, 2016).

Based on these findings, several studies have simulated artificial spatial patterns of the weak layer in mechanical models to understand the effect of the spatial variability of the weak layer on the slope stability, given the likelihood of an avalanche (Gaume *et al.*, 2014, 2013; Kronholm and Birkeland, 2005; Fyffe and Zaiser, 2004). Gaume *et al.* (2015a) used the same method to estimate the propensity for tensile failure in the slab and the relationship with the size of avalanche release. These studies typically assumed that the spatial patterns of the weak layer ranged from 0.5 to 10 m, with the other parameters being constant for simplicity. Kronholm (2004) and Bellaire and Schweizer (2011) demonstrated that the spatial patterns of the weak layer and the slab could have different correlation distances for the same survey, resulting in some cases in a smoother slab variation than the weak layer or the opposite. However, the spatial extent of the snow sampling was relatively small, only twice as the measured correlation length, and could affect the estimation of the correlation length (e.g. Dale and Fortin, 2014; Skøien and Blöschl, 2006). This matter should be further explored

with a spatial sampling extent greater than 20 m in order to improve the implementation of snow variability in mechanical models.

Spatial patterns of snow properties can be explained and estimated by statistical models with exploratory spatial variables. In the past, environmental variables were mapped using a linear regression model and kriging with external drift. Several studies used kriging to map point snow stability, such as snow stability test results, SMP-derived mechanical properties, and stability metrics (Birkeland, 2001; Mullen and Birkeland, 2008; Reuter *et al.*, 2015a; Schweizer and Kronholm, 2007). These studies demonstrated that point snow stability can be spatially estimated using topographic indicators such as aspect, elevation, and slope angle on the regional scale. These indicators capture the complex interactions between meteorological processes and terrain features, such as snow deposition by wind and the influence of solar radiation on the snow surface between different slopes (Reuter *et al.*, 2016). However, despite the use of statistical models incorporating topographic indicators, spatially autocorrelated residuals persisted. This residual spatial variability could be attributed to other spatial phenomena at a smaller scale.

In studies focused on the slope scale, researchers successfully explained and estimated the spatial variability of snow depth, even in cases where slope angle, aspect, and elevation remained relatively constant (e.g. Deems *et al.*, 2006; Grünewald *et al.*, 2010; Pulwicki *et al.*, 2018; Revuelto *et al.*, 2020; Meloche *et al.*, 2022; Trujillo *et al.*, 2007; Winstral *et al.*, 2002). They used in their studies microtopographic indicators such as the shape of the slope (topographic position index TPI), vegetation index and microclimate indexes such as wind exposure (Winstral index) or the potential of solar radiation. Guy and Birkeland (2013) related terrain parameters to potential trigger zones, but the relationships were not unique and their study was limited to the presence of depth hoar layers. However, the presence of depth hoar crystals is insufficient to characterize snow stability, which requires more information on snow mechanical properties for the slab and the weak layer. These mechanical properties can be accurately measured with the SMP (Reuter *et al.*, 2019). Reuter *et al.* (2016) have linked

snow stability from SMP-derived snow mechanical properties with microtopography indicators at the basin scale. While previous spatial studies explored linear relations between point snow stability and topographic indicators, Reuter *et al.* (2016) suggested that the relation between point snow stability and topographic indicators could be non-linear.

The snow mechanical variability can also affect the overall slope stability with the so-called knockdown effect (Fyffe and Zaiser, 2004; Gaume *et al.*, 2014; Kronholm and Schweizer, 2003; Schweizer *et al.*, 2008a). This effect denotes that variations in weak layer strength can cause the slope to fail before the load reaches the corresponding average strength, and this effect is more prominent with a longer correlation length. Additionally, spatial variation in snow can influence the size of the avalanche release (Gaume *et al.*, 2015a). Small-scale variation can promote slab tensile failure and smaller avalanches.

It is necessary to spatially explain and estimate the mechanical properties of snow and snow stability with microtopography indicators at the slope scale. This study is based on the limitations and suggestions of Reuter *et al.* (2016), who modeled the spatial patterns of two stability metrics at the basin scale with terrain-based indicators such as slope angle, aspect and elevation. This work aims to estimate spatial variation at a smaller scale using microtopographic indicators through non-linear regression. As such, the first objective of this paper is to compare the scaling effect of the snow mechanical properties and the stability metrics for slopes prone to avalanches with different characteristics. The second objective is to spatially estimate snow spatial variability using microtopography indicators. An additional objective is to compare our dataset with two empirical power law fits from the literature (Bažant *et al.*, 2003; McClung, 2009), which estimate the shear strength of the weak layer and slab density from the slab thickness.

1.4 Data and methods

1.4.1 Study sites

In order to spatially estimate the spatial variability of snow using microtopography indicators, we selected four study sites based on their specific microtopography and microclimate context. The first study site is located on Mount Albert in Gaspésie National Park, Québec, Canada (Figure 7a). The winter climate of the region is characterized by extreme changes caused by 1) low-pressure continental systems that bring heavy snowfall up to 100 cm in 48 hours followed by Artic cold air masses with strong northwesterly winds, 2) warm and wet air masses coming from the south creating rain-on-snow events (Meloche *et al.*, 2018). The study site is named Arete de Roc (AR) and is located in a subalpine/tundra area heavily affected by wind and snow transport compared to the other sites. This site has a high ground roughness with large boulders and small trees (1 m high). The slope angle is uniform (33°) with a convex roll at the top and a concavity at the bottom (Figure 7). Two other surveys in Mt Albert at Épaule du Mur (EP) where the snow slabs and thicker and denser, were added for our additional objective, namely to verify the parameterization of snow mechanical properties based on slab thickness (Bažant *et al.*, 2003; McClung, 2009). However, these two surveys were not used in the variogram analysis and spatial modeling due to their insufficient spatial density and extent compared to the other surveys. They were added to the study to increase the data range for our additional objective.

Two study sites are in Glacier National Park, located in Rogers Pass, British Columbia, Canada (Figure 7). Our study sites are on Mount Fidelity, which receives heavy snow precipitation (Hägeli and McClung, 2003), and has a snow cover of around 2-3 m and sometimes up to 4 m. The Mount Fidelity area is classified as a transitional snow and avalanche climate influenced by warm and wet air masses from the Pacific that bring heavy snowfall and cold air masses from the north, leading to the development of persistent weak layers (Hägeli and McClung, 2003). This study area experiences annually several persistent weak layers

consisting of buried surface hoars or facets, relevant for stability assessment. The first study site at Mount Fidelity is located just above the tree line at 2020 m a.s.l on a shoulder named Round Hill (RH). This site is an alpine area with low soil roughness (Figure 7). The slope angle is relatively low (near 25°), with long and smooth convex rolls around 20-30m. The last study site, Jim Bay Corner (JBC), is located below the tree line at 1830 m a.s.l. It is an open forested area with relatively low ground roughness with small shrubs. The site has 10 m tall trees which create some shaded areas and the slope angle is relatively constant (near 20°) with small convex rolls around 5-10 m (Figure 7).

1.4.2 Data collection and sampling strategies

For the spatial analysis, this study presents four snow spatial surveys collected during winter 2021-2022 (Figure 7): 25 February 2022 at the Arête de Roc site (AR22-PP), 27 January 2022 at the Round Hill site (RH22-PP), 19 January 2022 at Jim Bay Corner (JBC22-SH), and 24 January 2022 at Jim Bay Corner (JBC22-PP). Two more surveys were added for the comparison of different parametrizations of snow mechanical properties: 24 Janvier 2019 at Épaule du Mur (EP19-FC) and 29 Février 2020 at Épaule du Mur (EP20-DF). Snow mechanical properties were measured using the high-resolution SMP. To compare the spatial patterns of snow mechanical properties and snow stability, each SMP measurement was made following a sampling scheme, according to the concept of the scale triplet which is the support, spacing, and extent described by Blöschl and Sivapalan (1995). The support is the diameter of the SMP tip which is 5 mm, guaranteeing a proper estimation of the microstructural properties of the snow. A minimum spacing of 2 m and a study site extent covering around 60 to 100 m were chosen to allow the spacing to be at least half of the expected correlation length and the extent to be two to five times the expected correlation length. The expected correlation length has been reported to be around 5-20 m from several studies (Bellaire and Schweizer, 2011; Lutz *et al.*, 2007; Reuter *et al.*, 2016; Schweizer and Reuter, 2015). This method ensures a reliable estimate of the spatial pattern, defined by both spa-

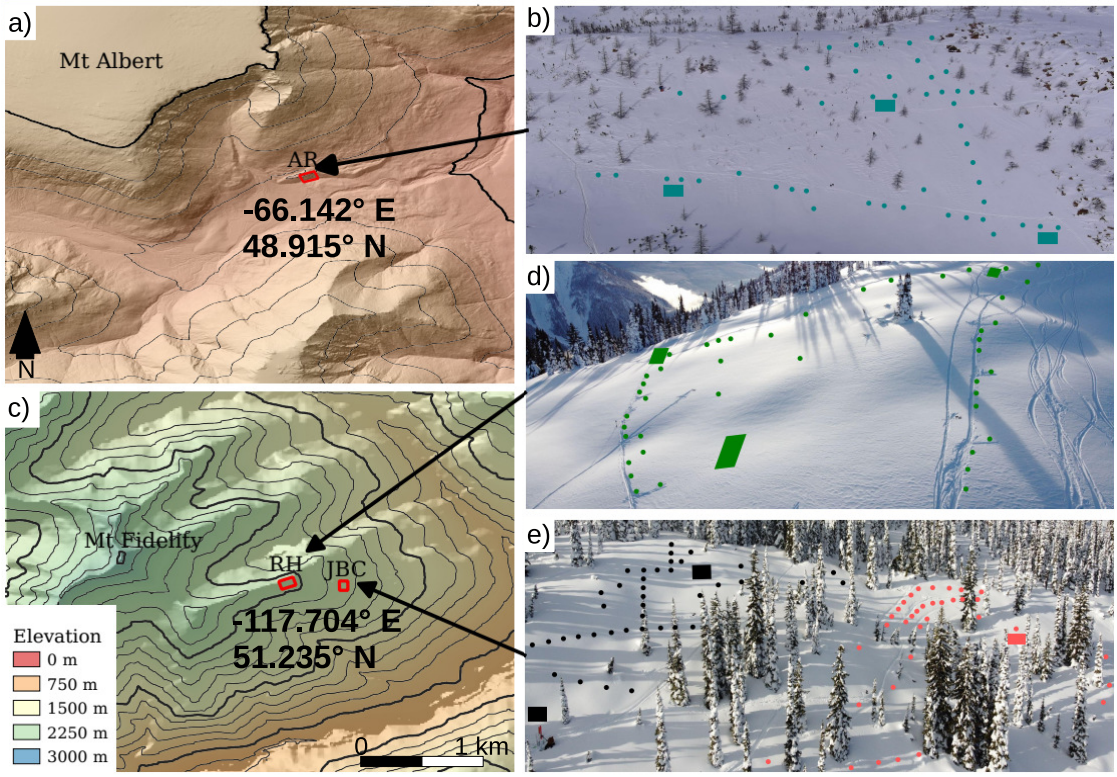

Figure 7 – Map of the study area of a) Mount Albert, Québec, Canada, with the study site b) Arête de Roc with the 25 February 2022 survey in blue (AR). c) Mount Fidelity study area, British Columbia, Canada, with sites: d) Round Hill (RH) with the 27 January 2022 survey in green and e) Jim Bay Corner (JBC) with the 19 January 2022 survey in red and the 24 January 2022 survey in black. The aerial photography is from the UAV flight of each study site and the snow spatial sampling is represented by circles for the locations of SMP measurements and the squares are the snow profile locations.

tial variance and autocorrelation distance (Skøien and Blöschl, 2006; Dale and Fortin, 2014). Our sampling scheme also needs to be adequate for the second objective, which is the spatial estimation of snow mechanical properties and stability metrics using microtopographic indicators. Therefore, the sampling scheme was adjusted for each specific study site to obtain a representative distribution of microtopographic indicator values while respecting the scale triplets mentioned above. The sampling was conducted by randomly traversing the study site while adhering to the minimum spacing, and also by characterizing the down and cross-slope for an isotropic sampling. The sampling was stopped when the study site was almost covered with 60 to 80 SMP measurements. The resulting sampling is shown in Figure 7. Random sampling contributes to obtain a robust estimation of the correlation length with limited SMP measurements (Kronholm and Birkeland, 2007; Skøien and Blöschl, 2006).

To ensure an accurate interpretation of the SMP signal, the weak layer needed to be identified and characterized from a snow profile. Full characterization of the snow stratigraphy was not needed for our analysis, so a shorter version of snow profile was used to optimize the time in the field. Two or three snow profiles were conducted per snow spatial survey, spaced at least 20 m apart and positioned next to SMP measurements (Figure 7). In each test snow profile, we first performed two compression tests to identify the weak layer (Canadian Avalanche Association, 2016). The weak layer was attributed to the uppermost compression test results consistent in both compression tests. Then, we visually characterized the types and sizes of the snow grains of the weak layer. Finally, a propagation saw test was performed to measure the critical crack length of the weak layer (Gauthier and Jamieson, 2008). Layers situated above the weak layer were considered part of the slab. This assessment allowed us to accurately identify the weak layer in the nearest SMP profile and subsequently in the remaining SMP profiles. Each snow measurement, SMP or snow profile, was georeferenced using a GNSS receiver with centimeter accuracy. Furthermore, for each study site, aerial imagery was captured by a quad-rotor UAV with RGB sensor to characterize the topography both in the summer and winter on the same day as the spatial snow survey. Ground / surface models were generated using a *structure from motion (sfm)* photogrammetry algorithm

(Westoby *et al.*, 2012) with ground and snow control points, ensuring georeferenced models with centimeter accuracy (< 2 cm in x,y and < 5 cm in z).

1.4.3 Snow mechanical properties and stability metrics

This section describes the workflow used to process every SMP profile, extracting several snow mechanical properties needed for stability assessment. Three stability metrics were derived from these snow mechanical properties. Figure 8 presents the summary of this workflow.

1.4.3.1 SMP signal processing and snow properties

Each SMP signal was visually interpreted to identify distinct layers. First, the weak layer was identified on the SMP signal next to the snow profile, based on the failure depth in the corresponding compression test. Then homogeneous layers above the weak layer were classified into slab layers (Sl_1, Sl_2,...Sl_i). This procedure was repeated for the remaining SMP signal. To obtain the macroscopic mechanical properties for each snow layer, the SMP signal was analyzed using a Poisson shot noise model with a moving window of 2.5 mm (Löwe and van Herwijnen, 2012). This analysis was used to recover microstructural parameters, including the peak force F, the deflection at rupture ζ, and the element length L (Löwe and van Herwijnen, 2012). Then, each structural and macroscopic snow mechanical property necessary for estimating the stability metrics can be retrieved: the slab thickness D, the weak layer thickness D_{wl}, the slab density ρ, the weak layer density ρ_{wl}, the elastic modulus of the slab E and the shear strength of the weak layer τ_p. Specifically, the slab thickness D and the weak layer thickness D_{wl} are directly extracted from the SMP profile. Slab density ρ and weak layer density ρ_{wl} are derived using the F and L parameters based on the method

proposed by Proksch *et al.* (2015):

$$\rho = 295.8 + 65.1ln(F) - 43.2ln(F)L + 47.1L, \tag{1.1}$$

where ρ is in kg m^{-3}, L in mm and F in N. The coefficients were obtained by Calonne *et al.* (2019). The slab density ρ was determined as the mean value of all sub-slab layers above the weak layer, while ρ_{wl} is the mean value of the signal inside the weak layer. The effective macroscale elastic modulus of the slab (E) was derived with the new formulation recently adapted by Reuter *et al.* (2019), originally developed by Johnson and Schneebeli (1999):

$$E = 880\frac{F\zeta}{L^3} \cdot \frac{\zeta}{L}. \tag{1.2}$$

The SMP cannot specifically measure the shear strength of the weak layer due to the mixed-mode loading on the weak layer caused by the slope angle in the field. Reuter *et al.* (2015a) previously assumed that the shear strength of the weak layer τ_p is approximately equal to the microstructural strength of the element defined by $\sigma^{th}_{micro} = F/L^2$. We retained the same assumptions, but we used the macroscale strength σ^{th}_{macro} to estimate τ_p. The formulation is similar, but scaled with the number of active contacts $\frac{\zeta}{L}$ over the 2.5 mm processing moving window of the SMP, following the formulation of Johnson and Schneebeli (1999):

$$\sigma^{th}_{macro} = \frac{F}{L^2} \cdot \frac{\zeta}{L}. \tag{1.3}$$

1.4.3.2 Stability metrics

The skier propagation index (SPI) proposed by Gaume and Reuter (2017) was used to describe the skier stability. The SPI is defined as the ratio of two lengths: the skier crack length l_{sk} and the critical crack length a_c. The skier crack length represents the length of the crack in the weak layer induced by the weight of a skier on top of a slab. The critical crack length is the length of the crack required for the onset of crack propagation. The skier crack

length is computed by solving the equation: $\tau + \Delta\tau = \tau_p$, where $\tau = \rho g D \sin\psi$ is the shear stress due to the slab weight with g as the gravitational acceleration. The stress due to the skier $\Delta\tau$, was originally defined by Föhn (1987), and refined by Monti *et al.* (2016):

$$\Delta\tau = \frac{2R\cos\alpha\sin^2\alpha\sin(\alpha+\psi)}{\pi D_e}, \tag{1.4}$$

where R is the skier load set to 780 N and ψ is the snow surface slope angle derived from UAV imagery. The angle α is defined as the angle between the point at the snow surface under the skier load to the point of maximum induced shear stress at the weak layer. Additionally, D_e is the new multilayered slab thickness proposed by Monti *et al.* (2016), considering that slabs are often made up of multiple layers with different properties, influencing stress redistribution (Habermann *et al.*, 2008). The computation of D_e follows Equations 2,3,4 in Monti *et al.* (2016), based on each layer elastic modulus E that composed the slab. In order to determine l_{sk}, the roots of the equation are found where $\tau + \Delta\tau = \tau_p$. The roots define two angles, α_1 and α_2, describing the area of stress from the surface beneath the skier to the weak layer. From these two angles, the skier crack length is calculated (l_{sk}) with the following equation (Gaume and Reuter, 2017):

$$l_{sk} = D_e\left[\frac{1}{\tan\alpha_1} - \frac{1}{\tan\alpha_2}\right]. \tag{1.5}$$

It is important to note that D_e was used exclusively in Eq. 1.4-1.5, and the slab thickness D was used in the a_c formulation (explained below) and in both spatial analysis and estimation.

The critical crack length is computed using the formulation from Gaume *et al.* (2017):

$$a_c = \Lambda\left[\frac{-\tau + \sqrt{\tau + 2\sigma(\tau_p - \tau)}}{\sigma}\right], \tag{1.6}$$

where $\sigma = \rho g D\cos\psi$ and Λ is a characteristic length of the system defined by:

$$\Lambda = \sqrt{\frac{E' D D_{wl}}{G_{wl}}}, \tag{1.7}$$

with $E' = E/(1-\nu^2)$, ν is the Poisson's ratio set to 0.3, D_{wl} is the weak layer thickness and G_{wl} is the shear modulus of the weak layer. However, Richter *et al.* (2019) proposed to change the formulation of Λ by excluding D_{wl} due to its sensitivity in snow cover modeling (SNOWPACK), which is also challenging to visually interpret in an SMP profile. Instead, they proposed a parameterization based on the weak layer density and optical grain size, replacing the ratio $\frac{D_{wl}}{G_{wl}}$ by ω (Eq. 1.8) into the characteristic length $\Lambda = \sqrt{E' D\omega}$. They normalized the optical grain size with a critical grain size (1.25 mm) from Schweizer *et al.* (2008b). The critical grain size of 1.25 mm was determined with a statistical analysis comparing weak layer properties from profiles classified as stable or unstable. We adapted this approach, by replacing the optical grain size with the SMP parameter L. Following Pielmeier and Marshall (2009), we used $L_0 = 1.09$ mm. Consequently, we obtained the following formulation for ω:

$$\omega = 4.7 \times 10^{-9} \left(\frac{\rho_{wl}}{\rho_{ice}} \cdot \frac{L_{wl}}{L_0} \right)^{-2.1} \text{[mPa}^{-1}\text{]} \tag{1.8}$$

where ρ_{wl} is the weak layer density, L_{wl} is the element length L of the SMP signal analysis averaged over the thickness of the weak layer. The values are slightly different from those reported by Richter *et al.* (2019). Additionally, critical crack lengths were obtained in the field with the propagation saw test (PST) conducted next to the snow profile for each snow sampling survey. We compare the critical crack lengths a_c from the SMP with the critical crack length from the PST tests to assess the precision of our approach. However, we do not intend to accurately predict the stability metrics, but to model their spatial variation. Finally, the skier propagation index SPI is defined as the ratio of the critical crack length (a_c) and the skier crack length (l_{sk}) (Gaume and Reuter, 2017):

$$SPI = \frac{a_c}{l_{sk}} \tag{1.9}$$

A snowpack loaded by a skier is considered stable for SPI > 1 and unstable for SPI < 1.

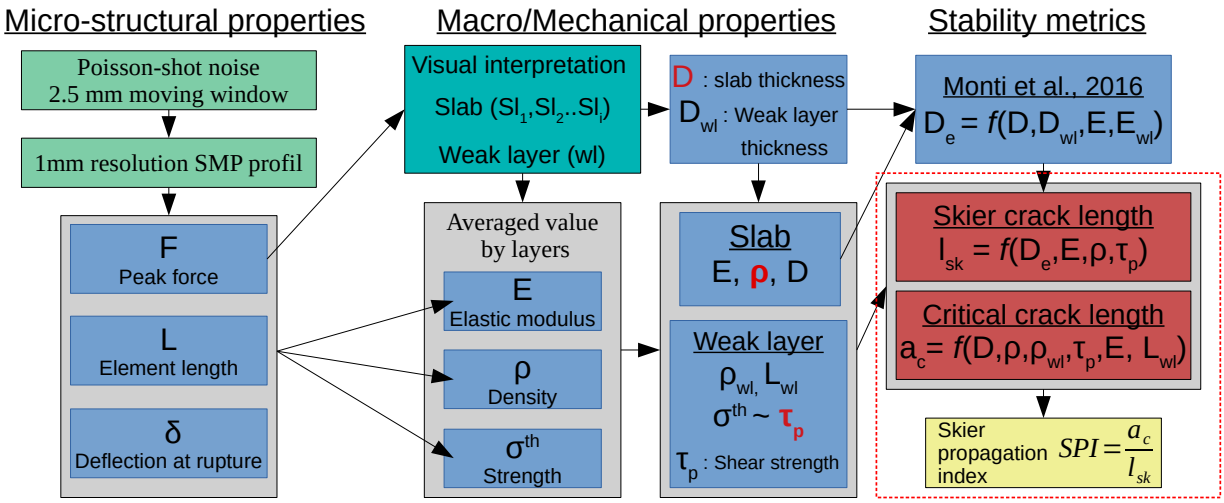

Figure 8 – Schematic representation of the workflow used to process the SMP signal to obtain the snow mechanical properties and the stability metrics. The variables and the dashed square in red are the snow mechanical properties and the three stability metrics that will be analyzed and spatially estimated in this work. The parameters of the weak layer are denoted by the subscript X_{wl}.

1.4.4 Analysis of spatial pattern

The first objective of this paper is to compare the scaling effect on snow mechanical properties and stability metrics for slopes prone to avalanches with different characteristics. We choose three mechanical properties, the slab thickness D, slab density ρ and the shear strength of the weak layer τ_p, as well as the three stability metrics described above, which are the skier crack length l_{sk}, the critical crack length a_c and the skier propagation index SPI. The spatial patterns of each snow mechanical property and stability metric were compared between the snow spatial surveys as an exploratory analysis. The omnidirectional experimental variogram γ was computed following the equation for a variable y (Chilès and Delfiner, 1999).

$$\gamma(d) = \frac{1}{2N}\sum_{i=1}^{N}[(y_i + d) - y_i]^2 \tag{1.10}$$

with N = number of observations and d = distance between observations. The experimental variogram is defined by three parameters, the nugget or the non-spatial variance, the sill, which is the spatial variance, and the range or correlation length, which is the distance where the variance levels out. While the sill is difficult to compare across properties due to differing units, the correlation length is comparable as it shares the same unit. The correlation length provides insight into the scale of spatial variation. Four types of covariance models (Gaussian, Exponential, Spherical, Matern) were fitted to the experimental variogram using iterative reweighted least squares estimation with function fit.variogram from the *gstat* package (Pebesma, 2004) in Rstudio (R Core, 2013). Furthermore, the fractal dimension, which expresses the roughness or complexity of a surface (2-3D) in a noninteger dimension (Gao and Xia, 1996), was estimated from the variogram. We estimated the slope ϕ of the transformed log-log variogram and then obtained the fractal dimension (Gao and Xia, 1996):

$$d_{fractal} = 3 - (\frac{\phi}{2}) \tag{1.11}$$

1.4.5 Spatial modeling

1.4.5.1 Covariates processing

The second objective of this study is to explore the link between microtopographic indicators and snow mechanical properties and stability metrics in order to estimate snow spatial variability. The scale of these microtopographic indicators is defined by the size of the moving window used to derive them. Different sizes of moving windows were used to allow for a multiscale approach describing the spatial process (e.g. Revuelto *et al.*, 2020; Meloche *et al.*, 2022; Veitinger *et al.*, 2014). The choice of different window sizes used in this study is based on the literature and will be developed further below. Microtopography indicators are used as exploratory spatial variables and will be referred to as covariates in the spatial model. These covariates were derived from a digital terrain and surface model (DTM/DSM)

generated through photogrammetry using the UAV imagery. The classification between the ground and the vegetation was performed manually through visual inspection, given the small extent of the study site. Additionally, canopy models were generated for each snow study site by differentiating the DSM from the DTM. Snow depth maps were generated using a snow surface model (DSM_{snow}) and compared to the DTM model to retrieve the snow depth for each spatial snow survey.

All covariates were raster data with an original spatial resolution below 0.1 m and were upscaled to a spatial resolution of 0.5 m. The final resolution of the spatial model was the same as the covariates. The choice of covariates was based on multiple studies that focus on spatial variation of snow depth that will be described below. Three groups of covariates, terrain shape, vegetation and microclimate, are presented in Table 1. Two indicators were chosen to describe the terrain shape, the topographic position index TPI and the vector ruggedness measure VRM. The TPI is a slope descriptor indicating ridges, valleys or slopes at a given scale, referencing the position in elevation relative to neighboring cells (Weiss, 2001). The TPI was measured between a minimum radius and a maximum radius with weighted distance from the maximum radius (Table 1). The vector ruggedness measure VRM indicates the ruggedness of the terrain independently of slope angle and aspect. The ruggedness was derived as the sum of elevation differences with neighboring cells, but then decoupled with slope angle and aspect, which means that a flat and a steep slope could be homogeneous with low ruggedness (Sappington *et al.*, 2007). These two indicators were used to explain and estimate snow depth (e.g. Revuelto *et al.*, 2020; Meloche *et al.*, 2022; Veitinger *et al.*, 2014). The sizes of the different moving windows were chosen based on the values used in these studies to have a multiscale approach (Table 1). We used the slope angle and convexity of the terrain as exploratory variables. Vegetation also has an impact on the spatial variation of snow depth (Deems *et al.*, 2006), we choose to use the canopy height for the influence of shrubs (around 0.3 and 0.5 m) and small trees (around 1 or 2 m) because snow cover can be up to 3 or 4 m in some areas of JBC and RH. Only trees above 5 m were masked from the study sites. We used the radial proximity to vegetation greater

than 2 m, to represent proximity to trees. Some authors also found that solar radiation (e.g. Lutz and Birkeland, 2011) and wind exposure (e.g. Winstral *et al.*, 2002) were important in spatially estimating snow properties. We selected as covariates the potentially incoming solar radiation. The algorithm simulated over a DSM (including trees), the trajectory of the sun in the sky based on the time of the year and the latitude of the study site. The covariate represents direct insolation (shade and sunshine areas), calculated over a month prior to the survey. The Winstral index or upwind maximum slope parameter S_x represents the shelter or exposure areas provided by the terrain upwind of each pixel (Winstral *et al.*, 2002). The upwind terrain was defined with the maximum search distance and the prevalent wind direction based on the mean wind direction from the nearest weather station of the study sites over the winter. The snow depth values from the DSM_{snow} were taken as covariates. The last covariates used were the spatial coordinates (easting and northing). The fitting of a smooth function to spatial coordinates, explained in the following section, will take into account the residual spatial autocorrelation (Nussbaum *et al.*, 2017). The processing of the covariates involved the use of the geoprocessing library SAGA (Conrad *et al.*, 2015), Qgis 3.14, and a Python implementation of the Winstral index S_x according to Winstral *et al.* (2002).

1.4.5.2 General additive model

General additive models (GAMs) can represent non-linear relationships between the covariates and the response variable. GAMs have been used in the past for spatial estimation of environmental variables (Nussbaum *et al.*, 2017). They produce good results while remaining easy to interpret compared to more complex tree classification methods and machine learning algorithms (Nussbaum *et al.*, 2017). A GAM model can be described as a generalized linear model with a linear prediction involving a sum of smooth functions s of

Table 1 – Covariates used for the spatial models with the source (DTM/DSM) and additional parameters.

Covariates	Abbr	Additional parameters	Processing library
Topographic Position index	TPI515	radius min/max = 5/15 m	SAGA
Topographic Position index	TPI2550	radius min/max = 25/50 m	SAGA
Vector ruggedness measure	VRM5	moving window = 5 m	SAGA
Vector ruggedness measure	VRM15	moving window = 15 m	SAGA
Vector ruggedness measure	VRM25	moving window = 25 m	SAGA
Terrain slope angle	Slope	NA	Qgis
Convexity	Convex	scale = 25	SAGA
Canopy height	Cano	DSM/DTM	Qgis
Distance to canopy	Dist-cano	Radial proximity to trees > 2 m	SAGA grid tools
Incoming solar radiation	Rad	Potential solar radiation summed up 30 days before sampling	SAGA
Winstral index	S_x	Search distance = 100 m	Python
Snow depth	H_s	$DSM_{snow} - DTM$	Qgis
Easting and northing	xy	NA	Python

covariates X (Wood, 2006):

$$Y_i = Z_i\xi + s_1(X_{1i}) + s_2(X_{2i}) + s_3(X_{3i}) + ...s_j(X_{ji}) \tag{1.12}$$

where Y_i is a response variable, Z_i is a row of the model matrix for any strictly parametric component with vector parameter ξ. Each smooth function or spline s_j can be expressed through a basis expansion b with a weight parameter η_k and the subscript k defining the order of the basis expansion.

$$s_j(X_j) = \sum_{k=1}^{k} \eta_k b_k(X_j) \tag{1.13}$$

Each smooth function represents a combination of linear terms fitted to a covariate X_j. The order of the smooth function determines the non-linear degree or the *wigliness* of the fit-

ted GAM. We kept a low order ($k = 3$) to avoid overfitting and non-realistic variation. While stepwise procedures are commonly used, they lack stability compared to newer methods such as shrinkage and boosting procedures (Hesterberg *et al.*, 2008). We used the double penalty approach as a shrinkage method proposed by Marra and Wood (2011), which adds a smoothing parameter for each covariate spline function. This method is implemented in the *mgcv* package in R. We applied this method for six response variables Y: the three snow mechanical properties (slab thickness D, slab density ρ_{slab}, and the shear strength of the weak layer τ_p) and the three stability metrics (skier crack length l_{sk}, critical crack length a_c and skier propagation index SPI). The estimation of these response variables used GAM's with the 13 covariates listed in Table 1.

The performance of our models was evaluated with the root mean square error RMSE and the mean absolute error MAE using a 10-fold cross-validation approach. This involves randomly splitting the sample into 10 subsets, fitting the model to the 9 subsets, comparing it to the remaining subset, and repeating this procedure 10 times. The percentage of deviance explained (sum of squared errors) was computed to demonstrate the amount of total variance accounted by the model, this metric is more suited for non-linear model compared to R^2, which is still shown in the results for comparison. Once our model was fitted (and cross-validated) and the covariates were selected, the response variable was estimated for every location at each study site on a 0.5 m resolution grid. A smaller resolution will not be in line with the assumption of homogeneous snowpack for the computation of the skier crack l_{sk} and the critical crack length a_c. All statistical computations were performed in R (R Core, 2013).

1.5 Results

1.5.1 Summary of spatial snow surveys

The first spatial snow survey was conducted at the AR site. A weak layer of precipitation particles with an observed grain size of 0.5 - 1 mm was investigated on 25 February

Table 2 – Summary for the snow measurements of all spatial surveys. The results of the compression test CT results and the propagation saw test PST are shown according to the standards of Canadian Avalanche Association (2016).

Surveys	Date	Mean D & ρ	Weak layer	Nb SMP	Extent	CT	PST (m)
AR22-PP	25 Feb 2022	0.28 m & 252 kg m^{-3}	PP 0.5-1 mm	45	71 m	CTM11 (RP) down 0.25 m	0.9/1.5 END
						CTH23 (RP) down 0.54 m	1.42/1.5 END
						CTH22 (RP) down 0.35 m	1.22/1.5 END
RH22-PP	27 Jan 2022	0.19 m & 171 kg m^{-3}	PP 0.5-1 mm	64	116 m	CTM19 (RP) down 0.22 m	0.8/1.5 END
						CTM19 (RP) down 0.22 m	0.28/1.5 SF
						CTH22 (RP) down 0.24 m	1.38/1.5 END
JBC22-SH	19 Jan 2022	0.39 m & 188 kg m^{-3}	SH 1-2 mm	53	102 m	CTH21 (RP) down 0.39 m	1.28/1.5 END
						CTM12 (RP) down 0.5 m	1.46/1.5 END
JBC22-PP	24 Jan 2022	0.21 m & 166 kg m^{-3}	PP 0.5-1 mm	55	74 m	CTM13 (RP) down 0.25 m	1.24/1.5 END
						CTM16 (RP) down 0.24 m	1.41/1.5 END
EP20-DF	29 Fev 2020	0.32 m & 241 kg m^{-3}	DF 0.5-1 mm	38	45 m	CTH23 (RP) down 0.38 m	-
						CTH24 (RP) down 0.45 m	-
EP19-FC	24 Jan 2019	0.85 m & 333 kg m^{-3}	FC 1 mm	22	48 m	CTH20 (SP) down 0.82 m	-
						CTM22 (RP) down 0.88 m	-

2022 (AR22-PP), with 45 SMP measurements and a spatial extent of 71 m. The average slab thickness was 0.28 m and the mean slab density was relatively high: 252 kg m^{-3} (Table 2).

At the RH site (RH22-PP), a weak layer of precipitation particles with an observed grain size of 0.5 to 1 mm was found beneath a relatively soft snow slab. The mean slab thickness was 0.19 m and the mean density was 171 kg m^{-3}. This survey, conducted on 27 January 2022, included 64 SMP measurements and covered a spatial extent of 116 m. The slab consisted of one homogeneous layer of storm snow, and both the slab and the weak layer originated from the same meteorological event.

We conducted two spatial snow surveys at the JBC site in two different areas of the site. The first survey at this site took place on 19 January 2022 (JBC22-SH) when there was a persistent weak layer of buried surface hoar of size 1-2 mm. The slab was composed of multiple layers with a mean slab thickness of 0.39 m and a mean density of 188 kg m^{-3} above the surface hoar crystals. This survey consisted of 53 SMP measurements, covering a spatial extent of 102 m. The second survey (JBC22-PP) was characterized by a weak layer of precipitation particles buried under a fresh snow slab of 0.21 m thickness and an average slab density of 166 kg m^{-3}, deposited by the same meteorological event as RH22-PP. This survey included 55 SMP measurements and the spatial extent was 74 m (Table 2).

The last two surveys presented in Table 2 were added to the study to increase the data range in Figure 9. The snow spatial survey EP20-DF had a mean slab thickness of 0.32 m and slab density of 241 kg m^{-3}, similar to AR22-PP. The snow spatial survey EP19-FC recorded the highest mean slab thickness of 0.85 m and the highest mean slab density of 333 kg m^{-3}. Although the number of SMP measurements and spatial extent were not sufficient for spatial analysis, these surveys provided valuable data points characterized by larger slab thickness D, contributing to a fair assessment of the two empirical power law fits (Bažant *et al.*, 2003; McClung, 2009).

Figure 9 shows slab density ρ and weak layer shear strength τ_p in relation to slab thick-

ness D. These relations are often established, as snow density and snow strength should increase as the slab load increases. We fitted two power laws to our SMP-derived dataset, and compared them with two other empirical power laws commonly used in the literature (Bažant *et al.*, 2003; McClung, 2009). Figure 9 indicates a poor fit for both parameters (ρ and τ_p). The power law from McClung (2009) was better suited for the two surveys characterized with relatively low density ($\rho < 250$ kg m^{-3}), which were conducted at Mount Fidelity (Figure 9-a). The surveys with higher density ($\rho > 250$ kg m^{-3}) were on Mount Albert, which is a heavily wind-exposed area that could explain these highly dense slabs. Figure 9-b shows some surveys aligned with the two power laws, especially the surveys from Mount Fidelity (circles). However, the Mount Albert surveys exhibited more variability compared to the Mount Fidelity surveys. In general, our data set fitted poorly with the power laws from the literature, and a lot of variability remained in each survey. The intra-survey variability and implication for snow mechanical modeling will be discussed in section 4.1.

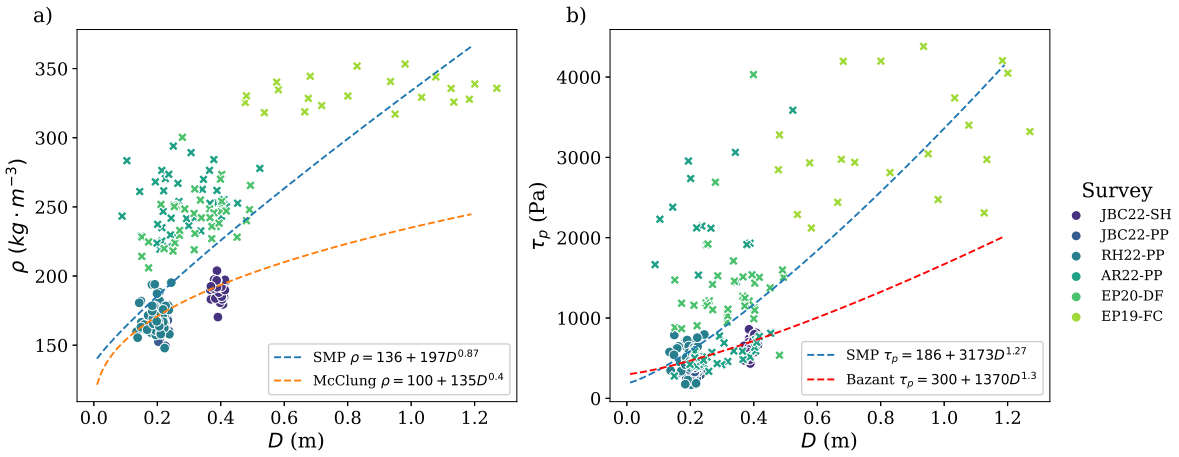

Figure 9 – SMP-derived a) slab density ρ_{slab} and b) weak layer shear strength τ_p in relation to the slab thickness D for each SMP measurement of all spatial survey. The full circles represent the SMP values from Mount Fidelity, British Columbia, and the crosses are from the surveys from Mount Albert, Québec. A power law in blue was fitted to the SMP-derived values of all surveys, with $R^2 = 0.5$ for ρ, and $R^2 = 0.4$ for τ_p, respectively. The orange power law in (a) represents ρ compared to D, with an initial density of 100 kg m^{-3} from McClung (2009). The red power law is the power law in (b) for τ_p from Bažant *et al.* (2003) who used the Mohr-Coulomb relation with an initial cohesion of 300 Pa (Gaume *et al.*, 2014).

1.5.2 Comparison of spatial patterns

For all spatial snow surveys, the empirical variogram showed smaller correlation lengths for the slab thickness compared to other properties, ranging from 5 to 10 m (Figure 10). The variograms for the slab density exhibited correlation length in the same range as for the slab thickness, particularly for JBC22-PP and RH22-PP, with 5 and 8 m, respectively. These two spatial snow surveys had the same weak layer and slab meteorological deposition event characterized by a new snow instability. The correlation length for the slab thickness and slab density at AR22-PP was 10 m, with the same type of new snow instability. The variogram for the slab density at JBC22-SH was the only survey that had a longer correlation length of 34 m. Variograms of the slab density from JBC22-SH, JBC22-PP and AR22-PP appeared to exhibit fractal characteristics. These variograms showed a distinct plateau of variance around 10-20 m, followed by an increase in variance around 30-40 m, indicating a multiscale pattern around these two distances (10 and 40 m). Variograms of the weak layer shear strength indicated a longer correlation length around 20 m compared to the ones of slab properties, which were around 10 m. In the JBC22-PP and RH22-PP surveys, which shared the same meteorological deposition event, the variance stabilized at 20 m without any further increase in variance. The other surveys (JBC22-SH and AR22-PP) had longer correlation lengths and showed fractal characteristics with no stabilization in variance as the sampling distance increased. The primarily used variogram models were spherical and exponential, characterized by a rapid increase in variance for short distances. These models tend to be less smooth than Gaussian models, which have a smaller variance for short distances. Gaussian models were fitted for slab thickness at JBC22-SH and slab density at JBC22-PP. In general, the correlation lengths tended to be shorter for the thickness and density of the slab compared to the shear strength of the weak layer in each snow spatial survey.

At first glance, all the correlation lengths for the stability metrics were longer than those for the slab properties. Surveys at the Jim Bay Corner (JBC22-SH and JBC22-PP) showed correlation lengths around 20 m (Figure 11). The other two surveys (AR22-PP and RH22-PP)

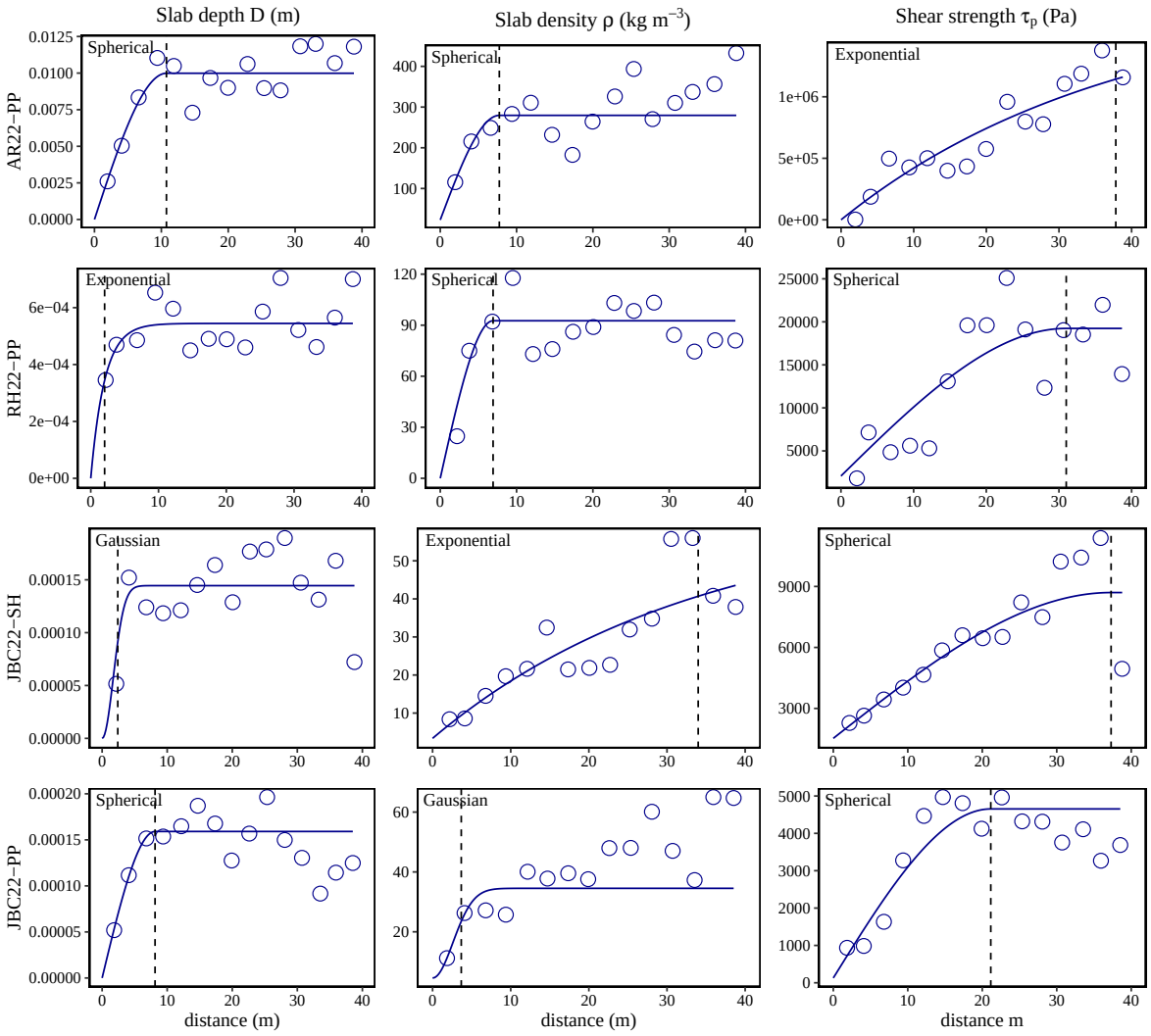

Figure 10 – Experimental variograms (circles) and fitted variogram models (line) for the snow mechanical properties. Note that the square root of the variance gives the absolute variation. The vertical dashed line in each variogram is the range for the fitted variogram model to the experimental variogram.

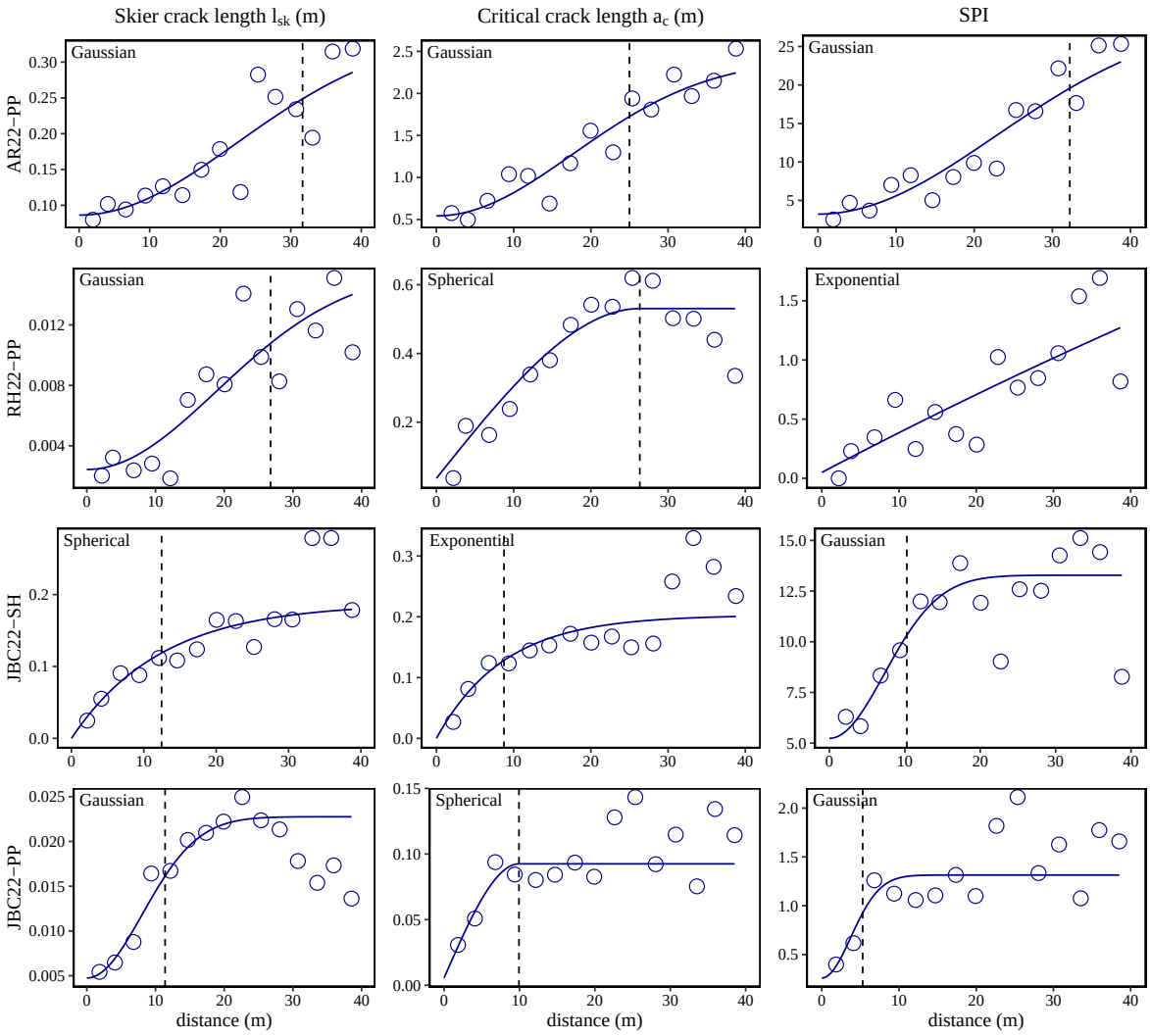

Figure 11 – Experimental variograms (circles) and fitted variogram models (line) for the stability metrics. Note that the square root of the variance gives the absolute variation. The vertical dashed line in each variogram is the range fitted for the theoretical variogram (line) to the empirical variogram (circles).

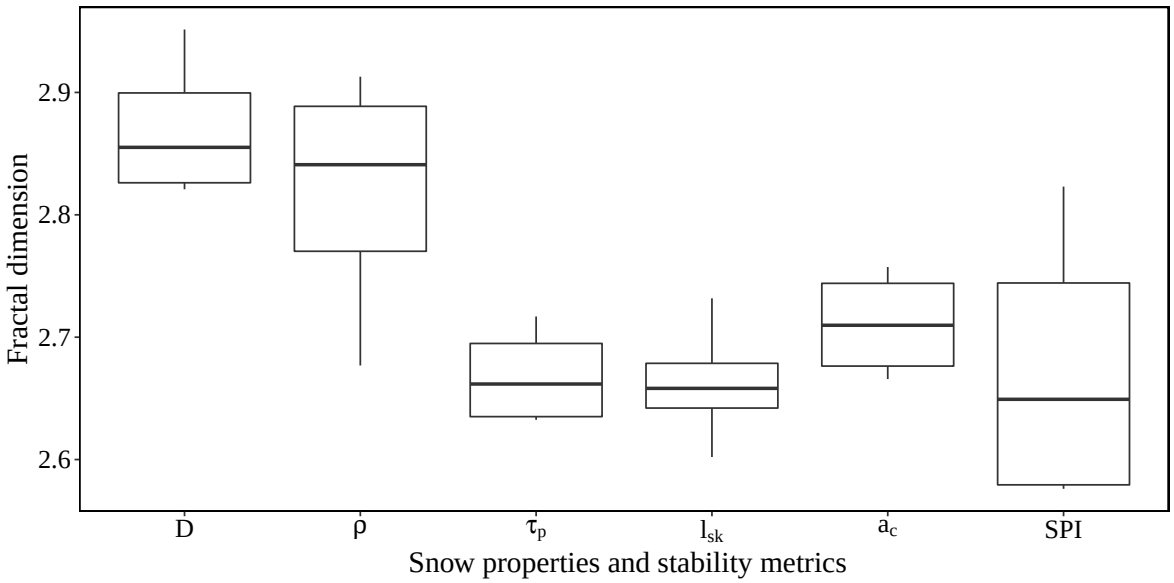

Figure 12 – Boxplot of fractal dimension for snow mechanical properties and stability metrics with the four surveys in each boxplot. The symbols corresponds to : Slab depth D, slab density ρ, weak layer shear strength τ_p, skier crack length l_{sk}, critical crack length a_c, and the skier propagation index SPI

exhibited an empirical variogram that did not show a clear plateau of variance to determine a correlation length. These surveys either had a longer correlation length than the spatial extent of the sampling or showed a fractal behavior over multiple scales. The correlation lengths of the stability metrics ranged from 10 to 20 m, which is longer compared to the slab properties (Figure 11). The most frequently used variogram model was spherical, but Gaussian models were also applied for the skier crack length (JBC22-PP, RH22-PP, AR22-PP) and skier index (JBC22-SH, JBC22-PP). Gaussian models were more frequently fitted to stability metrics than to snow properties, suggesting smoother spatial patterns for the stability metrics. The variogram for the stability metrics exhibited more similarities with the variogram of the weak layer shear strength rather than the slab properties.

The fractal dimensions for the snow properties indicated a difference in surface complexity between the slab properties, the weak layer properties, and the stability metrics (Figure 12). The slab properties had higher fractal dimensions, around 2.85, indicating a higher

surface complexity, compared to the weak layer and the stability metrics, which had a similar fractal dimension around 2.7. Despite the stability metrics being computed from both slab mechanical properties and weak layer properties, their fractal dimension values were closer to those of the weak layer rather than the slab. These results suggest that the spatial patterns of the stability metrics were more similar to those of the weak layer than those of the slab properties.

1.5.3 Spatial modeling

The spatial models created by the GAMs explained some of the variance of the response variable, but far from entirely. The R^2 and the percentage of deviance explained ranged from 0.17 to 0.84 and from 22 to 84 % (Table 3 - 4). On average for all models, the R^2 was approximately 0.5 and the percentage of deviance was 55 %. The average R^2 was 0.47 for snow properties and 0.55 for stability metrics, and the average percentage of deviance explained was the same at 55 %. The performance of the models was assessed with a 10-fold cross-validated RMSE and MAE. The cross-validated RMSE and MAE for the slab thickness D were mostly 1-2 cm except for 12 cm at AR22-PP and were around 4 to 27 kg m^{-3} for the slab density. The RMSE and MAE for the shear strength ranged from 30 to 128 Pa except for 752 Pa for AR22-PP, but this snow spatial survey was also the one which had the highest variance (500 to 3500 Pa).

The spatial surfaces estimated by the GAM models in JBC22-SH for the snow mechanical properties are presented in Figure 13. The estimated surfaces for the slab thickness and density exhibited a similar variation with comparable maximum and minimum areas. However, the estimated surface for the shear strength of the weak layer differed slightly from the slab properties. This finding reinforces the above results, indicating that the spatial pattern of the weak layer differed from the slab properties in our dataset. Estimation errors for critical crack length ranged 0.11 to 0.60 m, except for 1.2 m for AR22-PP. The RMSE and MAE for the skier propagation index ranged from 0.27 to 4, showing significant variability and rela-

Table 3 – Summary of the spatial models, model selections, and performance metrics for the snow properties. The performance metrics are the following: R^2, the percentage of deviance % dev, scale, the cross-validated Root-mean-squared-error CV RMSE, and the cross-validated mean-absolute-error CV MAE. The symbols next to the covariates refer to the significance levels of the p-value: > 0.1 ".", < 0.05 "*", < 0.01 "**", < 0.001 "***".

Site	Snow prop.	Covariates	R^2	% dev	scale	CV RMSE	CV MAE
JBC22-SH	D	TPI2550* + VRM25 + VRM5* + H_s* + Convex. + Dist-cano* + S_x*	0.35	42.9	9.57e-5	0.01	0.01
JBC22-SH	ρ_{slab}	Slope** + VRM15*** + H_s* + Convex*** + Dist-cano*	0.57	64.1	12.22	7.91	4.78
JBC22-SH	τ_p	(x+y)* + Slope* + TPI515* + VRM15** + VRM5* + Convex* + Cano.	0.50	66.2	3762.3	66.29	51.70
JBC22-PP	D	VRM5. + Cano*	0.17	22.2	0.0001	0.01	0.01
JBC22-PP	ρ_{slab}	Slope** + TPI515** + TPI2550*** + VRM25** + VRM15** + VRM5* + H_s. + S_x.	0.64	69.6	15.13	6.32	5.00v
JBC22-PP	τ_p	(x+y)*** + TPI2550*** + VRM25** + VRM15 + VRM5*** + Dist-cano** + S_x*	0.76	80.4	864.78	41.32	30.79
RH22-PP	D	(x+y)*** + Slope* + TPI515*** + TPI2550* + Cano** + Dist-cano** + S_x**	0.54	60	0.0002	0.03	0.02
RH22-PP	ρ_{slab}	(x+y)** + Slope. + TPI515. + VRM15** + Convex*** + Cano*	0.32	38.2	64.99	11.39	8.51
RH22-PP	τ_p	(x+y)** + TPI2550*** + VRM25* + VRM5** + Rad* + Cano**	0.42	48.3	10463	128.37	99.70
AR22-PP	D	(x+y). + VRM15* + VRM5. + Cano.	0.28	36.2	0.006	0.12	0.10
AR22-PP	ρ_{slab}	(x+y)** + TPI2550. + H_s. + Convex**	0.41	46.8	216.77	21.78	21.80
AR22-PP	τ_p	(x+y)*** + Slope* + TPI2550*** + VRM5* + Convex*** + Dist-cano*	0.72	76.7	2.157e5	752.70	578.88

Table 4 – Summary of the spatial models, model selection and performance metrics for the stability metrics. The performance metrics are the following: R^2, the percentage of deviance % dev, scale, the cross-validated Root-mean-squared-error CV RMSE, and the cross-validated mean-absolute-error CV MAE. The symbols next to the covariates refer to the significance levels of the p-value: > 0.1 ".", < 0.05 "*", < 0.01 "**", < 0.001 "***".

Site	Stab. metrics	Covariates	R^2	% dev	scale	CV RMSE	CV MAE
JBC22-SH	l_{sk}	(x+y)* + Slope** + VRM15*** + VRM5. + Convex.	0.58	64.8	0.06	0.48	0.22
JBC22-SH	A_c	Slope*** + TPI515** + TPI2550* + VRM15*** + VRM** + H_s***	0.60	65.9	0.06	0.20	0.14
JBC22-SH	SPI	Slope** + VRM15* + VRM15** + H_s*	0.35	40.3	6.66	2.5	1.89
JBC22-PP	l_{sk}	(x+y)*** + TPI2550** + VRM25** + VRM5** + S_x*	0.60	65.1	0.006	0.10	0.07
JBC22-PP	A_c	(x+y)* + TPI515*** + VRM5*** + H_s. + Rad** + S_x*	0.74	77.7	0.02	0.15	0.11
JBC22-PP	SPI	(x+y)** + TPI515*** + VRM5*** + Rad** + S_x*	0.84	87	0.20	0.36	0.27
RH22-PP	l_{sk}	(x+y)*** + TPI2550** + VRM25** + VRM15* + VRM5* + Rad* + Cano*	0.51	57.1	0.004	0.11	0.08
RH22-PP	A_c	VRM25** + VRM5**	0.25	28.7	0.39	0.60	0.47
RH22-PP	SPI	(x+y)*** + VRM25*** + Rad. + Convex**	0.43	48.5	0.61	1.23	0.85
AR22-PP	l_{sk}	(x+y)** + VRM25*	0.22	27.5	3.2	2.97	1.85
AR22-PP	A_c	TPI2550*** + VRM15* + Convex* + Cano. + S_x.	0.65	69.1	0.61	1.26	1.01
AR22-PP	SPI	TPI2550*** + Convex**	0.66	68.7	5.14	4.29	3.31

tively high values for an index. The estimation errors for the stability metrics were notably high, demonstrating that the model estimations were not reliable compared to the snow mechanical properties. However, Figure 14 suggests that some outliers might have contributed to overestimating the RSME, particularly with low values of l_{sk} and high SPI values (SPI $\approx$ 10). The spatial patterns of the stability metrics revealed two major weak spots represented by two clusters of low SPI values near zero, located on the north side (right) and northwest (upper-middle). These weak spots corresponded to areas with lower shear strength values and slightly thicker and higher-density slabs.

There are no clear covariates selected by the model for every site, snow properties, or stability metrics. However, some covariates were selected more frequently by the spatial models than others. The most frequently used covariates by the models, for both snow properties and stability metrics, were multiscale TPI and VRM, but their usage varied depending on the scale (Figure 15). Spatial models for the shear strength of the weak layer appeared to select mainly TPI2550 and VRM5, whereas for slab density, VRM15 and convexity were chosen predominantly. Canopy height was selected in the snow properties models, but rarely in the stability metrics models. The easting and northing coordinates (xy) were widely used in the models, indicating the presence of spatially autocorrelated residuals. Surprisingly, snow depth was not used as frequently as other covariates. Convexity was selected numerous times, especially for the slab density, but almost never for the slab thickness. Overall, these results indicate that there are no universal covariates or specific covariates for snow properties or stability metrics that could be extrapolated to other sites. The selection of covariates by the spatial models was site-specific and also specific to different snow properties. The spatial models presented using microtopography indicators were fairly reliable for estimating absolute values of snow properties and not reliable for the stability metrics, but rather for capturing relative spatial variability.

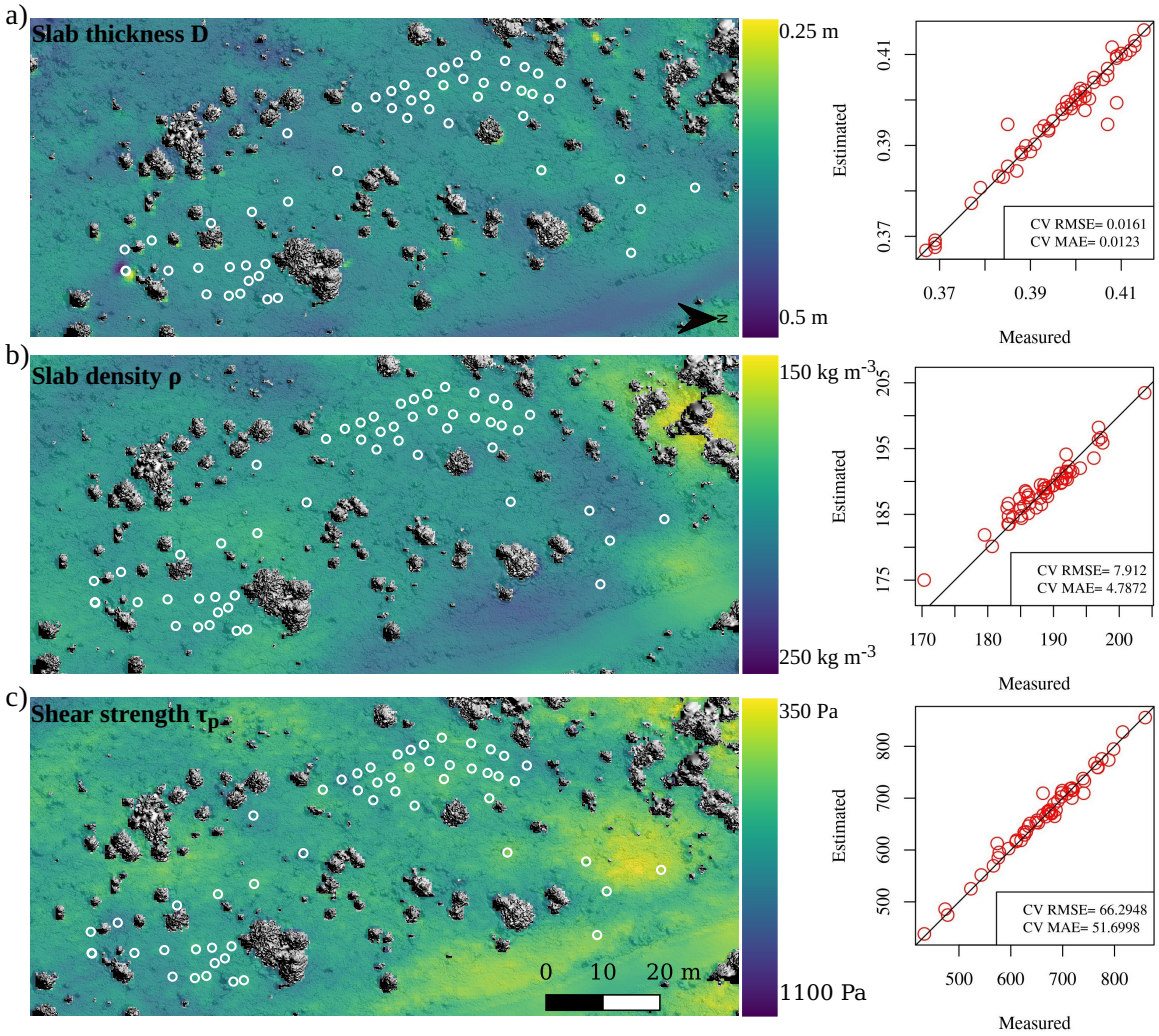

Figure 13 – Spatial estimation for the snow mechanical properties a) slab thickness D, b) slab density ρ, c) shear strength τ_p at the Jim Bay Corner on 19 January 2022 (surface hoar layer - 1mm). The cross-validated root mean squared error RMSE and the mean absolute error MAE are shown next to the map of each property. The gray shading on the background map represents a canopy shading only for the visualization of trees.

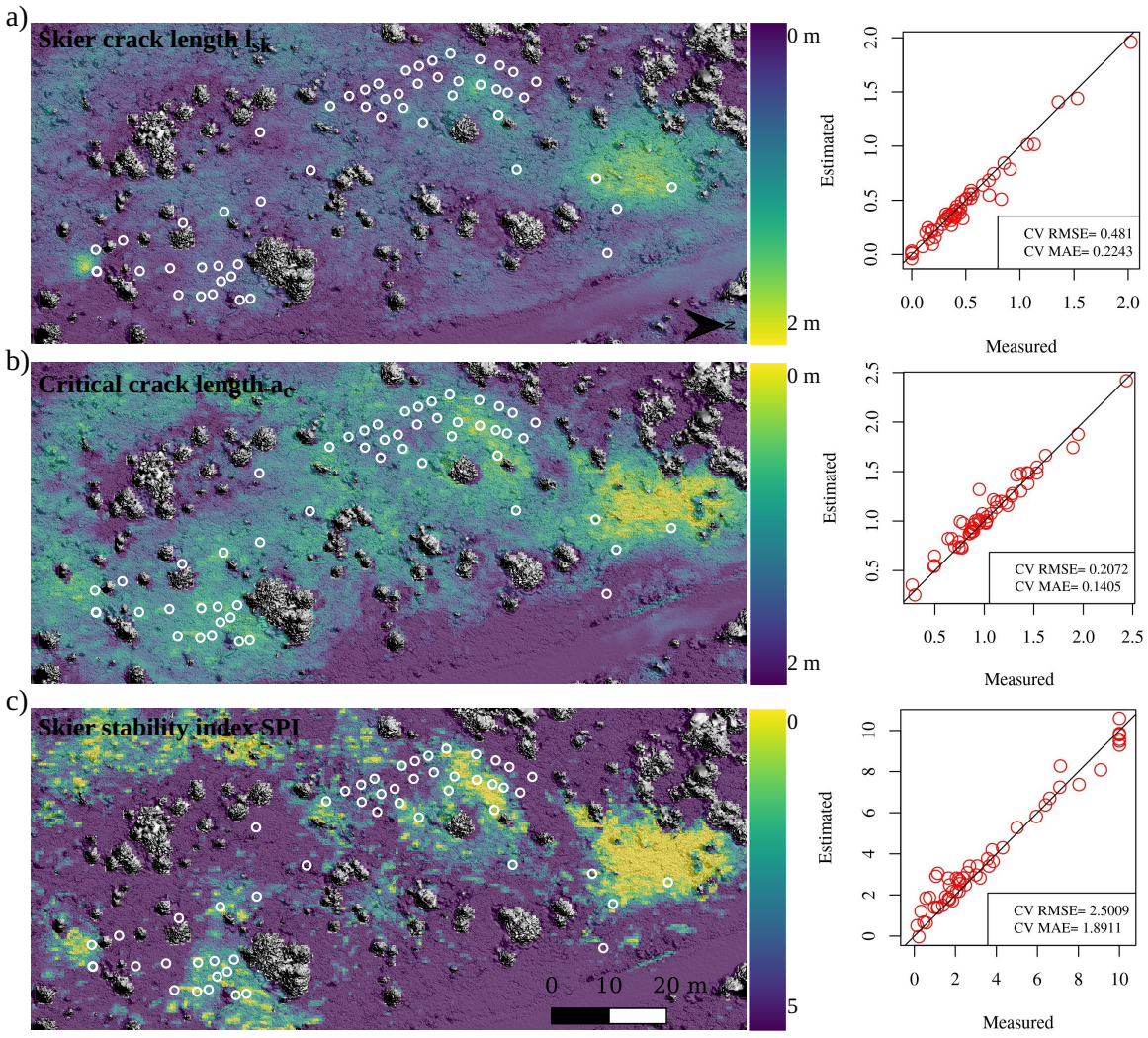

Figure 14 – Spatial estimation for the stability metrics a) skier crack length l_{sk}, b) critical crack length a_c, and c) Skier propagation index SPI at the Jim Bay Corner on 19 January 2022 (surface hoar layer - 1mm). Cross-validated root mean squared error RMSE and mean absolute error MAE are shown next to the map of each metric. The grey shading on the background map represents a canopy shading only for the visualization of trees.

1.6 Discussion

1.6.1 Snow mechanical parametrization

Our study aligns with the well-known relationship between slab thickness and slab density, attributed to snow settlement. The comparison of spatial patterns between surveys

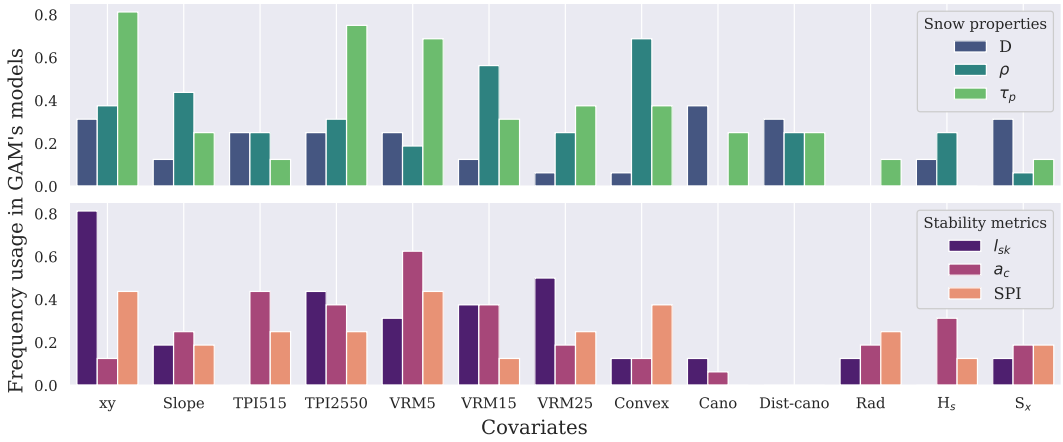

Figure 15 – The frequency usage of covariates in the GAM spatial models, the frequency is weighted with the significance levels of the p-value.

indicated that these two properties exhibited similar trends in their variogram, the fractal dimension, and their covariates used for spatial modeling. For further research, the empirical power law fit $\rho \sim 100 + 135D^{0.4}$ suggested by McClung (2009) provides a simple approach to obtain average values that represent the interaction between these two properties for mechanical simulation (e.g. Gaume and Reuter, 2017). The power law fitted to our SMP-derived data set appears to yield better average values for denser slabs in wind-exposed areas. However, it is important to note that these power laws fitted poorly with our dataset, indicating that significant variability remains. Nevertheless, these power laws could be used in a snow mechanical model to generate a slab density variation according to the spatial pattern of the slab thickness. Until now in snow mechanical modeling research, the spatial variation of snow properties was limited to the weak layer. Our study shows a distinction between the spatial variation of the slab properties and the weak layer, already observed by Kronholm (2004) and Bellaire and Schweizer (2011). We propose accounting for both slab properties variation and weak layer variation since spatial patterns can differ between them.

Weak layer variations exhibited longer correlation lengths (smoother spatial pattern) than slab variations, and the increase in shear strength did not necessarily match the increase in the slab thickness. In general, shear strength should increase with slab thickness due to

the slab load, but some variation was still present in our dataset (Figure 9). The interaction between slab thickness and shear strength can be described with a power law $\tau_p \sim c + 1370D^{1.3}$ (Bažant *et al.*, 2003), reported according to the Mohr-Coulomb relation with initial cohesion c (300 Pa in Figure 9) (Gaume *et al.*, 2014). This power law represented well the average values of the survey from Mount Fidelity, but our fitted power law could also be used for thicker (denser) slabs in wind-exposed areas. However, the four power laws tested did not adequately capture the variability in values for a specific spatial survey. The constant parameter must be adjusted for each spatial survey to fit the values. Overall, these power laws should be used with caution to estimate the average snow values (strength and density) if only the slab thickness is available.

Gaume *et al.* (2013) proposed a method to generate a weak layer with spatial heterogeneity. The method generates a random field with a specified mean, variance, and correlation length for the cohesion of the weak layer, where the shear strength of the weak layer is defined by a Mohr-Coulomb relation. The friction term of the Mohr-Coulomb relation, which incorporates the slab load, was added to the cohesion to obtain the shear strength. Although their friction term was constant due to a constant slab thickness, the method can be easily adapted to accommodate a variable friction term, reflecting a variation in slab thickness. This adaptation would enable the specification of two distinct random fields for the properties of the slab and the weak layer while ensuring consistency with load of the slab. This method still requires input values for mean, variance, and correlation length. The empirical power law can estimate mean values, but according to our dataset, the variance is not well represented (Figure 9). Future work should explore the possibility to estimate variance and correlation length of snow properties using the covariance of microtopography combined with distributed snow cover modeling. Such approaches could contribute to more realistic simulations in avalanche modeling, enhancing forecasting capabilities for both the probability of skier triggering and the size of avalanche releases.

1.6.2 Spatial modeling

This study gathers a unique dataset characterizing the spatial variation of snow mechanical properties and stability metrics at four different study sites. The comparison of variograms and fractal dimensions highlights differences in scale between slab properties and, on the other hand, weak layer properties and stability metrics (smoother patterns). Spatial GAM models were used to estimate with fair accuracy the snow mechanical properties using microtopography. However, the spatial modeling of the stability metrics was poor and not reliable. Additionally, a portion of spatial variances remained unexplained by the models, potentially due to non-spatial variances, such as instrument error or our processing data strategy. This strategy included a visual interpretation of the layer in the SMP resistance profile, as misclassification or misidentification of the weak layer boundaries can impact the result. Nevertheless, the modification of using the parameterization ω proposed by Richter *et al.* (2019) instead of the weak layer thickness for the computation of the critical crack length makes the method less dependent on weak layer thickness, enhancing its robustness. While the cross-validated RMSE for snow mechanical properties suggests sufficient precision, the high RMSE for stability metrics indicates that the spatial modeling of these metrics is not reliable (Table 3). Future work could use spatial estimations of the snow mechanical properties to compute the stability metrics from the spatial field of snow properties.

The cross-validation procedure was performed by randomly selecting 10 subsets. Future work should consider the correlation length during the random selection of subsets in cross-validation procedures to ensure complete independence between subsets. This could improve the reliability of RMSE and MAE estimations. However, our 10-fold cross-validation (repeated 10 times) still provides a reliable estimation of the performance of our models.

1.6.3 Microtopographic covariates

This study aimed to use microtopographic covariates for spatial estimations of snow spatial variability and stability. Our GAM spatial modeling did not reveal a universal covariate that could spatially estimate both snow mechanical properties or stability metrics. The study of Reuter *et al.* (2016), based on larger-scale terrain-based covariates, did not find a consistent covariate in all surveys to estimate instability at the basin scale. They reported that the slope aspect was selected as a estimator by the model in all of their surveys, but each survey used a different combination of covariates. In the present study, the selection of covariates was specific to each survey with no clear trend or takeaway regarding the choice of covariates. Notably, snow depth was not a reliable spatial estimator of snow mechanical properties and stability metrics, a finding consistent with the study by Reuter *et al.* (2016). The limited selection of snow depth as an estimator in our study might be attributed to the homogeneity of the dataset regarding snow depth or the weak layer's spatial variation being unrelated to the snow accumulation process. It is also noteworthy that, despite AR22-PP being a wind-exposed site, the GAM model did not select the Winstral index S_x as a predictor. This could be related to the research distance in S_x being too large (100 m), and adjusting the scale of this indicator, similar to TPI and VRM, could reveal S_x as a significant covariate, especially at the wind-exposed site (AR22-PP).

Unfortunately, no link could be made between our only persistent weak layer survey consisting of surface hoar crystals (JBC22-SH) and the remaining non-persistent weak layer surveys. A bigger dataset is needed to demonstrate clear differences between persistent vs. non-persistent weak layers, as well as between alpine vs. forested areas. The covariates TPI and VRM emerged as the most significant covariates for estimating snow properties, this was also observed by previous studies using spatial models (random forest) for snow depth estimation (Meloche *et al.*, 2022; Revuelto *et al.*, 2020). The optimal scale or window size for TPI and VRM varied depending on the study site, snow properties and stability metrics. Future work with a more extensive dataset should investigate whether the optimal scale is

linked to the specific scale of terrain features at each site, the scale of the meteorological process affecting the slab and the weak layer, or a combination of both factors.

The transferability of our results to different sites is not feasible. The selection of covariates by the model was specific to each site, snow properties and stability metrics. As demonstrated by Reuter *et al.* (2016), the interaction between meteorological processes and terrain leads to distinct spatial variations in snow properties across different surveys. These micrometeorological processes vary between sites and differences emerge not only between slab deposition patterns, but crucially, between different types of weak layer. More spatial snow surveys are needed to gather a robust dataset to highlight trends in spatial patterns between different types of weak layers, slab deposition, microtopographic, and microclimatic contexts. To obtain a more robust dataset, future research should aim for an equivalent or higher sampling density and extent presented in this study (60 and more SMP profiles covering 80 m extent). Lowering the sampling density and extent could compromise the estimation of the experimental variogram and the spatial modeling. An alternative approach to sampling with fewer SMP measurements could be to incorporate distributed 3D snow cover modeling tools like ALPINE3D. This avenue was explored by Reuter *et al.* (2016), but acknowledged the need to improve performance in distributed snow cover modeling. Implementing 3D snow cover modeling has the potential to capture a portion of these site-specific micrometeorological processes without requiring an extensive spatial survey of SMP measurements.

1.7 Conclusion

The study provides insights into the spatial variability of snow mechanical properties and stability metrics. First, we show that in our dataset, the slab properties exhibit spatial patterns that were different from the weak layer spatial patterns. In fact, the slab properties, both the slab thickness and density, had smaller correlation lengths in their variograms than the weak layer strength. The slab properties had higher fractal dimensions than the weak

layer strength, which demonstrates a more ”rough” spatial surface. Secondly, spatial modeling using microtopography variables allows for the estimation of snow mechanical properties with reasonable accuracy, although the reliability of stability metric estimations was poor and not reliable. We also show the utility of using microtopography to estimate snow spatial variability, but the selection of the indicators was specific to each study site and snow properties. The spatial models did not predominantly select a microtopographic indicator, indicating that there is no possible extrapolation to other sites or advice to backcountry recreationists. Future research could explore the capability of multiscale microtopographic indicators, like the topographic position index (TPI) and vector ruggedness measure (VRM), to estimate spatial patterns of snow mechanical properties with 3D snow cover modeling. This may contribute to the development of predictive methods for operational avalanche forecasting services, potentially estimating avalanche release sizes through snow cover modeling and mechanical models. Additional work is needed to gather a robust dataset regarding the spatial pattern of snow mechanical properties in order to elucidate trends between different types of weak layers and terrain features.

1.8 Acknowledgements

This project was funded by the Search and Rescue New Initiatives Fund from Public Safety Canada (SAR-NIF), the Natural Sciences and Engineering Research Council of Canada (NSERC), the Quebec Research Funds - Nature and Technologies (FRQNT), and the Canada Foundation for Innovation (CFI) for funding the Station d’études montagnardes des Chic-Chocs (SEM). The authors would like to thank Jeff Goodrich and the Mount Revelstoke and Glacier National Parks staff for their support. This research was also possible with the help of Claude Isabel and the Gaspésie National Park (SEPAQ), and also with the help of Dominic Boucher and Avalanche Québec staff. The authors would also like to thank Jean-Benoît Madore, Julien Meloche, Antoine Rolland, Alex Blanchette, Jacob Laliberté and William Durand for their help on the field. We want to thank the two anonymous reviewers

for their helpful and constructive comments, which significantly improve the quality of our manuscript. Lastly, we want to thank Jürg Schweizer for his useful comments to improve the presentation quality of this manuscript.

ARTICLE 2

L'INFLUENCE DE LA VARIABILITÉ SPATIALE DE L'ÉPAISSEUR DE LA PLAQUE SUR LA PROBABILITÉ DE DÉCLENCHEMENT PAR SKIEUR ET LA TAILLE DE L'AVALANCHE

2.1 Résumé en français du deuxième article

La variabilité spatiale des propriétés de la couche de neige ajoute de l'incertitude dans l'évaluation du danger d'avalanche. La variabilité de l'épaisseur du manteau neigeux, et par conséquent, l'épaisseur de la plaque susceptible de créer une avalanche, est significative à l'échelle de la pente (10-100 m). Ce prochain article propose une approche statistico-mécanique pour étudier comment la variation spatiale de l'épaisseur de la plaque influence la probabilité de déclenchement par un skieur et la taille possible de l'avalanche. Tout d'abord, nous générons plusieurs cartes d'épaisseur de plaque sur une pente fictive basée à partir d'un algorithme *Gaussian Random Field* (GRF), en spécifiant la moyenne, la variance et la longueur de corrélation. Pour chaque GRF, nous dérivons analytiquement l'indice de propagation du skieur (SPI). Ensuite, nous simulons plusieurs traces de skieurs et calculons la probabilité en fonction du nombre de fois où la trajectoire d'un skieur franchit une zone où le SPI est inférieur à 1. Enfin, nous utilisons une méthode de calcul numérique *Depth-Averaged Material-Point Method DAMPM* pour évaluer la taille possible de l'avalanche pour différentes variations de l'épaisseur de la plaque. Les résultats de cette analyse montrent que de grandes longueurs de corrélation et de petites variances entraînent une probabilité plus faible de déclenchement par un skieur, car cela réduit la taille et le nombre de zones avec une faible épaisseur de plaque. Ensuite, nous montrons l'effet du style de ski et de la taille du groupe de skieurs sur la probabilité de déclenchement par un skieur. La variabilité spatiale affecte également la taille possible de l'avalanche en ajoutant des fluctuations de contrainte

provoquant parfois une longueur en tension courte ou longue. En conclusion, nous quantifions avec nos modèles, la relation classique entre la probabilité de déclenchement par skieur et la conséquence d'une avalanche, ainsi que l'effet de la variabilité spatiale de l'épaisseur de la plaque.

Ce deuxième article, intitulé "*Influence of slab depth spatial variability on skier-triggering probability and avalanche size*", fut corédigé par moi-même ainsi que par mon collègue Louis Guillet de Université Grenoble Alpes, mon directeur Francis Gauthier, mon codirecteur Alexandre Langlois de l'Université de Sherbrooke, ainsi que Johan Gaume de l'École polytechnique fédérale de Zürich. Cet article a été réalisé dans le cadre d'une échange doctorale de 8 mois à l'École polytechnique fédérale de Lausanne avec le professeur Johan Gaume et Louis Guillet. Il fut accepté pour publication dans sa version finale en Janvier 2024 par les éditeurs de la revue *Annals of Glaciology*. Ma contribution en tant que premier auteur a été de conceptalisé la recherche en collaboration avec professeur Johan Gaume et de mon collègue Louis Guillet. Louis Guillet a développé la méthode numérique *Depth-averaged Material-Point-Method* avec l'aide de Johan Gaume. Ce dernier a émis de nombreuses recommandations durant l'ensemble du travail qui ont grandement amélioré la pertinence et la qualité de présentation de l'article. Francis Gauthier et Alexandre ont contribué significativement au développement de la recherche avec de nombreux conseils. Ils ont également contribué à la rédaction et la correction de l'article. Une version abrégée de cet article a été présentée à la conférence *International Snow Science Workshop ISSW* à Bend, en Oregon (États-Unis) à l'automne 2023.

2.2 Influence of slab depth spatial variability on skier-triggering probability and avalanche size

2.3 Introduction

2.3.1 Avalanche Hazard

Snow avalanches represent a natural hazard for infrastructure and backcountry recreationists across mountainous areas all across the world (Stethem *et al.*, 2003). Snow avalanches can be divided into different types from wet or dry avalanches and also loose-snow or slab avalanches (Schweizer *et al.*, 2003). However, dry-snow slab avalanches are the most destructive type and also very difficult to predict (Techel *et al.*, 2016). Such an avalanche releases from the failure of a porous weak layer buried below a cohesive snow slab. The initiation of the failure can be induced by a skier, new snow or explosives. If the size of the failed zone in the weak layer - or crack - exceeds a critical size, the crack may self-propagate across the slope possibly leading to the release and sliding of the snow slab (Schweizer *et al.*, 2016). Statham *et al.* (2018) proposed a conceptual model to better predict the avalanche hazard for practitioners and backcountry recreationists. This conceptual model consists of two main components: the likelihood of an avalanche and the avalanche release size. The combination of these two components gives the avalanche hazard in North America (Statham *et al.*, 2018). The terminology is slightly different in Europe which is based on three components: the probability of avalanche release, the frequency of these triggering spots and the avalanche size (Techel *et al.*, 2020). Practitioners and forecasters use mostly snow stability tests to gain information on the probability of triggering an avalanche, both by a skier or naturally. Repeated tests at numerous locations help them to gain information on the spatial distribution of the instability (Schweizer *et al.*, 2008a). However, the sparse and punctual nature of available observations on snowpack properties makes the forecasting of dry snow slab avalanches difficult (Hägeli and McClung, 2004). The second main component of the avalanche hazard is the

avalanche release size. Forecasters try to estimate the possible avalanche size by estimating the slab depth and the slab-weak layer propagation propensity. Studies have shown that these properties are highly variable in space (Schweizer *et al.*, 2008a), which makes it even more difficult to predict. The snow spatial variability at different scales also adds complexity to this difficult task by adding uncertainty on whether the properties measured on the field are representatives or not of the slab and weak layer system (Schweizer *et al.*, 2008a). At a smaller scale, the decision-making in avalanche terrain such as the task of up-hill and downhill route finding is very complex partly due to the spatial variability of snow.

2.3.2 Spatial variability of snow

The subject of the spatial variation of snow mechanical properties is nothing new in the science community. Conway and Abrahamson (1984) has made several measurements of a weak layer shear strength along an avalanche fracture line. They highlight these so-called deficit zones where the weak layer shear strength was significantly lower than surrounding areas along the fracture line. The idea of weak zones or weak spots initiated numerous studies over the last two decades (Schweizer *et al.*, 2008a). New instruments like the high-resolution snow penetrometer called SnowMicroPen (SMP) can measure with great accuracy the snow mechanical properties of both the slab and the weak layer (Proksch *et al.*, 2015; Löwe and van Herwijnen, 2012; Johnson and Schneebeli, 1999; Reuter *et al.*, 2019). The SMP enabled fast sampling of the snow mechanical properties over several locations on an avalanche-prone slope (Bellaire and Schweizer, 2011; Feick *et al.*, 2007; Lutz *et al.*, 2007; Landry *et al.*, 2004; Kronholm, 2004; Lutz and Birkeland, 2011; Reuter *et al.*, 2016). These studies focused mainly on the weak layer properties, thickness and strength, and they used the variogram analysis to estimate the spatial pattern of the weak layer mechanical properties. They reported correlation distances ranging from 1 to 15 m with a spatial sampling extent of around 20 and 40 m. The correlation distances were nearly half of the extent and this could bias the estimation of the correlation length (Skøien and Blöschl, 2006; Kronholm and Birkeland,

2007). Reuter *et al.* (2016) used the same sampling density but with a spatial extent of nearly 500 m, and reported correlation distances from 5 to 25 m with one exception of 68 m.

These studies measured and explained the spatial variability of snow mechanical properties, but did not explain the effect of this variability on slope stability. Kronholm and Schweizer (2003) proposed a conceptual model to explain the effect of the spatial variation of the stability on the overall slope stability. Short-range variation could have a stabilizing effect on the snowpack and the long-range variation could have a so-called "knock-down effect" on the slope stability, but further investigation through mechanical models was needed to test this conceptual model. Several studies simulated artificial spatial patterns of the weak layer into mechanical models in order to explain the effect of the spatial variability of the weak layer on the overall slope stability (Gaume *et al.*, 2014, 2013; Kronholm *et al.*, 2004; Schweizer *et al.*, 2008a; Fyffe and Zaiser, 2004). First, some studies used cellular automata models and showed the effect of the variance shear strength on the slope stability (Fyffe and Zaiser, 2004; Kronholm and Birkeland, 2005; Faillettaz *et al.*, 2004). High shear strength variances create more deficit zones and cause easier overall failure of the slope even with strong zones. However, these models only account for the state of the neighbor cells and large-scale elastic redistribution could not be taken into account, therefore the link with the correlation length could not be explored. Finite-element method (FEM) can handle large-scale elastic redistribution and was used in several studies to explain the influence of the correlation length over the slope stability. Gaume *et al.* (2013) explored how the stress redistribution induced by the elasticity of the slab could smooth the heterogeneity of the weak layer. They showed, in particular, that if the correlation length is smaller than the characteristic elastic length of the system, it behaves as in a homogeneous case. When the correlation length is larger than this elastic length, the smoothing does not take place and the system is more likely to fail even for large slab depth which illustrated the so-called knock-down effect (Gaume *et al.*, 2013, 2014). Gaume *et al.* (2015a) use the same method to estimate the propensity for tensile failure in the slab in order to relate to the avalanche release size. Weak layer heterogeneity increases slab tensile failure propensity for soft and shallow slabs, thus

potentially smaller avalanches. On the other hard and deep slabs were hardly influenced by weak layer heterogeneity which led to wide-spread crack propagation.

These FEM studies focused exclusively on the spatial variation of the weak layer cohesion and its influence on natural avalanche release. It has been demonstrated numerous times, through survey and modeling, that snow depth is highly variable in mountainous areas (e.g. Deems *et al.*, 2006; Winstral *et al.*, 2002; Mott *et al.*, 2011; Grünewald *et al.*, 2013; Schirmer *et al.*, 2011; Hubbard *et al.*, 2018), especially in avalanche start zones (Miller *et al.*, 2022). The slab depth spatial variability should be related to the spatial variation of snow depth. Therefore, the spatial variation of the slab depth should affect the skier-triggering probability over an entire slope. For homogeneous cases, the influence of slab depth on skier-triggering was analyzed based on stress over strength approaches (Föhn, 1987; Monti *et al.*, 2016; Habermann *et al.*, 2008) but also to address crack propagation propensity (Heierli *et al.*, 2008; Gaume *et al.*, 2017). To the best of our knowledge, there is no study on the effect of slab depth spatial variation on the probability of skier-triggering and crack propagation. Slab depth variability should also affect the avalanche possible size. Slab properties, mainly slab depth and density, are one of the main drivers for dynamic crack propagation (McClung, 1981; Heierli *et al.*, 2008; Gaume *et al.*, 2017). The spatial variation of the slab-weak layer system should affect the stress in the slab and might promote crack arrest caused by slab tensile failure. There is a need for further investigation on that matter in order to provide estimates of the avalanche release size which is crucial information for avalanche forecasting and risk management.

Several tools have been used to understand dynamic crack propagation. Previous studies on the influence of spatial variability of snow on the release and the avalanche size used mainly mesh-based approaches which can handle large deformations and fracture propagation at the (significant) cost of re-meshing and mesh refinement techniques. Some researchers used the discrete element method to model snow but are limited to small computational domains from the microstructure scale (Mede *et al.*, 2020; Hagenmuller *et al.*, 2015) to a

few meters scale (Gaume *et al.*, 2017; Bobillier *et al.*, 2021). More recently, the Material Point Method (MPM), a hybrid Eulerian-Lagrangian technique showed promise in simulating solid-fluid transitions and crack propagation in geomaterials (Sulsky *et al.*, 1994). Gaume *et al.* (2019) propose an elastoplastic MPM with a new snow constitutive model to simulate the mechanical behavior of snow slabs and weak snow layers. With this model, they can simulate in a unified way, numerous important mechanical processes in a snow slab avalanche, from the weak layer failure initiation, dynamic crack propagation, slab tensile fracture, and, finally the release and the flow of the slab down the slope. Trottet *et al.* (2022) used this method and full-scale measurements to reveal a transition between anticrack propagation (closing crack/mode -I) and so-called "supershear" propagation in which the fracture occurs in shear (mode II) at a speed larger than the shear wave speed (of the slab). They report that this transition requires a slope angle larger than the snow friction angle ($\approx 27°$) and a propagation distance larger than typically 3-5 m. This suggests that a pure shear interface model could be sufficient to simulate large avalanche releases on an inclined slope. This finding, together with the large computational cost of 3D MPM simulations motivated us to use the depth-averaged MPM (DAMPM) recently proposed and validated by Guillet *et al.* (2023). DAMPM enables a fast computation time over large domains, allowing us to produce a vast number of simulations to better understand the effect of the slab depth variation on the avalanche release size.

Understanding how the spatial variation of slab depth influences the probability of skier-triggering and the avalanche release size is of great importance. This could lead to an improvement in snow avalanche forecasting and decision-making in avalanche terrain for backcountry recreationists. To better understand this issue, we propose a combined mechanical-statistical approach to study how spatial variation of slab depth affects the skier-triggering probability and possible avalanche release size. First, a sensitivity analysis is made for the skier-triggering probability in relation to the spatial variation of the slab depth. Secondly, we use our approach to test the effect of skiing style and downhill strategy on skier-triggering probability. Lastly, DAMPM simulations allowed us to investigate the relation

between slab depth variations and the avalanche release size, by analyzing the propagation distance leading to the first tensile fracture in the slab.

2.4 Methods

2.4.1 Spatial variability of slab depth

Gaussian random fields (GRF) will be used to generate artificial 2D surfaces as input into our numerical mechanical models. Each point of the surface in space (x, y) can be defined as a random variable, so the collection of random variables is called a random field defined by:

$$D(x, y) \in \overline{D} \cdot C \tag{2.1}$$

where $D(x, y)$ is the slab depth random field, $\overline{D}$ is the mean slab depth and cov is the Gaussian covariance model defined by the formulation in *gstools v1.3* documentation (Müller *et al.*, 2022):

$$cov(d) = S_D^2 \left[1 - exp\left(\frac{d}{\epsilon} \right)^2 \right] \tag{2.2}$$

where d is the distance between the observations, S_D^2 is the slab depth variance and ϵ is the correlation length of the slab depth variation. We used a Gaussian covariance model without a nugget. For each GRF, we can specify the mean and the covariance function, the last one is defined by a variance and a correlation length. A sensitivity analysis is presented on these three parameters of the slab depth spatial variation for both the skier-triggering probability and avalanche release size. We test the mean slab depth from 0.5 m to 1 m with a 0.1 m increment. Several studies have shown that snow mechanical properties can be approximated by a Spherical and Gaussian covariance function with correlation lengths ranging mostly from 5 to 20 m (Bellaire and Schweizer, 2011; Feick *et al.*, 2007; Lutz *et al.*, 2007; Landry *et al.*, 2004; Kronholm and Schweizer, 2003; Lutz and Birkeland, 2011; Reuter *et al.*, 2016) and sometimes 50 m (Reuter *et al.*, 2016). Based on these studies, we chose

to test correlation length from 5 m to 40 m with an increment of 5 m. The idea is to tend toward a very smooth random field close to a homogeneous case. We took the same approach with the variance, from 0 to 0.025 m^2 which represents approximately 0.3 m from the mean slab depth to maximum and minimum values. The selected variance values were based on field measurements done by **?**. Gaussian random fields were generated using the *gstools v1.3* package in Python (Müller *et al.*, 2022).

2.4.2 Skier-triggering probability

One of the specific objectives of this study is to evaluate the skier-triggering probability as a function of slab depth variations. The snow properties were selected to represent a meta-stable slab and weak-layer system where the natural release is not possible but only the skier-triggering. Different snow mechanical properties can be related to each other (Jamieson and Johnston, 1990; Scapozza *et al.*, 2004; Sigrist, 2006). In general, it has been demonstrated that the increase in slab depth will also increase the snow density, elastic modulus, and shear strength of the weak layer. We computed realistic snow mechanical values based on empirical power-law functions obtained based on literature data. First, the snow density ρ is related to the mean slab depth $\bar{D}$ according to Equation 6 in McClung (2009):

$$\rho = 100 + 135\bar{D}^{0.4} \tag{2.3}$$

Then, we computed the elastic modulus E based on the snow density ρ according to Sigrist (2006):

$$E = 9.68 \times 10^8 \left(\frac{\rho}{\rho_{ice}}\right)^{2.94} \tag{2.4}$$

where $\rho_{ice} = 917\ \mathrm{kg\ m^{-3}}$. Note that, contrary to the slab depth, the density and elastic modulus of the slab does not spatially vary in our simulations but are related to the mean slab depth. Finally, the shear strength of the weak layer τ_p was computed according to the following

power-law relationship from Bažant *et al.* (2003) adapted by Gaume *et al.* (2014):

$$\tau_p = c + 1370D^{1.3} \tag{2.5}$$

where c is the cohesion set to 300 Pa. This allows us to account for the local friction effect where the slab depth is locally increasing.

2.4.3 Stability metrics

We choose to assess the skier stability based on the skier propagation index (SPI) proposed by Gaume and Reuter (2017). The index consists of the ratio between two lengths, namely the critical crack length a_c and the skier crack length l_{sk} (Gaume and Reuter, 2017). The skier crack length is computed by solving the equation: $\tau + \Delta\tau = \tau_p$, where $\tau = \rho g D \sin\psi$ is the shear stress due to the slab weight on an inclined slope ψ and g is the gravitational acceleration constant. The additional stress due to the skier standing on the snow is defined by (Föhn, 1987; Monti *et al.*, 2016):

$$\Delta\tau = \frac{2R\cos\alpha\sin^2\alpha\sin(\alpha+\psi)}{\pi D} \tag{2.6}$$

where R is the skier load set to 780 N and ψ is the slope angle set to 35°. We find the two roots of the equation given two angles α_1 and α_2, where total shear stress is equal to the shear strength of the weak layer. We used the two angles α_1 and α_2 to find the skier crack l_{sk} with the following equation:

$$l_{sk} = D\left[\frac{1}{\tan\alpha_1} - \frac{1}{\tan\alpha_2}\right] \tag{2.7}$$

The critical length a_c is computed using the formulation from Gaume *et al.* (2017):

$$a_c = \Lambda\left[\frac{-\tau + \sqrt{\tau + 2\sigma(\tau_p - \tau)}}{\sigma}\right] \tag{2.8}$$

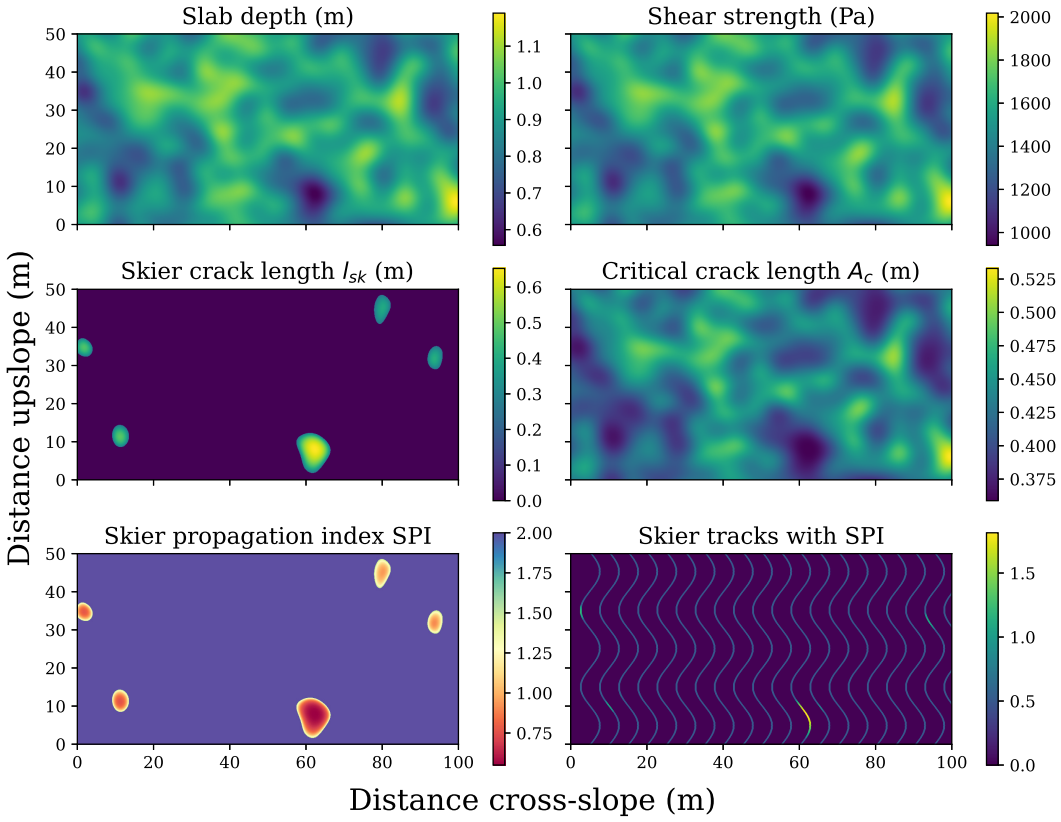

Figure 16 – Example of one realization of a Gaussian Random Field GRF for slab depth D, slab density ρ, skier crack length l_{sk}, critical crack length a_c, skier propagation index SPI and skier tracks with SPI. The slope is reduced to 50 m by 100 m only for visualization purposes.

where $\sigma = \rho g D \cos\psi$ and Λ is a characteristic length of the system defined by:

$$\Lambda = \sqrt{\frac{E' D D_{wl}}{G_{wl}}} \tag{2.9}$$

with $E^{'} = E/(1-\nu^2)$. The weak layer thickness D_{wl} and the shear modulus G_{wl} were set to 0.04 m and 0.2 MPa respectively, ν is the Poisson's ratio set to 0.3. The skier propagation index SPI is thus defined as:

$$SPI = \frac{a_c}{l_{sk}} \tag{2.10}$$

These formulas allow us to generate SPI maps from our corresponding GRF slab depth

and snow properties maps over a 200 m by 100 m fictional slope (Figure 16). For each GRF realization, we simulated sinusoidal ski tracks all over the fictional slope representing a ”modern freeride” skiing trajectory defined by a down-slope turn radius of 10 m and cross-slope amplitude of 5 m (Figure 16). The spacing between the skier was held constant at 5 m with a total of 40 skiers. We recorded a hit if a skier track passed through a zone with SPI below 1. We computed the probability of skier-triggering with the number of skier tracks who recorded a hit compared to all skier tracks on the slope. A convergence of analysis for the total number of skiers on the slope is presented in the appendix (Figure 40).

A secondary objective of this study was to assess the influence of skiing style or skiing trajectory on the skier-triggering probability. Different trajectories were tested on the basis of two ”extreme” trajectories. The first one is to mimic a pure linear trajectory which is defined by the projected weak spot length on the x-axis (cross-slope) compared to the total cross-slope length. This ratio was obtained following these two steps: 1) the presence of weak spots in the up-slope direction is checked for every point following a transect in the cross-slope direction, and 2) a length is obtained with the sum of every presence of weak spot along this transect and then compared to the cross-slope length. The second extreme trajectory mimics a skier who will span the entire slope in a cross-slope direction which would yield a skier-triggering probability of one.

2.4.4 Possible Avalanche size

In order to link the spatial variability of slab depth to the avalanche release size, a method is needed to compute the dynamic crack propagation in a weak snow layer. The finding from Trottet *et al.* (2022) supports the physical assumptions needed for a depth-averaged method that integrates the momentum and mass conservation equation in the z direction. Guillet *et al.* (2023) presents a detailed view of this method and the integration of the governing equation. We will present the key assumptions but please refer to Guillet *et al.* (2023) for an in-depth view of the method. The first key assumption is the classic shallow water

assumption where the vertical length is shorter than the horizontal length, which translates in an avalanche context as $\frac{h_0}{L} \ll 1$ where h_0 is the standard height of the slab and L the characteristic length of the avalanche. The material is assumed incompressible meaning that the density ρ does not depend on position either time and place, and the flow surface is stress-free at the top of the slab where $\sigma|_{h=z} = 0$. Note here, that the method could be easily adapted in compressible form if the ρ needs to be as a function of the particle height and the position. The velocities in the x direction are similar to the ones in the y direction but the velocities in the z direction are small and negligible. The other particularity of the depth-averaged method is the column-shaped particle of height $h = D$ where the integration point of σ_{zz} is $h/2$ (Figure 17), which gives us this depth-averaged equation of mass conservation:

$$\frac{\partial h}{\partial t} + \frac{\partial (h\overline{v}_x)}{\partial x} + \frac{\partial (h\overline{v}_y)}{\partial y} = 0 \tag{2.11}$$

where $\overline{v}_x$ and $\overline{v}_y$ are the depth-averaged velocity field at the integration point of the particle. The last assumption is a plane stress assumption with $\sigma_{zy} = \sigma_{zx} = 0$. Basal forces are applied at the interface between the slab and the weak layer defined by:

$$\tau_{xz} := \sigma_{xz}|_{z=0}, \tau_{yz} := \sigma_{yz}|_{z=0} \tag{2.12}$$

which give also $\sigma_{zz}|_{z=0} = \rho g h$ at the bottom of the slab column and $\overline{\sigma}_{zz} = \frac{1}{2} h \rho g$ at the integration point. This allows us to have the depth-averaged non-conservative form of momentum conservation:

$$\rho h \frac{\overline{d}\overline{v}_x}{\overline{d}t} = \frac{\partial (h\overline{\sigma}_x x)}{\partial x} + \frac{\partial (h\overline{\sigma}_x y)}{\partial y} - \tau_{xz} + g\rho h. \tag{2.13}$$

$$\rho h \frac{\overline{d}\overline{v}_y}{\overline{d}t} = \frac{\partial (h\overline{\sigma}_y y)}{\partial y} + \frac{\partial (h\overline{\sigma}_x y)}{\partial x} - \tau_{yz} + g\rho h. \tag{2.14}$$

The slab is represented with an elastoplastic model following a Modified Cam-Clay

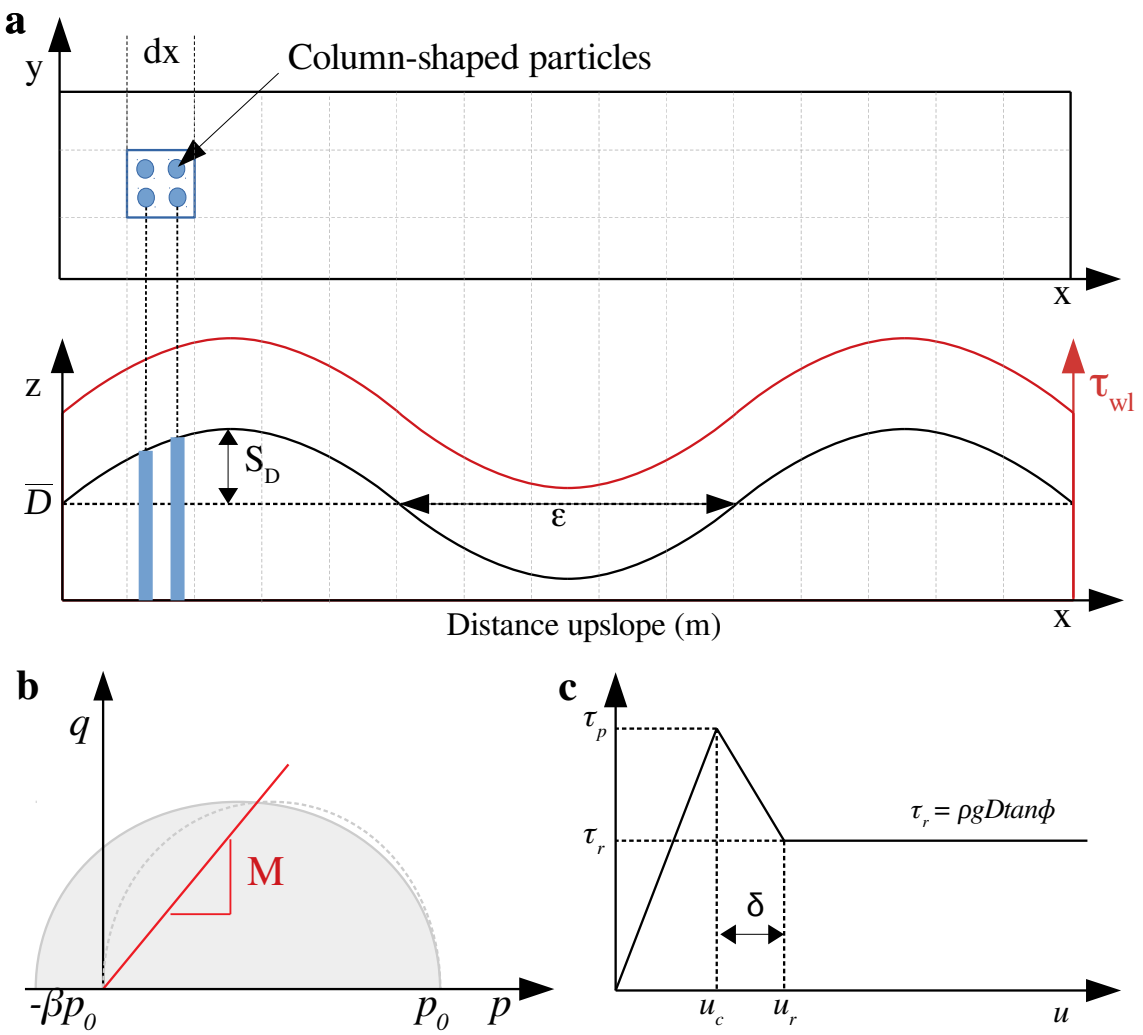

Figure 17 – DAMPM model and simulation parameters. (a) The geometry of the simulated propagation saw test PST with a sinusoidal slab depth variation and shear strength associated. The slab depth variation parameters from the sinus function are the mean slab depth $\overline{D}$, the standard deviation S_D, and the correlation length ϵ. (b) Slab elastoplasticity model following a Modified Cam-Clay yield surface. (c) Weak-layer model as quasi-brittle interface.

yield surface γ in the $p - q$ space (Gaume *et al.*, 2018b):

$$\gamma(p, q) = q^2(1 + 2\beta) + M^2(p + \beta p_0)(p - p_0) \tag{2.15}$$

where M is the cohesionless critical state line, β is the cohesion parameter that quantifies the ratio between the tensile and compressive resistance and p_0 is the consolidation pressure that affects the size of the yield surface. With M and β being constant respectively at 0.3 and 1.2, we related the slab tensile strength σ_t to p_0:

$$p_0 = -(1 - \beta) + \sqrt{\left(\frac{(\beta + 1)p}{2\beta}\right)^2 + \left(\frac{q}{M}\right)^2 \left(\frac{(1 + 2\beta)}{\beta}\right)} \tag{2.16}$$

where $p = \frac{\sigma_t}{\sqrt{3}}$ and $q = \frac{\sigma_t}{2}$ considering the plane stress hypothesis. The weak layer is an external force represented by a quasi-brittle interface with a softening behavior when the displacement u reaches the critical displacement u_c defined by the shear stress reaches τ_p (Figure 17). Then we have the softening until the displacement reaches the residual displacement u_r defined by the residual friction τ_r. The softening displacement is set to $\delta = 2u_c$, as suggested in Gaume *et al.* (2013). The snow parameters are the same as in the skier method regarding snow density and elastic modulus, as they are set according to the mean slab depth values of the simulated slope via a power-law fit. The shear strength is set according to the local slab depth values in order to represent the friction for thicker slabs. The slope angle is also the same as the previous method set at 35°. We used the empirical power-law fit to link the slab tensile strength with the mean slab density according to Sigrist (2006):

$$\sigma_t = 2.4 \times 10^5 \left(\frac{\rho}{\rho_{ice}}\right)^{2.44} \tag{2.17}$$

The depth-averaged material point method is more computer-intensive and time-consuming compared to the analytical method. A GRF simulation of the slab depth required at least 50 simulations per set of GRF parameters in order to obtain a statistical distribution and get

representative results. We changed our approach and simulated a sinusoidal slab depth variation in order to reduce the number of simulations to one and have a deterministic view. The variance parameter is changed to standard deviation S_D representing the amplitude of a sinus function (Figure 17). We simulate very long propagation saw tests (PST) of 75 m in the up-slope direction and 0.30 m wide (Gauthier and Jamieson, 2008). For each simulation, the cohesion is numerically removed from the bottom of the slope to obtain a critical crack length that will start the dynamic crack propagation across the slope. Finally, a tensile fracture is needed in the slab to be released from the slope and create a slab avalanche. This type of fracture in the slab occurs when the tensile stress in the down-slope direction (σ_{xx}) reaches the tensile strength of the slab σ_t. The distance to the first tensile fracture in the slab is noted for each simulation, we called this distance the tensile length L_t.

2.5 Results

2.5.1 Sensitivity analysis of the skier-triggering probability

The probability of skier-triggering decreases with the increase of the mean slab depth as expected (Figure 18). The homogeneous cases with zero variance show stable snowpack for skiers triggering from 0.6 m to 1 m slab depth. We observed two distinct regimes, one for a slab depth of 0.5 m where every skier is triggering for both homogeneous or heterogeneous cases. The second regime is defined with a 1 m mean slab depth where every skier doesn't trigger except for the larger variance at 0.025 m^2. There is an intermediate regime for the other values of mean slab depth which is affected by both the variance and the correlation length. The probability of skier-triggering increases with the slab depth variance. The increase in the slab depth variance allows some areas of the fictional slope to have shallow slab depth and create weak zones where the SPI is below 1. The increase of the correlation length is decreasing the skier-triggering probability. This decrease is caused by the reduction of the number of weak spots with SPI below 1 across slopes. A small correlation length creates

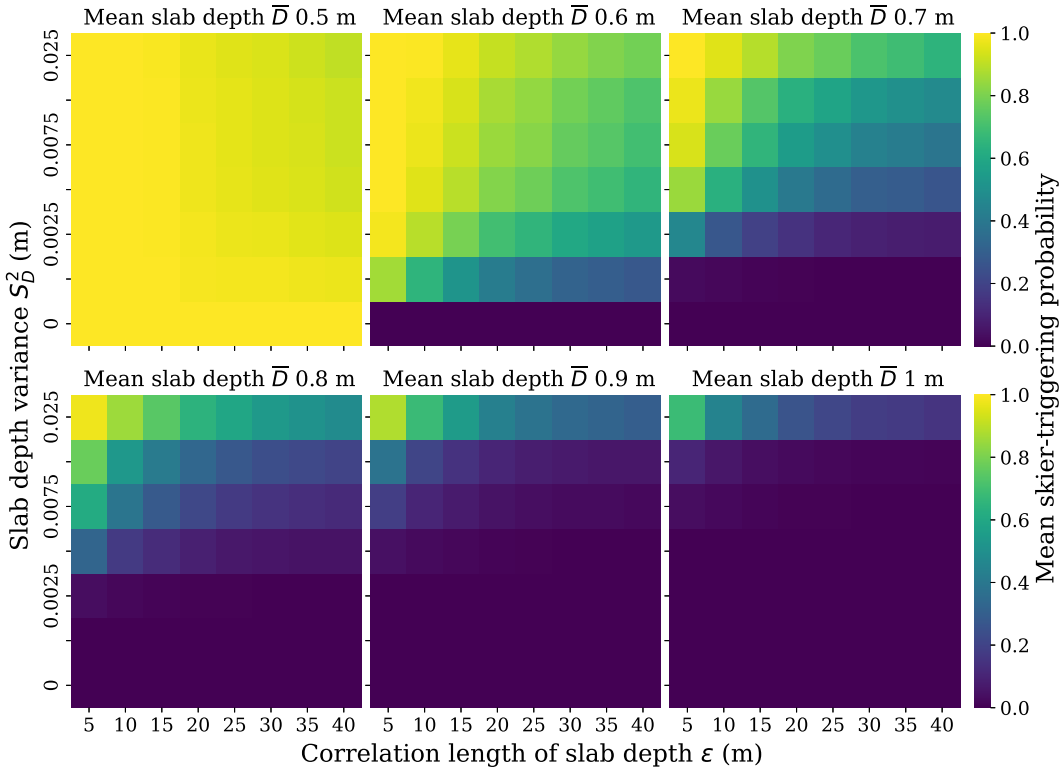

Figure 18 – Sensitivity analysis for the mean skier-triggering probability with regards to the mean, spatial variance and correlation length of the slab depth. The mean probability is computed from a distribution of 100 realizations for each specific set of mean slab depth, variance and correlation length

more weak spots where SPI is below 1 and a large correlation length creates fewer but bigger weak spots with SPI below 1. Instead of the mean presented above, we looked into the distribution of the skier-triggering probability containing 100 realizations. Figure 19 shows different probability density functions for each specific set of GRF parameters. With a mean probability below 0.3, the distribution is skewed towards 0 like a log-normal distribution. For cases where the mean skier-triggering probability range from 0.3 to 0.6, the distribution is relatively flat and centered, like a normal distribution. Even if the mean value is around 0.4 or 0.5, the variance of these distributions is quite large from 0.2 to 0.8 skier triggering probability. This means that for the same GRF parameters, some realizations were very unstable with more than half of the skiers triggered an avalanche and some realizations with

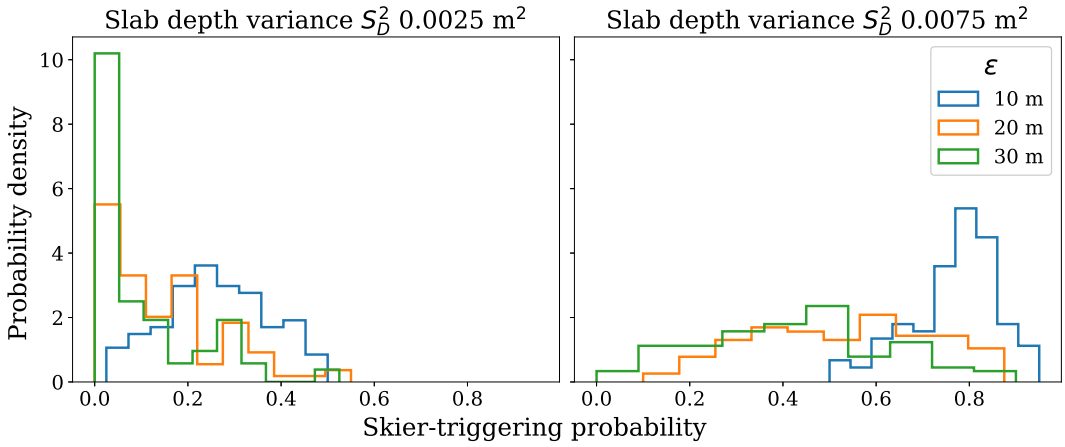

Figure 19 – Probability density function of the skier-triggering probability for mid to low mean skier-triggering probability. All the distributions presented are from a GRF using a 0.7 m mean slab depth, 0.0025-0.0075 m^2 slab depth variance, and 10-20-30 m correlation length.

very few skiers triggered. These cases in the intermediate regime described above from 0.6 to 0.9 m mean slab depth, the spatial variability of slab depth adds uncertainty to the probability to trigger an avalanche by a skier. With a mean probability above 0.8, the distribution is normally distributed around the mean values.

2.5.2 Influence of the skiing style

The previous analysis was conducted using a constant skiing style defined by a 10 m down-slope turn radius (R_{down}) with a 5 m cross-slope amplitude (A_{cross}) (Figure 16). However, these two parameters should influence the trajectory of each skier and therefore, should also affect the probability of the skier hitting a weak spot. We made a sensitivity analysis of these two parameters. We test multiple values in order to get a down-slope linear trajectory and the complete opposite with a trajectory that will traverse the entire slope in the cross-slope direction. These two extreme trajectories should mimic a freeride down-hill skiing trajectory (linear down-slope) compared to an up-hill skinning trajectory (cross-slope). Figure 20 shows that for a large A_{cross}/R_{down} ratio, the mean skier probability is increasing towards

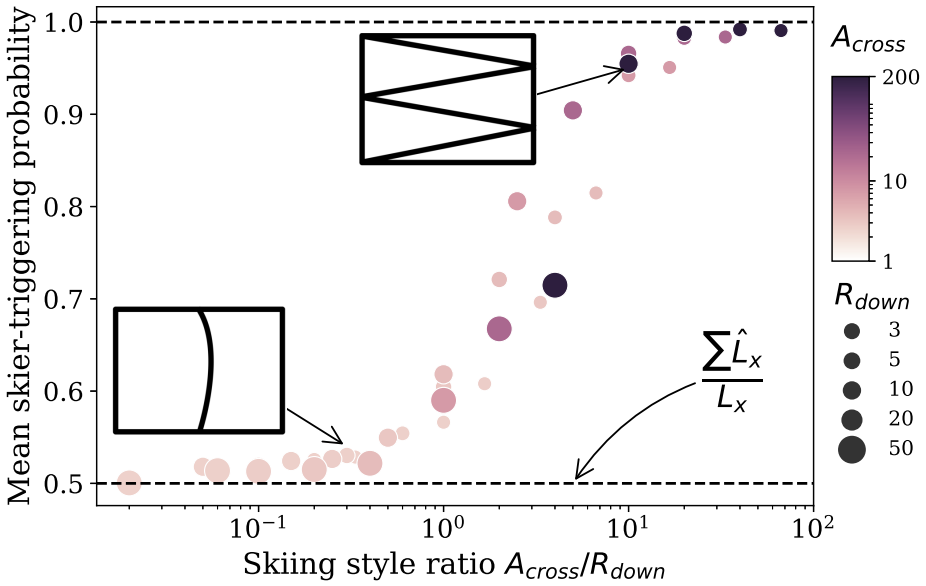

Figure 20 – Mean skier-triggering probability from 100 realizations for different skiing style ratios A_{cross}/R_{down}. A_{cross} represents the cross-slope amplitude and R_{down} represents the down-slope turn radius. A small skiing style ratio represents a linear down-slope trajectory and a large skiing style ratio represents a cross-slope trajectory. The probabilities are constrained by two values: the first is a probability of 1 where all skiers have triggered, and the second value is a linear weak spot cross-slope ratio between the sum of weak spot length in the cross-slope direction compared to the total cross-slope length. The dashed line is set at 0.505 which is the mean of the linear weak spot cross-slope ratio for 100 realizations for this set of GRF parameters: mean slab depth of 0.7 m, variance of 0.0075 m^2, and 20 m correlation length. This line should move with regard to the GRF parameters. The inlets represent schematic skiing style based on the skiing style ratios.

a probability of one with positive hits for every skier, meaning that a trajectory with a large cross-slope amplitude is more likely to encounter weak spot and trigger an avalanche. For a small A_{cross}/R_{down} ratio, the mean skier probability is decreasing towards a value determined by a ratio that we called the linear weak spot cross-slope ratio($\frac{\sum \hat{L}_x}{L_x}$). This ratio indicates the minimum probability of a purely linear trajectory specific to each realization per set of GRF parameters. Note that the 0.505 found in Figure 20 represents the mean of the linear weak spot cross-slope ratio for 100 realizations for a mean slab depth of 0.7 m, variance of 0.0075 m^2, and 20 m correlation length.

2.5.3 Influence of group size and terrain choice

We investigated the influence of the group size on the skier-triggering probability. Here, we want to test the hypothesis that it is safer to ski near a preexisting ski track that is considered safe, compared to a completely random approach. We randomly selected a position at the top of the slope to start the first skier, and if the first skier track didn't record a hit on a weak spot, we keep adding a skier 5 m apart until a trigger was recorded or the slope was entirely skied. We repeated this operation 50 times on one realization and repeated it for 100 realizations for a 0.7 m mean slab depth and 0.005 m^2 variance, with four different correlation lengths (5, 10, 20, 30 m). Figure 21 is showing that for a correlation of 5 and 10 m, the random and structured approaches have a similar experimental cumulative density function (ECDF) but the structured approach is slightly shifted. The ECDF for the 5 and 10 m correlation length had a median of one or two additional skiers which can be translated into a slightly lower skier-triggering probability compared to the 20 and 30 m ECDF. For the simulation with a correlation length of 20 and 30 m, the ECDF of the structured approach is completely shifted from the random approach, towards more additional skiers before triggering. The ECDF is starting at two additional skiers for the 20 m and the 30 m distribution, which means that a minimum of two additional skiers were needed before recording a trigger compared to the random approach, from all the 5000 simulations represented in one ECDF. The difference is more significant for the median of the ECDF, the random approach as between 3 to 4 additional skiers before the trigger compared to the structured approach with 7 skiers (20 m) and 10 skiers (30 m).

2.5.4 Tensile length and avalanche release size

Figure 22 shows different simulations of PST for three different correlation lengths. During a dynamic crack propagation for a homogeneous case, the tensile stress σ_{xx} increased linearly as the unsupported slab grew from the damaged weak layer. Then, the tensile stress

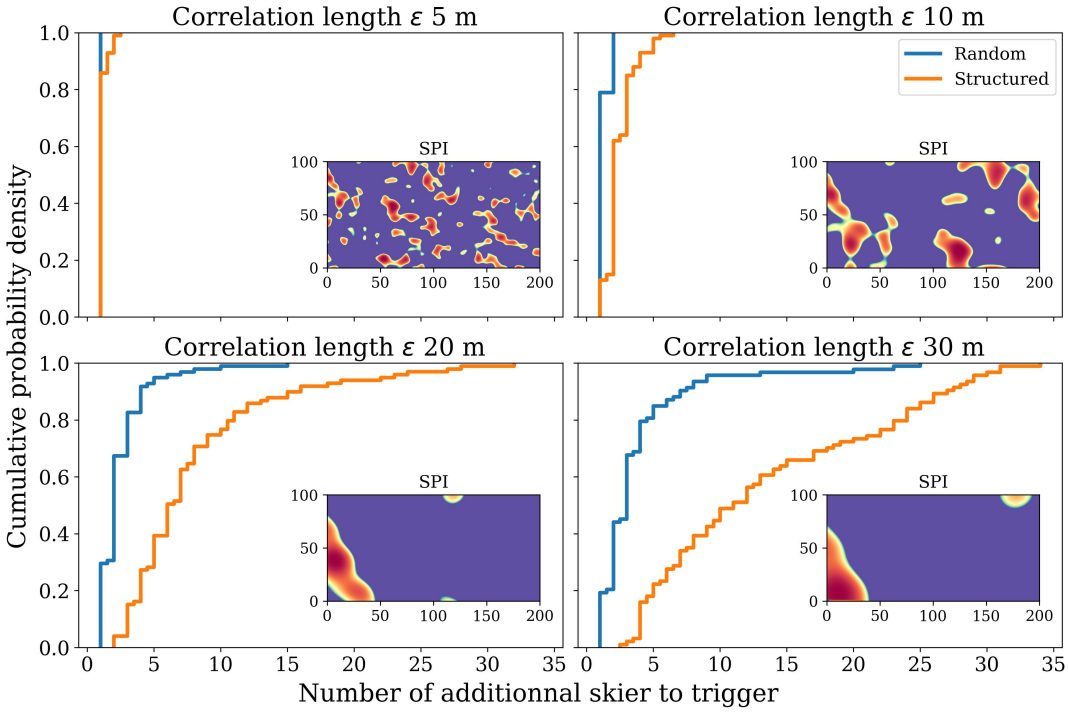

Figure 21 – Experimental cumulative density functions (ECDF) of the number of additional skier to trigger from mid to low mean probability. All the distributions presented are from a GRF using a 0.7 m mean slab depth, 0.005 m^2 slab depth variance, and 5-10-20-30 m correlation lengths. The inlets show examples of the corresponding SPI map specific to their GRF parameters.

σ_{xx} reached the tensile strength σ_t, and a tensile fracture in the slab is observed. The increase is linear because the shear stress is constant across the slope in a homogeneous case, as the crack tip moves across the slope at 1.6 c_s. However, the tensile stress pattern changed for different cases of slab depth variations. If the correlation length is large, around 25 m or more, the tensile length converges towards the homogeneous case because the tensile stress is increasing almost constantly. Figure 22-a shows a simulation for a mean slab depth of 0.7 m, a standard deviation of 0.25 m, and a correlation length of 30 m where the tensile stress σ_{xx} is constantly increasing in the lower part of the slope (distance up-slope < 20 m). Then, the tensile stress increases non-linearly to reach the tensile strength at ≈ 34 m. Tensile stress σ_{xx} increases rapidly as shear strength τ_p and shear stress τ_{xz} reduces around 25 m. This smooth spatial variability with a long correlation length results in a tensile length similar to the homogeneous case. Figure 22-b shows a simulation for a mean slab depth of 0.7 m, a standard deviation of 0.25 m, and a correlation length of 15 m where the tensile stress fluctuates as the crack tip moves across the slope. The same nonlinear increase is observed around 15 m up-slope in the tensile stress, but then it decreases as the slab depth, the shear stress, and strength increase again around 25 m up-slope (Figure 22-b). Finally, the tensile stress increases a second time as the slab depth, shear stress and strength start to decrease around 40 m up-slope (Figure 22-b). In this particular case, the spatial variability of the slab depth and the underlying weak layer strength cause a fluctuation in the tensile stress of the slab σ_{xx}, resulting in a longer tensile length. Figure 22-c shows the same fluctuation in tensile stress but for a 10 m correlation length. The fluctuation in tensile stress is more significant and closer to the bottom of the PST, leading to a shorter tensile length. From a static point of view, tensile stress builds as the length of the ”unsupported” slab increases due to weak layer damage and crack propagation. The tensile stress is equal to the load from the slab in the down-slope minus the friction of the slab weight. This relation is linear assuming a constant slab depth. However, our system had a variation in slab depth that will also cause a variation in the friction effect that is more pronounced where the slab is locally thicker and explains why the tensile stress locally reduces where the slab is thicker (Figure 22). Dynamic effects

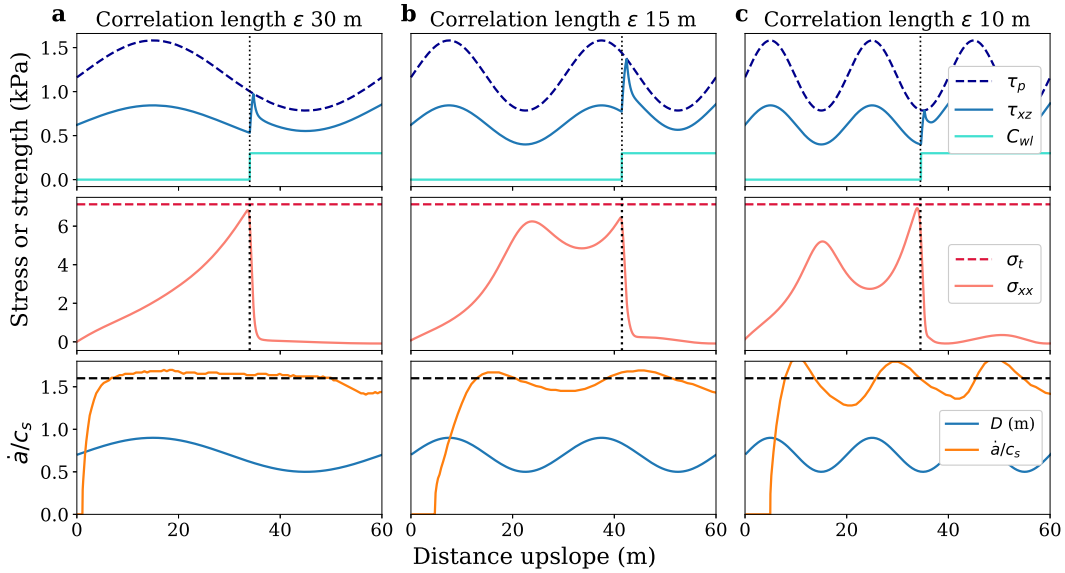

Figure 22 – Three different regimes of tensile fracture for a 0.7 m slab depth $\overline{D}$ and 0.25 m S_D. These three simulations show the last frame saved just before the tensile fracture occurs when $\sigma_{xx} = \sigma_t$. The shear stress τ_{xz} and the weak layer shear strength τ_p and the cohesion C_{wl} are also represented. The crack tip (dotted line) is located just behind the peak of τ_{xz} at the loss of cohesion C_{wl}. The distance between the crack tip and the τ_{xz} peak is due to the softening δ. The bottom plot shows the corresponding crack speed $\dot{a}$ which is normalized over the shear wave speed $c_s = \sqrt{\frac{G}{\rho}}$, and the slab depth D in m. (a) PST simulation with a ϵ 30 m just before a tensile fracture occurs. (b) PST simulation with a ϵ of 15 m just before a tensile fracture occurs. (c) PST simulation with a ϵ of 10 m just before a tensile fracture occurs.

could also explain some fluctuations in the tensile stress. In fact, variations in shear stress and weak layer strength lead to variations in crack speed around 1.6 c_s, which can also cause fluctuations in tensile stress.

We present a sensitivity analysis of the propagation distance that results in the first tensile fracture (L_t) from our numerical PST experiment. Figure 23 shows all the results from our simulations with different mean slab depth values $\overline{D}$, slab depth standard deviation S_D (sinus function) and correlation length ϵ. The homogeneous tensile length is obtained here based on a simulation with homogeneous slab depth (i.e. standard deviation of zero). This homogeneous tensile length increased with the slab depth even if the theoretical quasistatic

tensile length is in principle not linked to the slab depth ($L_t = \frac{\sigma_t}{\rho g \sin\psi}$). However, in our study, the slab density and tensile strength are related to the mean slab depth (Eq. 2.3-2.4), which explains the reported increase in the tensile length obtained for our homogeneous cases (Figure 23). A shorter tensile length is obtained as the standard deviation increases. A longer tensile length is obtained as the correlation length increases around 25 m, then, it converges towards the same values as the homogeneous case. We observed a tensile length approximately 20 m shorter than the homogeneous case when the standard deviation is 0.2 m and a correlation length of 10 m or less. The tensile length is only longer than the homogeneous case for a correlation length of 15 m and 20 m for higher slab depth, but also for a standard deviation of approximately 0.1 m and higher (Figure 23). This regime with larger tensile lengths is more pronounced for thicker slab depth. This particular regime with longer tensile lengths, which is associated with a correlation length of 15 or 20 m, is caused by the use of the sinus function. This function caused an increase in the weak layer strength around 30-40 m, which reduced the tensile stress in the slab just before it would have reached the tensile strength σ_t, thus resulting in a longer tensile length (Figure 22-b). The correlation length has a major influence on the strength of the weak layer, τ_p, with a shorter correlation length causing the peak to move closer to the bottom of the slope, resulting in a shorter tensile length than in the homogeneous case. However, cases with a longer correlation length (> 25 m) have a similar behavior as cases with homogenous properties. (Figure 22-a). The sharp transition in tensile length around 15-20 m of correlation length in our result (Figure 23) is due to the sinus function itself, and this could be smoothed out by performing numerous simulations with sinus functions of different phases (i.e. by shifting the origin of function) or by using a GRF-based simulation (Appendix Figure 41).

To further investigate the results presented above in the case of a sinus function, we used GRF to simulate slab depth variation for a few GRF parameters. Figure 24 shows the distribution of tensile lengths from 50 realizations for four different sets of GRF parameters. The dashed line represents the homogeneous tensile length. For the small variance S_D^2 (0.005 m^2), the distribution is narrow and centered around the homogeneous tensile length. For the

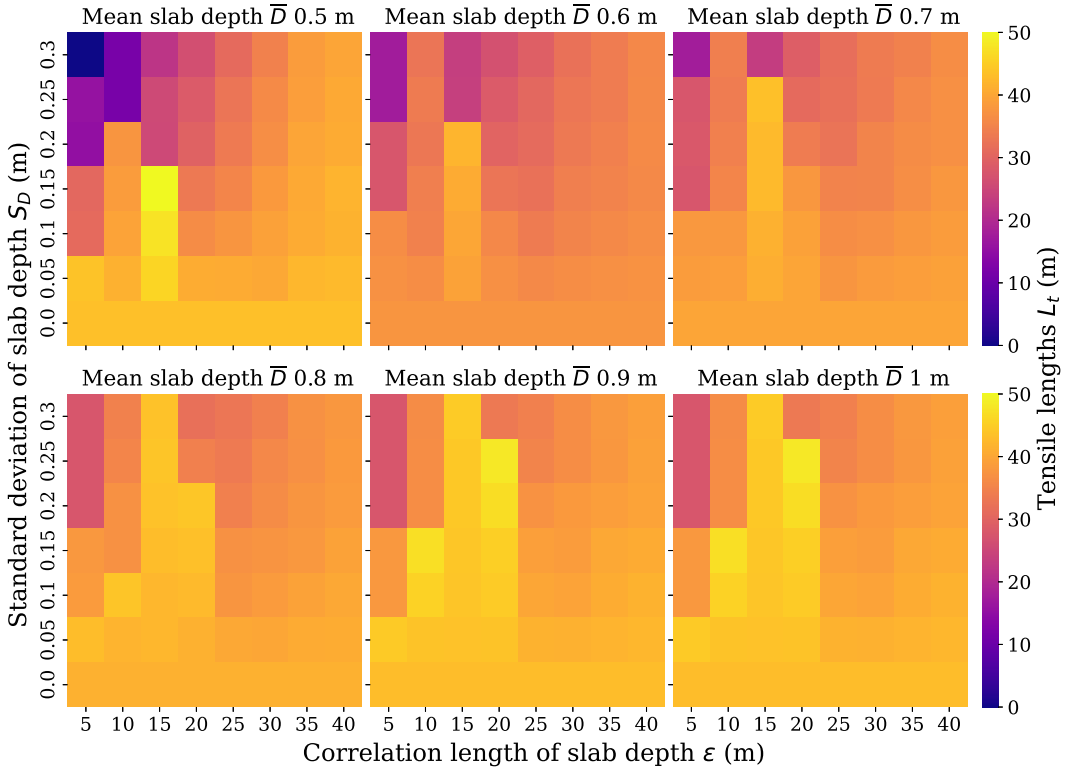

Figure 23 – Sensitivity analysis for the tensile length L_t with regards to the mean $\overline{D}$, standard deviation S_D and correlation length ϵ of the slab depth sinus function.

higher S_D^2 (0.025 m^2), the distribution of tensile length has a large variance, especially for the 5 m correlation length with values of tensile lengths ranging from 10 to 50 m. The distribution for a 1 m slab depth has nearly the same distribution shape, which is narrow for a small value of 0.005 m^2 S_D^2 and wider for a S_D^2 of 0.025 m^2 (Figure 24). The variance of tensile length distribution is smaller for a 1 m mean slab depth compared to the 0.5 m distributions. The medians of tensile length distributions for the 1 m mean slab depth are larger compared to the homogeneous values denoted by the dashed line in Figure 24. The distributions are shifted towards bigger tensile length values compared to the homogeneous tensile length, with either a small or high variance (Figure 24). This could be explained by a larger friction effect by the 1 m mean slab depth, causing a less important build-up of tensile stress in the slab which resulted in tensile length values larger compared to the homogeneous tensile length.

2.5.5 Skier-triggering probabilities versus potential avalanche release sizes

This last result section presents both the sensitivity analysis of the skier-triggering probability and the potential avalanche release size. To obtain the potential size of the avalanche release, we multiplied the tensile lengths by the mean slab depth to get an estimate of the volume of snow mobilized for the avalanche. Typically the avalanche release size is computed from the volume of snow in movement but our simulations setup does not include the cross-slope length of the potential avalanche. Figure 25 shows both the probability of skier-triggering and the potential avalanche release size. The skier-triggering probability appears to be inversely related to the mean slab depth because the force induced by a skier at a given depth is inversely proportional to the depth. On the contrary, the potential avalanche release size increased with slab depth. We obviously got a correlation as we multiplied the tensile length by the mean slab depth to get the potential avalanche release size. However, the tensile strength in our simulations was parametrized based on the mean slab depth which also explains the longer tensile length values for thicker and stronger slabs. Furthermore, Figure 25 shows that the skier-triggering probability is increasing, with increasing the standard de-

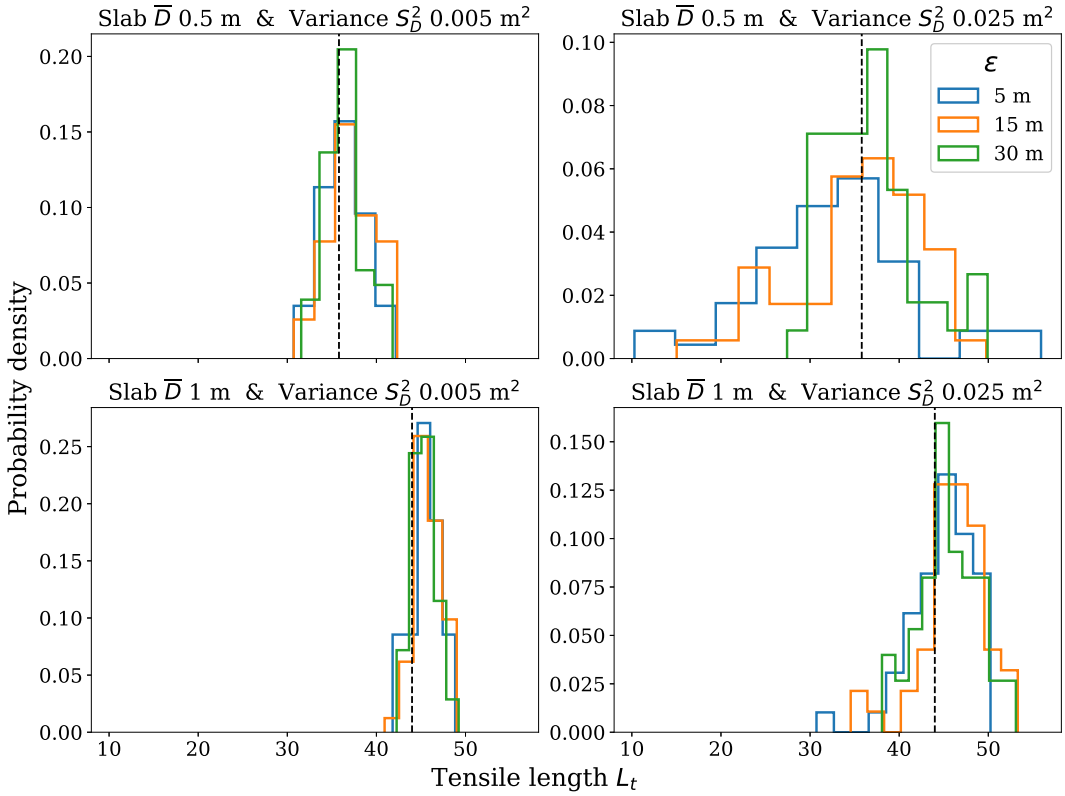

Figure 24 – Probability density functions of tensile lengths L_t of 50 realizations for different mean slab depths $\overline{D}$ of 0.5-1 m, different variances S_D^2 of 0.005-0.025 m^2, and 5-15-30 m correlation lengths ϵ. The dashed line represents the homogeneous tensile length for a mean slab depth of 0.5 m and 1 m.

viation for a given mean slab depth. However, the avalanche release size should be smaller when the standard deviation is increasing, but this result should be nuanced because Figure 24 shows that with a more natural spatial variability generated from a GRF, the avalanche size is quite variable compared to the homogeneous case but tends to be larger while the mean slab depth is increasing. The area in the heatmap where the maximum probability is correlated with the area of minimum potential avalanche release size, and the opposite is also present with the minimum of probability with the maximum size (Figure 25). For the same mean slab depth values, high variation leads to a high skier-triggering probability but a lower potential avalanche release size. As the mean slab depth increases, the skier-triggering probability decreases to a point that for 0.9 and 1 m mean slab depth, the probability to trigger by a skier is almost impossible except with high slab depth variation, but the trigger could lead to relatively larger avalanches. These cases represent a scenario of low probability but high consequences with large avalanches, and this scenario is only possible with a slab depth spatial variation.

2.6 Discussion

2.6.1 Relevance of the study for practical implications

This study presents a novel mechanical-statistical approach to understanding the influence of slab depth spatial variability on the skier triggering probability of potential avalanche size. First, we showed a sensitivity analysis of the three parameters defining the variability. The increase of skier-triggering probability is inversely proportional to the mean slab depth, which was expected considering previous studies on this matter but without slab depth variation (Föhn, 1987; Monti *et al.*, 2016; Gaume and Reuter, 2017). However, we show that the tensile length and the potential avalanche size are increasing proportionally to the mean slab depth, which is in agreement with previous studies showing that thicker and stronger slabs promote larger avalanches (Gaume *et al.*, 2015a). The variance and the correlation length

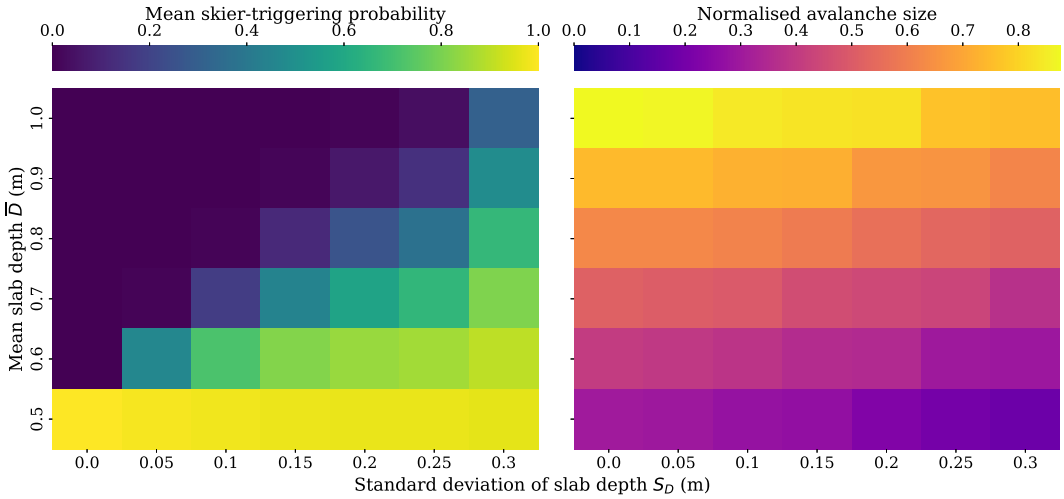

Figure 25 – Probability of skier-triggering and normalized potential avalanche release size in relation to the mean slab depth and standard deviation of the slab depth. Potential avalanche release size combines the tensile length normalized with the largest tensile length multiplied by the mean slab depth. We show the standard deviation slab depth values for visual purposes but the variance values used with GRF method yield approximately the same values as the standard deviation slab depth used with the sinus function.

results from the sensitivity analysis could be interpreted together. The combination of both creates some propagation spots (SPI below 1) on the fictional slope that skiers triggered. As the variance increases, it creates more propagation spots on the slope because it creates more areas where the slab is thinner so the skier can trigger the weak layer. A smaller correlation length leads to several small weak spots distributed across the slope compared to cases with longer correlation lengths, which led to fewer weak spots that cover more surface on the slope. The higher number of weak spots created using a smaller correlation length induced a higher skier-triggering probability than in the case with fewer weak spots covering more surfaces. In brief, a short-range variation creates numerous propagation spots leading to an increase in the skier triggering probability. Interestingly, several studies investigated the effect of the weak spots, created by heterogeneity in the weak layer, on natural release and obtained opposite conclusions (Gaume *et al.*, 2013, 2014). The short-range variation of the weak layer creates several weak spots that are distributed across the slope like the short-range variation of slab depth. These short-range variations can be smoothed due to the elasticity

of the slab (Gaume *et al.*, 2013) and reduce the probability of a natural avalanche occurring. These studies also found that long-range variations create fewer weak spots but these weak spots were larger and covered more surfaces. This long-range variation was destabilizing the entire slope, in line with the so-called knock-down effect (Kronholm and Schweizer, 2003; Fyffe and Zaiser, 2004; Gaume *et al.*, 2014). Finally, the variation of the snow mechanical properties (slab depth or weak layer cohesion), creates a spatial distribution of weak spots on the slope, and this variation does not have the same effect regarding the type of trigger between a skier (more unstable with a short-range variation) compared to a natural release (which is more unstable with a long-range variation).

This study also had an implicit objective to apply the method to test common knowledge that practitioners of the avalanche industry developed through many years of experience in the field. We realized that our method was heavily dependent on the skier style of the simulated skier trajectory. We show that a linear trajectory with a high down-slope radius R_{down} and a small cross-slope amplitude A_{cross}, reduce significantly the odds of triggering a weak spot. These results should be applied carefully in practice because it doesn't imply that skiing straight down the slope is "safer", whatever the term safer implicated in this context, but it only reduces the probability of triggering a weak spot resulting in an avalanche. The opposite trajectory was also simulated with a very high cross-slope amplitude and a small down-slope radius, representing an up-slope trajectory which we can translate to skinning up the up-slope with conversion (Figure 20). Backcountry recreationists should not base their decision to ski a particular slope on their skiing trajectory. Decision-making in avalanche terrain is a complex task with many different aspects like terrain features, safety management, and other mountain hazards (Harvey *et al.*, 2023)

We wanted to test if it was safer to ski closer to a preexisting ski track. Figure 21 shows a comparison between a structured approach that mimics skiing closely to a preexisting ski track from a completely random approach. The ECDF with a long correlation length had a median from 7 to 10 skiers on the slope before recording a trigger. It is important here to

notice that in this method, the ECDF only represents cases where the first skier did not trigger, and then we started to add additional skiers both in a structured and random approach. The use of a safe first skier track is important because it mimics the fact that preexisting ski tracks could give information to other skiers that this trajectory did not trigger. Then, in spatial variation with a long correlation length like 30 m, the distance to the next weak spot could be on average 30 m away, explaining the fact that many skiers, with a spacing of 5 m could be on the slope before recording a trigger. These results confirm and quantify common knowledge used by ski guides and in avalanche awareness communication (Harvey *et al.*, 2023).

Our results showed that the slab depth spatial variability adds randomness and unpredictability to skiing an avalanche-prone slope. A spatially homogeneous slab creates a binary outcome: either each skier triggers the avalanche or none do. But, the spatial variability of the slab depth creates a third regime in which some skiers trigger the avalanche and some do not on the same slope. The slab depth spatial variability creates weak spots on the slope which the skier trajectory will determine the outcome. The randomness is a result of the arbitrary anisotropic trajectory (down-slope) of the skier toward a potential weak spot on the slope. Our results also showed randomness in the tensile length obtained from our GRF simulations. The variation of slab depth sometimes induced an early crack arrest resulting in shorter tensile length, and sometimes the opposite outcome. The slab depth variation influences the crack speed during crack propagation. The observed increase in the speed of the crack caused a decrease in the tensile stress building up on the slab, which led to a longer tensile length. The same phenomenon was observed when the slab depth variation was slowing down the crack propagation, causing a sharp increase in tensile stress.

The last result presented in this study is the comparison between the skier triggering probability and the potential avalanche size. We show that it is more probable to trigger thinner and softer slabs compared to thicker and stronger slabs, but these thicker and stronger slabs could potentially create larger avalanche release sizes, also described and modeled by Gaume *et al.* (2015a). The increase of the slab depth standard deviation has an ambiguous

effect because it increases the skier-triggering probability but reduces the avalanche release size. This latter was also observed by Gaume *et al.* (2015a) but regarding the variation of the weak layer cohesion instead of the slab depth on the avalanche release size. The relation between the likelihood to trigger by a skier compared to the propensity of propagation was initially described, through stability tests and field observations by van Herwijnen and Jamieson (2007). However, this study focused on fracture initiation and the propensity of propagation but not the potential avalanche size which refers to the dynamic crack propagation. Our statistical-mechanical provides a physically-based validation and includes the effect of spatial variability of this well-known relationship (Figure 25) which is the basis to describe the avalanche hazard in several countries (Techel *et al.*, 2020; Statham *et al.*, 2018).

2.6.2 Limits of the study and outlooks for future work

The novel methods used in this study present some limitations and assumptions that could be explored in future work. The analytical method considered the skier loading static along the skier tracks. In reality, the skier adds more pressure to the snow cover at the apex of each turn. This additional pressure in the apex could potentially trigger the weak layer in thicker slabs. Also, skier penetration was not taken into account, and this could potentially affect some of the presented results. The additional pressure coupled with the skier penetration depth could increase the skier-triggering probability using a skiing style with more turns compared to a linear skiing style. In addition, in the DAMPM model, the volumetric collapse of the weak layer and the induced slab bending is not taken into account because of the depth-averaged assumptions. In principle, at such a scale on an inclined slope, the slab tension represented by the DAMPM model is significantly higher than the slab bending which is anyway limited by the slab touchdown slab behind the crack tip (Benedetti *et al.*, 2019).

We made the assumption that the weak layer strength would follow the slab depth variation locally. However, Bellaire and Schweizer (2011) has shown that is not always the

case and the weak layer and the slab spatial pattern could differ. The relation between the slab depth and the weak layer strength is mainly due to the settlement and the friction from the slab weight, but some variation could still remain. The weak layer could be parameterized using the Mohr-Coulomb relation proposed by Gaume *et al.* (2013), but with the friction term locally adjusted to the slab depth and the cohesion term could be set using a GRF with a different spatial pattern than the slab depth. This could lead to more realistic variations of snow properties and ultimately more realistic simulations. We choose not to follow this approach because we want to isolate only the slab depth variation in order to better understand individual drivers of the instability. Either approach should create weak spots triggered by skiers in the fictional slope, but maybe not in the same areas of the slope. However, the use of two different spatial patterns for the weak layer and the slab could create areas where the weak layer is stronger and the slab depth is thinner, the opposite of what this work is presenting. Such areas could promote slab tensile failure and potentially a crack arrest in the weak layer. Further investigations should be made on this matter to see if it could reduce the crack speed and potentially promote the crack to arrest, which we did not observe in our simulations. The covariance model used in the GRF did not contain any nugget. This choice created a smoother spatial realization of the slab depth without any ”noise” from the nugget. However, Kronholm and Birkeland (2005) has shown that increasing the nugget effect could promote crack arrest during dynamic crack propagation. This effect should be explored in future work regarding crack arrest and potential avalanche release size.

This study only investigates in numerical simulation the length at which the first tensile fracture occurred in the slab as a proxy to the potential avalanche release size. Tensile fracture is often related to crack arrest in the weak layer but not necessarily. There are no current studies to the best of our knowledge that explore the conditions of the crack arrest on an inclined snow slope. However, real-scale experiments on flat-terrain show some mechanical conditions when crack arrests were observed on 10 m long flat PST's (Bergfeld *et al.*, 2021). They demonstrate some dissipation of energy during the dynamic crack propagation which could reduce the crack speed and possibly induce a crack arrest without a slab frac-

ture. The dissipation of energy was due to the compression of the weak layer by the slab behind the crack tip. However, this phenomenon could be less important or may be absent on an inclined slope where the crack propagation changes to pure shear crack propagation (Trottet *et al.*, 2022). Other dissipation mechanisms could influence the crack arrest like the softening behavior of the weak layer. Further investigation should focus on the effect of the softening on energy dissipation and crack arrest. Strong heterogeneity in the weak layer and topography changes should also be explored to further explain the conditions for a crack to arrest, and ultimately estimate the potential avalanche release size.

2.7 Conclusion

This study demonstrates the influence of slab depth spatial variability on the skier-triggering probability and the possible avalanche release area using a novel mechanical-statistical approach. We show that the spatial variability slab depth could increase the skier-triggering probability for thicker slabs when in a homogeneous case, a trigger by a skier is unlikely. For the possible avalanche release size, we show that the spatial variability of slab depth can induce a fluctuation in the tensile stress causing an early tensile failure resulting in smaller avalanches and also the opposite with bigger avalanches depending on the scale of the variability. We used the tensile length as a potential proxy for crack arrest but further research should focus on drivers for crack arrest dynamic crack propagation.

This study provides quantification and scientific evidence on the common knowledge that practitioners have developed throughout years of experience in the avalanche industry. We demonstrate the effect of skiing style on the probability to trigger an avalanche. We validate the idea with scientific evidence that skiing near a preexisting skier track could reduce your probability to trigger an avalanche compared to a random approach. This study demonstrates some processes during dynamic crack propagation regarding the variation of slab depth along a 1D slope. However, more research is needed to understand which drivers

like topography or strong snow heterogeneity could potentially stop this dynamic crack propagation, both for the anticrack propagation in flat terrain and the super-shear regime on an inclined slope. Finally, this study shows, validates, and quantifies the well-known relationship between the likelihood and the size of an avalanche as well as common knowledge for safety guidelines in the avalanche community.

2.8 Acknowledgements

We want to thank all the SLAB members at EPFL, including Lars Blatny, Bertill Trottet, Hugo Rousseau, Thomas Pauze, Roxanne Fayant and Grégoire Bobillier who participated in the discussion and shared enthusiasm regarding this study during team meetings and coffee breaks. We also want to thank Stephan Harvey for his useful comments regarding the practical implications of this study. We thank Karl Birkeland and an anonymous reviewer for their helpful and constructive comments.

ARTICLE 3

COMPRENDRE L'ARRÊT DE LA PROPAGATION DYNAMIQUE DES FISSURES DANS LES AVALANCHES DE PLAQUES: VERS UNE ESTIMATION DE LA TAILLE DE L'AVALANCHE

3.1 Résumé en français du premier article

Les avalanches de plaques de neige sèche sont considérées comme les plus difficiles à prévoir, mais aussi comme les types d'avalanches les plus meurtrières. Le déclenchement des avalanches de plaques de neige commence par la rupture d'une couche de neige faible enfouie sous des plaques de neige cohésives. Cette rupture initiale peut se propager sur la pente jusqu'à ce que la plaque se fracture et glisse. L'évaluation de la zone de propagation de la fissure et de la taille potentielle de l'avalanche est une préoccupation majeure pour les prévisionnistes d'avalanches. Le but de cette étude est de tester l'hypothèse selon laquelle deux facteurs principaux peuvent potentiellement arrêter la propagation dynamique de la fissure : l'hétérogénéité des propriétés du manteau neigeux et les variations locales du terrain. Pour tester cette hypothèse, nous utilisons et développons davantage une moyenne en épaisseur *Depth Averaged Material-Point Method* (DA-MPM) qui intègre la *Material-Point Method* (MPM) avec les hypothèses classiques *shallow water* pour une modélisation élasto-plastique efficace des avalanches de plaques de neige. Notre analyse inclut des scénarios impliquant i) des plaques purement élastiques et ii) des plaques élasto-plastiques. Dans le premier scénario, nous rapportons une diminution significative de la contrainte de traction de la plaque avec l'augmentation de la vitesse de fissure et proposons une formulation analytique expliquant la réduction de la contrainte par rapport à la théorie quasi-statique. De plus, nous quantifions l'effet de l'hétérogénéité de la couche faible et de l'énergie de fracture de ramollissement sur le mécanisme d'arrêt de la fissure. Dans le deuxième scénario,

nous analysons l'interaction entre l'hétérogénéité de la couche faible et la fracture de traction de la plaque et quantifions leur effet combiné sur l'arrêt de la fissure. Les résultats sont interprétés à travers une loi d'échelle reliant la distance d'arrêt de la fissure à deux nombres sans dimension liés à la variabilité de la résistance de la couche faible et à la fracture de traction de la plaque. Ces nombres intègrent les paramètres clés régissant la longueur d'arrêt de la fissure, offrant des informations importantes sur la taille des zones de déclenchement des avalanches. En outre, le modèle proposé est appliqué à deux études de cas correspondant à des campagnes de terrain dans lesquelles les variations spatiales de la résistance au cisaillement de la couche faible ont été mesurées. Sur la base des mesures, on peut obtenir une indication de la taille de la zone de déclenchement en utilisant le modèle proposé. Enfin, des simulations DA-MPM sont effectuées sur un terrain 3D avec des variations spatiales dans la direction parallèle à la pente, et dans la direction transversale à la pente, révélant des schémas de déclenchement intéressants. Cette recherche et les méthodes proposées peuvent non seulement améliorer notre compréhension des facteurs mécaniques et géométriques influençant les tailles de déclenchement des avalanches, mais aussi informer, à l'avenir, la conception de nouvelles ouvrages géotechniques d'atténuation ou l'amélioration d'ouvrages existants pour les zones de départ des avalanches.

Ce dernier article, intitulé "*Understanding crack arrest during dynamic crack propagation in snow slab avalanches: towards estimating the avalanche release size*", fut rédigé par moi-même et assisté par mes collègues Grégoire Bobilier du l'Institut fédérale suisse de recherche sur la neige et les avalanches SLF, Louis Guillet de l'Université Grenoble-Alpes INRIA, mon directeur Francis Gauthier, de mon codirecteur Alexandre Langlois de l'Université de Sherbrooke et finalement, le professeur Johan Gaume de l'École Polytechnique fédérale de Zürich. Cet article devrait être soumis tout prochainement à la revue *Canadian Geotechnical Journal*. Ma contribution en tant que premier auteur a été de conceptalisé la recherche en collaboration avec professeur Johan Gaume et mon collègue Grégoire Bobillier. Louis Guillet a développé la méthode numérique *Depth-averaged Material-Point-Method* avec l'aide de Johan Gaume. Ces derniers (Grégoire, Louis et Johan) ont prodigué de

nombreux conseils durant l'ensemble du travail qui ont grandement amélioré la pertinence et la qualité de présentation de l'article. Francis Gauthier et Alexandre ont contribué significativement aux développement de la recherche avec de nombreux conseils. Ils ont également contribué à la rédaction et la correction de l'article. J'ai rédigé le premier jet de l'article et l'ensemble des co-auteurs ont aidé à la révision de l'écriture de l'article. Une version abrégée de cet article a été présentée à la conférence *International Snow Science Workshop* à Bend, Oregon (États-Unis) à l'automne 2023.

3.2 Understanding crack arrest during dynamic crack propagation in snow slab avalanches: towards estimating the avalanche release size

3.3 Introduction

The release of snow slab avalanches can lead to significant volumes of fast-moving snow that can endanger people and infrastructure. It is essential to assess the size of the release area as this is a key indicator of the destructive power of the avalanche and thus a crucial parameter for risk assessment. For many years, research has been conducted to better understand the process of dry snow slab avalanches to accurately assess the stability of the snowpack (e.g. Föhn, 1987; McClung, 1981; Schweizer *et al.*, 2003; Monti *et al.*, 2016), which is necessary for avalanche forecasting. The release of a dry-snow slab avalanche requires the presence of a weak snow layer buried below cohesive snow slabs. Additional loading, such as a skier or new snowfall, can induce failure of the weak layer. The length of the failure, or crack, must exceed a so-called critical crack length to self-propagate along the slope in the weak layer. Once the propagation has started, tensile stresses build up in the slab as a result of slope-parallel displacements. Eventually, the tensile stress may reach the tensile strength of the slab, causing a slab fracture perpendicular to the weak layer, leading to the release and sliding of the slab down the slope (Schweizer *et al.*, 2016). Numerous studies have been conducted on the initiation of failure and the assessment of the critical crack length needed for the onset of propagation (e.g. Gaume *et al.*, 2017, 2018b; Gaume and Reuter, 2017; Schweizer and Reuter, 2015; Reuter and Schweizer, 2018). In the field, the assessment of the likelihood of these two processes—failure initiation and onset of crack propagation—can be done through snow mechanical tests, which can provide useful information for avalanche forecasting. However, estimating the area of the avalanche release zone remains challenging due to incomplete understanding of the mechanical processes involved. At the moment, methods based mainly on terrain characteristics and snow depth maps (e.g. Veitinger *et al.*, 2016; Duvillier *et al.*, 2023) are used to predict potential avalanche release

areas. This method yields interesting results and seems promising for operational applications, but lacks mechanical ingredients to fully account for dynamic crack propagation and crack arrest.

Originally, some studies used a cellular automata method to focus on the influence of spatial heterogeneity of the weak layer strength on the slope stability (Faillettaz *et al.*, 2004; Fyffe and Zaiser, 2004; Kronholm and Birkeland, 2005). They showed that a complete failure of all cells was more likely to occur with a highly correlated spatial structure, compared to a spatial structure with random noise. These studies were the first to provide indication for the possible avalanche release size. The finite-element method (FEM) was also used to study the influence of the spatial heterogeneity of the weak layer on the avalanche release size. Gaume *et al.* (2015a) demonstrated with a FEM method that a weak layer heterogeneity could induce a slab tensile fracture that could potentially stop the propagation and release the slab. However, previously proposed cellular automata and FEM methods were unable to capture all mechanical processes involved during a dynamic crack propagation in a snow slab avalanche. Recently, snow avalanche research has shifted towards understanding dynamic crack propagation, which supposedly largely influences the avalanche size (Bergfeld *et al.*, 2023; Bobillier *et al.*, 2021, 2024a; Trottet *et al.*, 2022). Yet, so far, avalanche release size indicators accounting for the intricacies of dynamics crack propagation and arrest are still missing, urging for more research.

Crack propagation in dry snow slab avalanches was originally understood as a shear band propagation (mode II in fracture mechanics) within the weak layer (McClung, 1981; Gaume *et al.*, 2013; Puzrin and Germanovich, 2005; Gaume and Puzrin, 2021). However, this shear propagation model fails to reproduce crack propagation on low-angle terrain or observations of remotely triggered avalanches. Johnson (2000) observed a change in the weak layer thickness after fracture, which indicated that the weak layer collapsed during crack propagation. He proposed a theory in which crack propagation on low-angle terrain is driven by the collapse of the weak layer and subsequent bending of the slab, which led to the in-

troduction of a new snow mechanical test called the Propagation Saw Test (PST) (Gauthier and Jamieson, 2008). Heierli *et al.* (2008) proposed to adapt the so-called "*anticrack*" theory proposed in earthquake science for crack propagation in snow avalanche. This model represents a mode of crack propagation with closing crack faces under compression (mode -I), by opposition to opening crack faces under tension (mode I). Recently, more advanced analytical models for the onset of crack propagation in avalanche release were proposed including mixed-mode weak layer failure (Rosendahl and Weißgraeber, 2020; Benedetti *et al.*, 2019).

Over the past decade, various numerical simulation methods have been employed to investigate avalanche release mechanisms. Among these, the Discrete Element Method (DEM) with a bonded contact model (Gaume *et al.*, 2015b, 2017), the finite element method (FEM) (Habermann *et al.*, 2008; Reuter *et al.*, 2015b; Gaume *et al.*, 2018a; Podolskiy *et al.*, 2013) and the Material Point Method (MPM) with a new elasto-plastic law (Gaume *et al.*, 2018b, 2019; Trottet *et al.*, 2022) have been extensively utilized to simulate the initiation and dynamics of crack propagation. Drawing from these distinct methodologies and field observations, Bobillier *et al.* (2021, 2024a) and Trottet *et al.* (2022) documented a transition from sub-Rayleigh anticrack to supershear crack propagation during the release process. This finding was further supported by surprisingly large propagation speeds measured on avalanche videos (Hamre *et al.*, 2014; Simenhois *et al.*, 2023). The study of Trottet *et al.* (2022) now closes the debate on whether crack propagation is in shear mode or collapse-based anticrack mode, demonstrating that both crack propagation regimes are present in the release mechanism of a dry snow slab avalanche. On low-angle terrain or on slopes for short crack propagation distances (¡ 1-3 m), the propagation is driven by an anticrack mode in which the crack speed is below the shear wave speed of the slab (Siron *et al.*, 2023). On steep terrain, after propagating over a distance larger than the so-called "super critical length", the crack transitions from a sub-Rayleigh anticrack regime to a supershear propagation regime in which the crack speed is higher than the shear wave speed of the slab. These findings suggest that a pure shear model could be enough to simulate large-scale avalanche release processes. Hence, to reduce the computational cost of 3D DEM or MPM, Guillet *et al.* (2023) developed a depth-averaged

Material-Point-Method (DA-MPM), which simulates the supershear dynamic propagation on complex terrain in a very efficient manner.

The understanding of dynamic crack propagation is currently expanding, facilitated by enhanced measurements in the context of field PSTs (e.g. Bergfeld *et al.*, 2021), as well as physically-based modeling (Gaume *et al.*, 2019; Bobillier *et al.*, 2021). However, very few studies have focused on the conditions for the arrest of the crack and slab tensile failure during dynamic crack propagation (Bergfeld *et al.*, 2023; Gaume *et al.*, 2015a, 2019; Trottet *et al.*, 2022). More knowledge on slab tensile failure and crack arrest in a dynamic context is crucial to ultimately estimate the avalanche release size. Gaume *et al.* (2015a) made the assumption that the distance of the first slab tensile fracture could serve as an indicator for the size of the avalanche. However, their model did not explicitly represent the arrest mechanism, which could potentially be caused by a slab fracture. Gaume *et al.* (2019) demonstrated with the MPM method, two different types of slab fracture opening under tensile stress during dynamic crack propagation. The first type is related to the anticrack regime in which the bending of the slab induced an opening from the top of the slab. This type of slab fracture opening could be the cause of the crack arrests observed by Bergfeld *et al.* (2021). They observed several crack arrests on 10 m long flat PSTs, propagating in mode -I (closing crack), at a speed lower than the shear wave speed of the slab. They suggested that these crack arrests were caused by inherent properties of the slab/weak layer system. In the contrary, when the crack speed is relatively high in supershear regime driven by shear, Gaume *et al.* (2019) observed that the opening of the fracture started from the bottom of the slab. This bottom opening of the slab fracture was also observed in an avalanche crowns (Bair *et al.*, 2016; McClung, 2021) suggesting shear failure of the weak layer.

Furthermore, Trottet *et al.* (2022) provided insight into the effect of slab tensile fractures on crack propagation speed. They reported that slab fractures could prevent propagation from reaching the supershear speed if they occur before or during the transition between the anticrack and supershear regime. Multiple slab fractures could potentially slow the crack and

cause a crack arrest. They also showed that once the crack is in the supershear regime, i.e. at a crack speed higher than the shear wave speed of the slab, the slab fractures do not affect the crack speed any longer. This result could potentially indicate that supershear crack propagation could only be stopped if something changes in the system, either the topography or a heterogeneity in the snow properties. Further work is needed to test this hypothesis.

In accordance with the arguments put forth by Guillet *et al.* (2023) which draw from the findings of Trottet *et al.* (2022) regarding the supershear transition in avalanche release, and considering the significant computational expenses associated with 3D simulation tools like MPM or DEM, we have chosen to investigate crack arrest mechanisms during dynamic crack propagation using the depth-averaged Material Point Method (DA-MPM). This approach was recently introduced and verified by Guillet et al. (2023). DA-MPM enables rapid calculations over large areas, allowing to simulate these avalanche releases on realistic slopes within few minutes instead of days. This enables an investigation on potential drivers of crack arrest at the slope scale. Our work focuses on crack arrest that occurs when dynamic crack propagation reaches a steady state in the supershear regime, at a crack speed near the longitudinal elastic wave speed of the slab. Our work is based on the following hypothesis, which is based on the results of Trottet *et al.* (2022) and Simenhois and Birkeland (2014): we assume only two drivers can stop a crack propagation in a dynamic supershear mode: 1) an internal heterogeneity in the snowpack, 2) an external variation such as topography.

In this paper, we aim to quantify the effects of weak layer heterogeneity and slab fracture on crack arrest propensity. These effects are examined both independently and in combination. In Section 2, we introduce the numerical method employed, namely the Depth-Averaged Material Point Method (DA-MPM), along with the simulation setup. In subsequent sections, we present results for two scenarios: first, for purely elastic slabs, and second, for elasto-plastic slabs allowing for slab tensile fractures. We conduct a sensitivity analysis and propose a scaling law to elucidate crack arrest distances based on two dimensionless numbers. Furthermore, we present an application based on real weak layer heterogeneity derived

from field measurements and outline future directions, including the extension of our study to 3D simulations at the slope scale. Finally, in Section 5, we discuss the results and their implications, highlighting the model limitations and avenues for further research.

3.4 Methods

3.4.1 DAMPM

The findings of Trottet *et al.* (2022) support our choice to adopt a depth-averaged approach that solves the momentum and mass conservation equations. The main assumptions will be outlined in this section, however, for a more detailed presentation of the method, please refer to Guillet *et al.* (2023). The DA-MPM method is based on the classic shallow water assumption, i.e the flow thickness is much smaller than slope-parallel dimensions of the flow. It can be translated into our avalanche context as $h/L \ll 1$, where h is the slab height and L is the characteristic length of the avalanche. The material in this study is assumed to be incompressible, meaning that the density ρ is constant regardless of time, place, or position. The flow surface is stress free at the top of the slab, where $\boldsymbol{\sigma} h = z = \mathbf{0}$. It should be noted that the method can be easily adapted to a compressible form if the evolution of ρ is necessary. In contrast to classical MPM in which the continuum is discretized using particles, in DA-MPM, colums of height h are utilized (Fig.26). The depth-averaged equation of mass conservation is given by:

$$\frac{\partial h}{\partial t} + \frac{\partial (h\overline{v}_x)}{\partial x} + \frac{\partial (h\overline{v}_y)}{\partial y} = 0 \tag{3.1}$$

where $\overline{v}_x$ and $\overline{v}_y$ are the depth-averaged velocities at the integration point of the particle.

The last assumption is a plane stress assumption with $\sigma_{zy} = \sigma_{zx} = 0$. Basal forces are applied at the interface between the slab and the weak layer defined by:

$$\tau_{xz} := \sigma_{xz}|_{z=0}, \tau_{yz} := \sigma_{yz}|_{z=0} \tag{3.2}$$

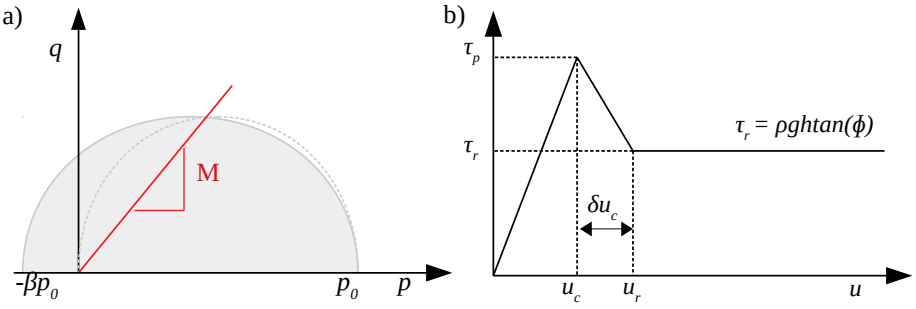

Figure 26 – a) Slab elasto-plastic model following a Modified Cam-Clay yield surface, with q representing the Von Mises equivalent stress, p the pressure, M the slope critical state line, p_0 the compressive strength, and the βp_0 the tensile strength. b) The weak-layer is defined as as quasi-brittle interface model with the peak shear stress τ_p at the critical displacement u_c, and the residual stress τ_r at the residual displacement u_r. The residual stress is defined as $\tau_r = \rho g h \tan\phi$ where ρ is the particle density, g is the gravitational acceleration, h the particle height and ϕ is the friction angle. The softening behavior is defined by the softening coefficient δ.

which give also $\sigma_{zz}|_{z=0} = \rho g_z h$ at the bottom of the slab column and $\overline{\sigma}_{zz} = \frac{1}{2} h \rho g_z$ at the integration point, located in the middle of the column. This allows us to have the depth-averaged non-conservative form of momentum conservation:

$$\rho h \frac{\overline{d}\overline{v}_x}{\overline{d}t} = \frac{\partial(h\overline{\sigma}_x x)}{\partial x} + \frac{\partial(h\overline{\sigma}_x y)}{\partial y} - \tau_{xz} + g_x \rho h. \tag{3.3}$$

$$\rho h \frac{\overline{d}\overline{v}_y}{\overline{d}t} = \frac{\partial(h\overline{\sigma}_y y)}{\partial y} + \frac{\partial(h\overline{\sigma}_x y)}{\partial x} - \tau_{yz} + g_y \rho h. \tag{3.4}$$

where the depth-averaged material derivative $\overline{d}/\overline{d}t$ is given by $\overline{d}/\overline{d}t = \partial/\partial t + \overline{v}_x \partial/\partial x + \overline{v}_y \partial/\partial y$.

The slab is represented with an elasto-plastic model following a Modified Cam-Clay yield surface γ in the $p - q$ space (Gaume *et al.*, 2019):

$$\gamma(p, q) = q^2(1 + 2\beta) + M^2(p + \beta p_0)(p - p_0) \tag{3.5}$$

where M is the cohesionless critical state line, β is the cohesion parameter that quantifies the ratio between the tensile and compressive resistance and p_0 is the consolidation pressure that affects the size of the yield surface. With M and β constant, respectively, at 0.3 and 1.2 (Guillet *et al.*, 2023), we related the uniaxial slab tensile strength σ_t to p_0 according to:

$$p_0 = \frac{-(1-\beta)p_t}{2\beta} + \sqrt{\left(\frac{(\beta+1)p_t}{2\beta}\right)^2 + \left(\frac{q_t}{M}\right)^2 \left(\frac{(1+2\beta}{\beta}\right)} \tag{3.6}$$

where $p_t = \frac{\sqrt{3}\sigma_t}{2}$ and $q_t = -\frac{\sigma_t}{2}$ considering the plane stress hypothesis (see Appendix B). The weak layer is conceptualized as a quasi-brittle interface that exhibits a softening behavior when the displacement u reaches the critical values u_c, corresponding to the shear stress reaches τ_p (Figure 26-b). The stress τ increases with the displacement u until τ_p. The associated stiffness K_{wl} can be related to the shear modulus of the weak layer G_{wl} and weak layer thickness D_{wl} according to $K_{wl} = G_{wl}/D_{wl}$. The softening continues until the displacement reaches its residual values u_r , after which the stress levels-off at a residual frictional value τ_r. The residual friction is given by the slab density ρ, the slab thickness h, the gravity acceleration g and friction angle of snow $\phi = 27°$. The residual displacement u_r is given by $u_r = u_c + \delta u_c$. The softening behavior is defined by the softening coefficient δ, so that a high δ will have a important softening behavior in the weak layer (a value of $\delta = 0$ corresponds to a perfectly brittle behavior).

We used DA-MPM to simulate PSTs which are 100 m long and 30 cm wide, with a dx set to 0.02 m on with a slope angle $\psi = 35°$. The initial column height h (slab thickness) was set to 0.5 m and the slab density was set to 250 kg m^{-3}. As the slab elastic modulus E crucially impacts crack propagation dynamics, it will be varied within a realistic range and its effect on the results will be analyzed in details. The goal of this study is to test our research hypothesis that a internal snow variation could lead to a crack arrest in supershear regime. The internal snow variation was represented by the shear strength of the weak layer τ_p, with a constant and positive shear strength gradient θ. A propagation towards stronger zones of the weak layer (increase of shear strength) appears appropriate in a real avalanche

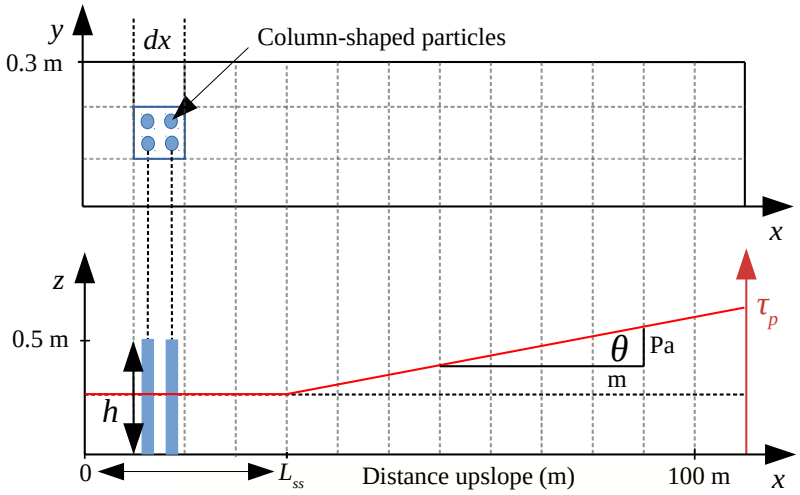

Figure 27 – Geometry of the PST's simulation in (x, y) (a, top view) and (x, z) (b, side view) planes. The particle height h is constant at 0.5 m. The simulations with the weak layer strength variation (red) were defined with the shear strength gradient θ is defining the shear strength τ_p beyond L_{ss} of the PST. The crack arrest position L_{ca} is where the crack speed has returned to zero. The crack arrest length A_{ca} is defined as $L_{ca} - L_{ss}$.

context because the fracture initiation induced by a trigger will typically start within weaker zones of the snowpack. For these simulations, all snow properties (h, ρ, E, σ_t) were constant across the PST except for τ_p, which was constant at 1000 Pa over a certain distance called the steady-state length L_{ss} and then gradually increases according to a shear strength gradient θ in Pa m^{-1} (Figure 27). The steady-state length L_{ss} is the distance that ensures the crack propagation speed reaches a steady-state regime. To simulate a PST, we numerically removed the cohesion of the weak layer, and applied the residual friction τ_r (Figure 26-b). The removal of the weak layer at the bottom of the PST will induce stress concentration at the crack tip, until it reached the stress necessary for the onset of crack propagation. Then, the crack dynamically propagates as a shear band up-slope until a crack arrest was recorded or until the crack propagated across the entire PST without arrest. The crack speed was normalized by the the shear wave speed of the slab given by $c_s = \sqrt{\frac{G}{\rho}}$, with G being the slab shear modulus and ρ the slab density. The slab shear modulus is defined by $G = \frac{E}{2(1+\nu)}$, with ν being the Poisson's ratio set to 0.3 in all simulations.

Four different types of simulations were performed in this study that will be presented in distinct result sections. First, simulations will be performed to investigate an the effect of crack speed on slab tensile stress. For these simulations, different controlled crack speed are used to investigate the dynamic tensile stress build up in the slab, and compared to the quasi-static tensile stress, given by $\sigma_{xx}^{qs} = \rho g a \sin(\psi)(1 - \frac{\tan(\phi)}{\tan(\psi)})$, where a is the crack length growing during the simulation. These PSTs were conducted with a pure elastic slab and an infinite shear strength, making self-sustained dynamic crack propagation not possible. Hence, a "controlled" crack propagation was enforced by numerically removing the cohesion of the weak layer at different and constant speed values. This controlled procedure enabled us to illustrate the effect of crack speed on dynamic tensile stress in the slab.

Second, a sensitivity analysis was conducted with a pure elastic slab. A pure-elastic slab, although non-realistic, will allow us to test the following parameters in a simpler case study to isolate important mechanical drivers: the steady-state length L_{ss}, the softening coefficient δ, the shear strength gradient θ, the weak layer shear modulus G_{wl}, and the slab elastic modulus E.

Third, the PST analysis was made with an elasto-plastic slab. This allowed us to study the effect of slab fracture(s) on the propagation speed and possibly the arrest of the crack. This analysis involves one additional parameter: the slab tensile strength σ_t. In addition, we performed similar simulations with *in-situ* shear strength values and gradients obtained based on field measurements conducted by Meloche *et al.* (2024). Using a high-resolution penetrometer named SnowMicroPen (Johnson and Schneebeli, 1999), they mapped the shear strength of the weak layer across various avalanche-prone slopes.

The last type of simulation presented in this research represents an application to predict the avalanche release size at the slope scale over three-dimensional terrain with a spatial variability of the weak layer strength. The slope scale simulation was performed on two generic slopes with dimensions 50 m (down-slope) by 60 m (cross-slope) for the first slope and 50 m (down-slope) by 100 m (cross-slope) for the second slope, aimed at studying cross-

Table 5 – Summary of all parameters for the four different types of simulations performed in Depth-averaged Material Point Method DAMPM.

Parameters	PST "controlled" speed	Pure elastic slab	Elasto-plastic slab	Full slope scale
Column/slab height h	0.5 m	0.5 m	0.5 m	0.5 m
Column/slab density ρ	250 kg m^{-3}	250 kg m^{-3}	250 kg m^{-3}	250 kg m^{-3}
Weak layer shear strength τ_0	∞ Pa	1000 Pa	1000 Pa	mean 1000 Pa
Weak layer shear modulus G_{wl}	0.2 MPa	0.1...0.3 MPa	0.2 MPa	0.2 MPa
Weak layer thickness D_{wl}	0.04 m	0.04 m	0.04 m	0.04 m
Poisson's ratio ν	0.3	0.3	0.3	0.3
Slope angle ψ	35°	35°	35°	max 35°
Internal snow friction angle ϕ	27°	27°	27°	27°
PST sawing speed	0.01...1.6 c_s	6 m s^{-1} = 0.07 c_s	6 m s^{-1} = 0.07 c_s	6 m s^{-1} = 0.07 c_s
Steady-state length L_{ss}	NA	5...30 m	10-20-30 m	NA
Softening coefficient δ	0	0...4	0-1	1
Shear strength gradient θ	NA	100...10 000 Pa m^{-1}	10...1000 Pa m^{-1}	20 Pa m^{-1}*
Tensile strength σ_t	∞ kPa	∞ kPa	2..10 kPa	4 kPa
Slab elastic modulus E	4 MPa	2-4-6 MPa	2-4-6 MPa	4 MPa

*GRF Gaussian Random field was used to generate 2D surface gradient of shear strength gradient θ.

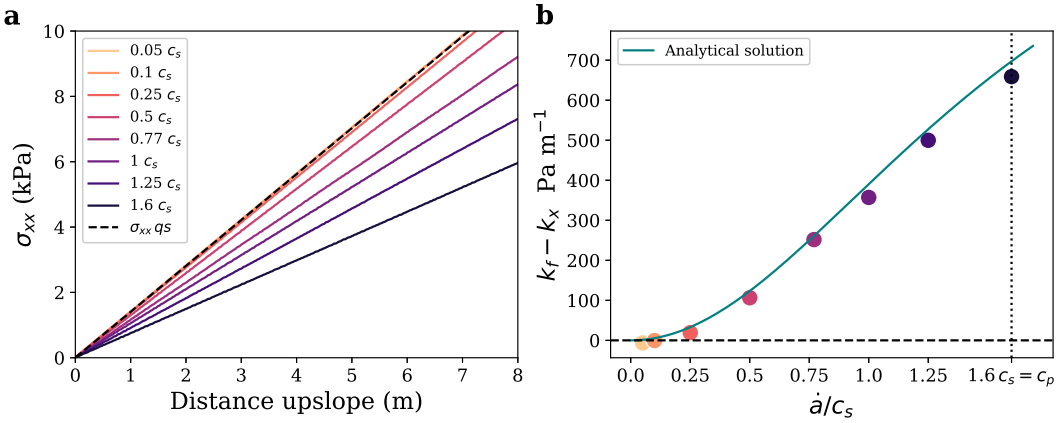

Figure 28 – a) Tensile stress σ_{xx} as a function of the distance upslope in a PST simulation with infinite weak layer shear strength in a controlled sawing procedure. The numerical sawing is performed by removing weak layer cohesion at different speeds, along the upslope direction. The theoretical quasi-static tensile stress σ_{xx}^{qs} is also plotted for reference. b) Difference between the quasi-static tensile stress gradient k_f (Eq. (7)), and the dynamic tensile stress gradient k_x (Eq. (8)) versus the normalized sawing speed $\dot{a}/c_s$, until $c_p \approx 1.6c_s$.

slope propagation. The generic slope consists of a concave zone at the slope toe which reaches a maximum slope angle $\psi = 35°$, followed by a convex shape at the top of the slope. A Gaussian random field GRF approach was used to generate the shear strength heterogeneity with similar strength gradients as those measured experimentally. Table 5 lists all parameter values used for the four different types of simulation, including the range values tested of each parameters. Finally, we define A_{ca}, the crack arrest length which is computed as $A_{ca} = L_{ca} - L_{ss}$, where is L_{ca} is the x-position of the crack arrest in the coordinate system defined in Figure 27.

3.5 Results

3.5.1 Dynamic effects on slab tensile stress

An in-depth analysis of our simulations revealed that the tensile stress was significantly lower than the quasi-static tensile stress given by $\sigma_{xx}^{qs} = a\rho g \sin(\psi)\left(1 - \frac{\tan(\phi)}{\tan(\psi)}\right)$, where a is

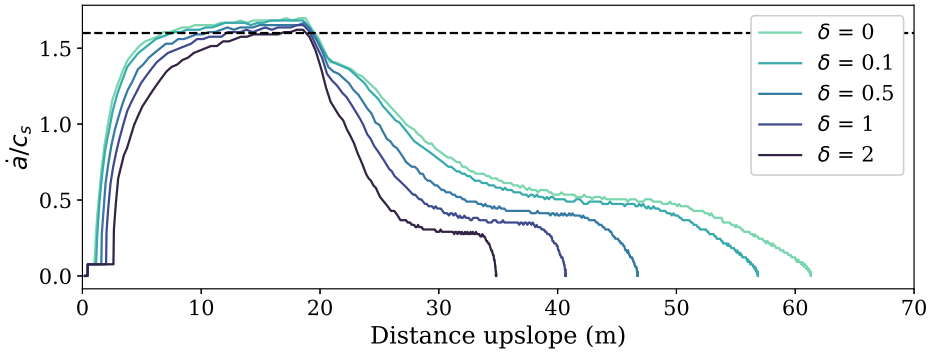

Figure 29 – Crack speed $\dot{a}$ along the PST, normalised by the slab shear wave speed $c_s = \sqrt{G/\rho}$. The colors represent different simulations with specific softening coefficients δ (0 = brittle). Crack arrest is observed when the crack speed goes back to zero. A horizontal dashed line is set at 1.6 $c_s \approx \sqrt{E'/\rho}$, which is the supershear speed (Trottet *et al.*, 2022).

crack length increasing during the simulation. We investigated this reduction in tensile stress induced by dynamic effects using a PST setup with "controlled" speed (i.e. the crack is artificially created with a constant speed). This controlled procedure enabled us to quantify the effect crack speed on slab tensile stress. Figure 28-a shows the tensile stress as a function of the distance upslope along the PST. The black dotted line represents the quasi-static tensile stress. As the speed increases, the tensile stress deviates from the quasi-static formulation. Figure 28-b demonstrates the difference between the quasi-static tensile stress gradient k_f and the dynamic tensile stress gradient k_x for different normalized speed values $\dot{a}/c_s$. The increase of the tensile stress gradient difference $k_f - k_x$ with crack speed is well reproduced by a newly developed analytical expression (Figure 28-b) given by Eqs. (7) and (8):

$$k_f = \rho g \sin(\psi)\left(1 - \frac{\tan(\phi)}{\tan(\psi)}\right) \tag{3.7}$$

and,

$$k_x = \frac{c_p^2 k_f}{c_p^2 + \dot{a}^2} \tag{3.8}$$

where $c_p = \sqrt{\frac{E'}{\rho}}$ represents the elastic wave speed of the slab, $E' = E/(1-\nu^2)$, and $\nu = 0.3$ is the Poisson's ratio. The derivation of the analytical solution is detailed in Appendix A.

3.5.2 Simulations with Elastic Slabs

The first simulations were performed with a pure elastic slab to isolate important drivers with potentially five parameters that could affect the crack arrest length. First, we analyze the effect of the softening coefficient δ which relates to the energy dissipated during fracture. Figure 29 shows five PST simulations with different softening coefficients δ with the same shear strength gradient. First, the crack speed reached 1.6 c_s, within the steady-state length (L_{ss} = 20 m). Different PST simulations exhibited the same behavior within L_{ss}, reaching supershear speed at 1.6 c_s, except that the simulations with the lower δ values (pure brittle) reached 1.6c_s earlier than the simulations with higher δ (Figure 29). Beyond L_{ss}, the crack speed was significantly influenced by the shear strength gradient (θ = 500 Pa m^{-1}), eventually causing the crack speed to return to zero. All PST simulations displayed a rapid deceleration in the crack speed, followed by a period of rather constant crack speed, before returning to zero (Figure 29). This sustained constant crack speed observed at the end of crack propagation was a result of the combined effects of deceleration at the crack tip and the pure elastic slab, generating residual downward stress leading to a ”late push” in the crack propagation. As will be seen later, this finding may not applicable to rather soft elasto-plastic snow slabs for which a slab fracture would have occurred before. Finally, the effect of the softening coefficient was demonstrated with the pure brittle simulation (δ = 0) with the longest crack arrest length A_{ca} of 62 m, compared to a δ of two with almost half the length at 35 m (Figure 29). This finding demonstrated how increasing weak layer fracture energy resulted in shorter A_{ca}.

The steady-state length L_{ss} is the second parameter that could potentially affect the crack arrest length. Several PST simulations with different values of L_{ss} demonstrated a linear effect of L_{ss} over A_{ca} (Figure 30). Indeed, slabs with cracks which propagated over longer distances L_{ss} at a speed around 1.6 c_s stored more elastic energy than those with lower L_{ss} values. Higher stored elastic energy also implies higher energy to dissipate to stop crack propagation thus naturally leading to a higher A_{ca} value. Another parameter that obviously

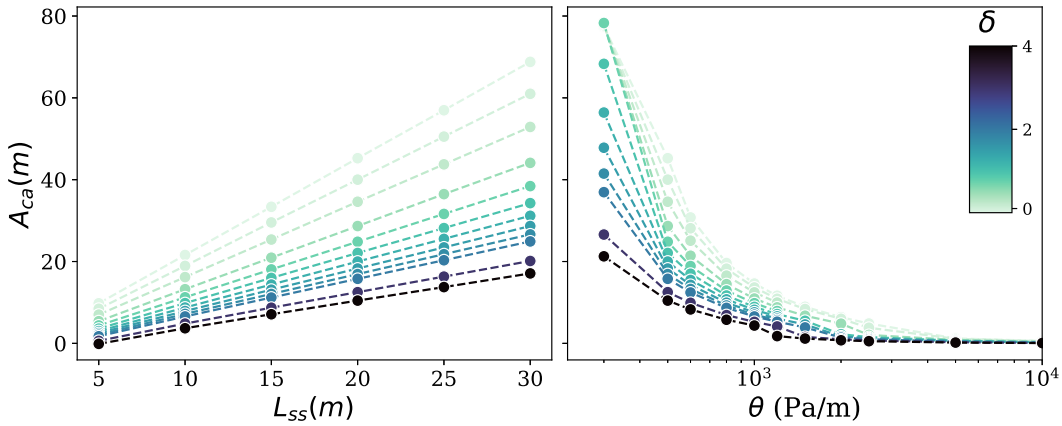

Figure 30 – Crack arrest length A_{ca} from the PST simulations in relation to a) the super shear length L_{ss} with different softening coefficients δ, and a constant $\theta = 500$ Pa m^{-1} and to b) the shear strength gradient θ with different softening coefficient δ, and a constant $L_{ss} = 20m$.

significantly affects the crack arrest length is the shear strength gradient θ. His effect on A_{ca} is nonlinear as A_{ca} rapidly decreases as θ increased, especially around 500 Pa m^{-1} (Figure 30). When the shear strength gradient is around 5000 Pa m^{-1}, the gradient is too large, causing crack arrest after L_{ss}. Figure 30 also illustrates the influence of the softening coefficient δ on the crack arrest length, in combination with the effects of L_{ss} and θ.

The last two parameters that were tested with a pure elastic slab are the slab elastic modulus E and the weak layer shear modulus G_{wl}. These two parameters have a significant, yet opposite impact on the crack arrest length A_{ca}. Indeed, both parameters affect the characteristic elastic length of the system $\Lambda = \sqrt{\frac{EhD_{wl}}{(1-\nu^2)G_{wl}}}$. If the slab elastic modulus of the slab increases, Λ also increases, thus reducing stress concentrations at the crack tip, resulting in a reduction in crack arrest length (Figure 31-a). On the other hand, if the the shear modulus of the weak layer increases, Λ decreases resulting in higher stress concentrations and thus a higher value of A_{ca}.

Following a comprehensive examination of the simulation data, a scaling law relating the dimensionless crack arrest length A_{ca}/L_{ss} to the dimensionless variable $\tau_g/(\theta\Lambda\sqrt{1+\delta})$ was found (Figure 32a). This number basically compares a driving contribution, namely the

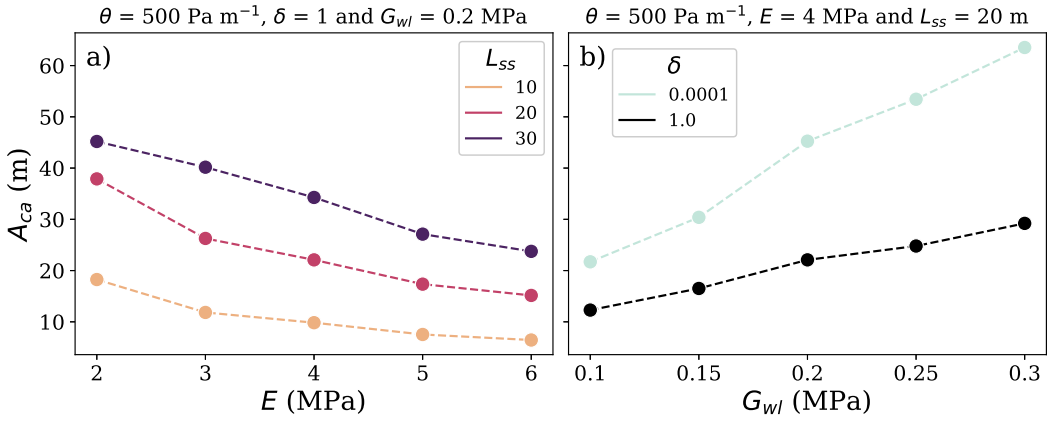

Figure 31 – Crack arrest length A_{ca} from the PST simulations in relation to a) different elastic modulus of the slab E with different steady-state length L_{ss}, a constant $\theta = 500$ Pa m^{-1}, softening coefficient $\delta = 1$ and a shear modulus $G_{wl} = 0.2$ MPa and in relation to b) the weak layer shear modulus G_{wl}, with different softening coefficient δ, and a constant $L_{ss} = 20$ m, shear strength gradient $\theta = 500$ Pa m^{-1}, and slab elastic modulus $E = 4$ MPa.

shear stress τ_g to a resisting term, namely the shear strength increment $\theta\Lambda$ over a distance Λ (characterizing elastic stress concentrations) multiplied by $\sqrt{1+\delta}$ (characterizing the softening distance in the weak layer mechanical model). On the basis of this data collapse and linear character of the relationship in log-scale, we can provide the following empirically-based power-law equation:

$$\frac{A_{ca}}{L_{ss}} \propto \left(\frac{\tau_g}{\theta\Lambda\sqrt{1+\delta}}\right)^{3/2} \tag{3.9}$$

3.5.3 Simulations with Elasto-Plastic slabs

The PST simulations presented in this section are performed with an elasto-plastic snow slab, allowing for slab tensile fractures to occur and potentially affect the propagation and cause the arrest of the crack. Simulations performed with a very low shear strength gradient, at 10 Pa m^{-1}, led to full propagation with slab tensile fractures that had no effect on the crack speed. Shear strength gradients of more than 20 Pa m^{-1} were needed to obtain crack arrest within the PST length. In this cases, the crack arrest lengths were significantly lower

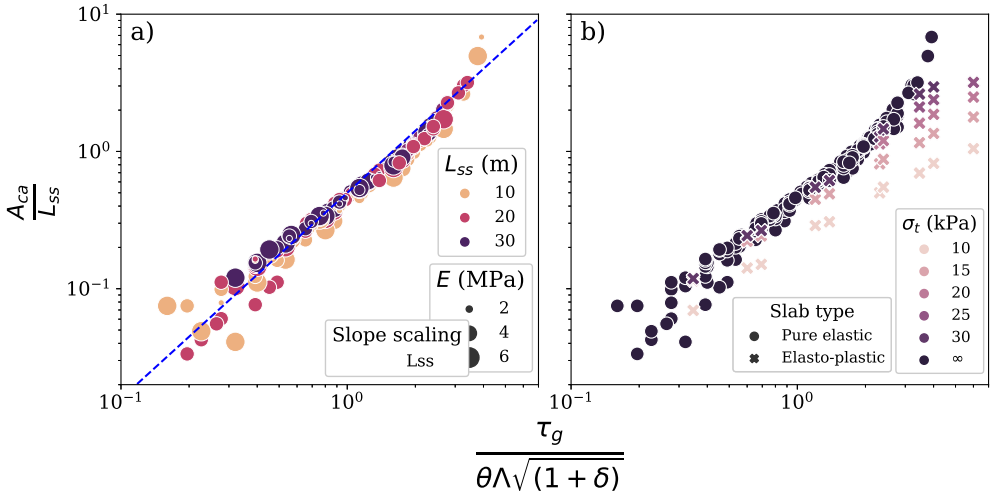

Figure 32 – Crack arrest length A_{ca} (normalized with L_{ss}) from all our PST pure elastic slab simulations in relation to the dimensionless number $\tau_g/(\theta\Lambda\sqrt{1+\delta})$. The PST simulations presented in a) were all pure elastic slab simulations. The 2:3 line is plotted in blue as reference. In b) the same PST simulations as in a) are shown in dark blue but with additional PST elasto-platic simulations with different values of σ_t. The data in this plot includes the results from all pure elastic simulations with the following parameters that were varied: the shear strength gradient θ, the weak layer shear modulus G_{wl}, the steady-state length L_{ss}, elastic modulus of the slab E, and the softening coefficient δ.

than those performed with pure elastic slabs for the same weak layer shear strength gradient. Figure 33 illustrates two PST simulations that resulted in different types of crack arrest. Supplementary videos are also provided to better grasp the spatio-temporal evolution of the stress states and crack dynamics. In Figure 33-a, the first type is achieved with a relatively low θ (30 Pa m^{-1}), and was characterized by four slab tensile fractures needed to stop crack propagation. Initially, the first slab fracture minimally affected the crack speed as the crack tip just passed 30 m (20 m = L_{ss}). However, subsequent slab fractures increasingly affected the crack speed until the last fracture completely stopped the propagation at around 94 m. Figure 33-b shows a PST simulation with a higher shear strength gradient θ of 150 Pa m^{-1}, yet with the same tensile strength σ_t as in Figure 33-a. The higher value of θ caused the crack speed to decelerate significantly after the first slab fracture. In this case, only one slab tensile fracture was needed to stop crack propagation. Both the shear strength gradient θ and slab

tensile fracture σ_t contribute to the arrest of the crack.

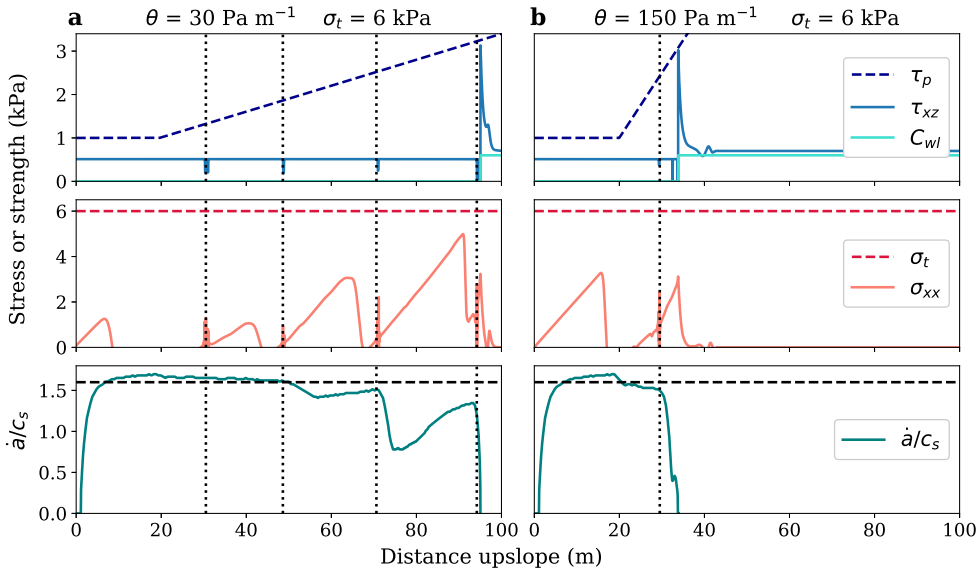

Figure 33 – Two PST simulations with elasto-plastic snow slabs. The top subplots show the shear stress τ_{xz} and strength τ_p as well as the weak layer cohesion $C_{wl} = \tau_p - \tau_r$. The middle subplots show the tensile stress σ_{xx} and strength σ_t. The bottom subplots show the crack speed $\dot{a}$ normalised by the shear wave speed of the slab c_s. A horizontal dashed line is set at 1.6 c_s for the crack speed. Vertical dotted lines represent locations where slab tensile fractures occurred along the PST. a) PST simulation with shear strength gradient θ = 30 Pa m^{-1} with multiple tensile fracture (dotted lines) causing a crack arrest at 94 m. b) PST simulations with θ at 150 Pa m^{-1} with only one tensile fracture causing a crack arrest at 34 m. In both simulation, the tensile strength σ_t was set to 6000 Pa, and the softening coefficient δ to 0 (brittle).

Figure 34 presents a sensitivity analysis for four parameters in the case with an elasto-plastic slab: shear strength gradient θ, the tensile strength σ_t, the elastic modulus E and the steady-state length L_{ss}. First, similar to the pure elastic case, we report a significant decrease of the crack arrest length A_{ca} with increasing shear strength gradient, as expected. However, compared to the pure elastic slab case, values of θ about an order of magnitude lower were required with an elasto-plastic slab to obtain a similar crack arrest length. This result illustrates the complex interplay between slab tensile fractures and the crack dynamics in the weak layer on crack arrest propensity.

In addition, the tensile strength σ_t also had a significant influence on crack arrest. For a given θ, a higher σ_t led to slab tensile fractures occurring further upslope in the PST, resulting in longer A_{ca} (Figure 34-a). The slab's elastic modulus E also influences A_{ca}, where lower E values correspond to larger A_{ca} values for identical θ values. The influence of the steady-state length L_{ss} on A_{ca} depends on the value of θ. For large θ values, we report a decrease of A_{ca} with increasing L_{ss} (Figure 34-c). However, for lower values of θ, it appears that the effect of L_{ss} becomes more moderate and tends to vanish with decreasing values of θ.

Furthermore, this elasto-plastic analysis reveals two distinct types of crack arrest (Figure 34): crack with single or multiple slab tensile fractures. Multiple slab tensile fractures (circles in Figure 34), often called "en-echelon" fractures in the literature (Gauthier and Jamieson, 2016), occurred within the lower range of θ. This regime of multiple fractures is also affected by several parameters such as σ_t, E and L_{ss} (Figure 34). For larger values of the shear strength gradient θ, typically above 100 Pa/m, only a single slab tensile fracture was required to arrest the crack (crosses in Figure 34). Finally, note that simulations with θ below 20 Pa/m were removed from this analysis because the crack in the weak layer fully propagated throughout the entire PST length, without arrest, even with multiple slab tensile fractures.

Numerous simulations were performed with various parameters to better understand the mechanisms driving crack arrest during snow slab avalanche release. Here, we simulated PSTs with different values of L_{ss}, E, σ_t, two different values of δ (perfectly brittle weak layer, i.e. $\delta = 0$ and with a non-zero softening length i.e. $\delta = 1$). On the basis of the large amount of simulation data generated, a second dimensional analysis was performed. The crack arrest length was normalized by the quasi-static tensile length $L_t = \sigma_t/(\rho g \sin\psi(1 - \frac{\tan\phi}{\tan\psi}))$. This normalized crack arrest length A_{ca}/L_t was plotted against the dimensionless number $\left(\frac{\tau_g}{\theta\Lambda\sqrt{1+\delta}}\right)\sqrt{\left(\frac{\sigma_t}{\tau_g}\right)}$. The left side of this number is the same as in the elastic scaling, and characterizes the ratio between the driving forces, namely the shear stress τ_g to a term characterizing the resisting forces, and related to θ, Λ and δ. The right side of the term

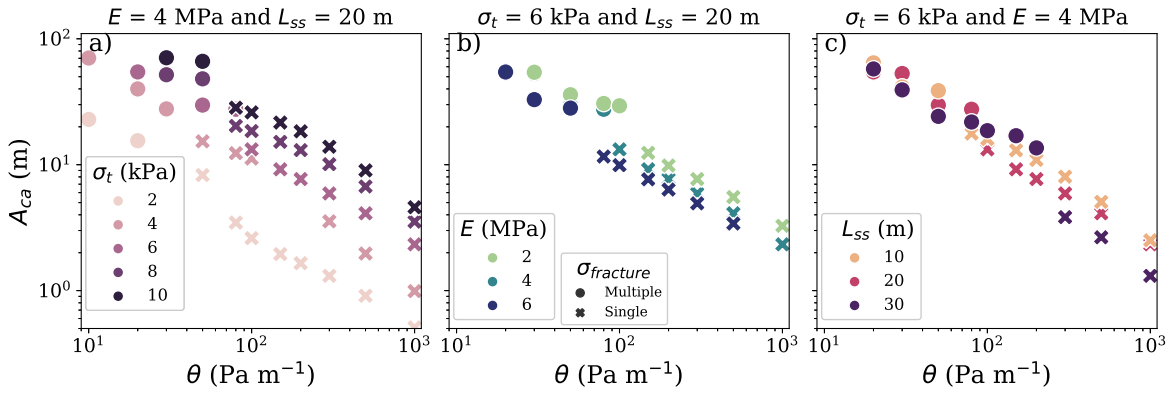

Figure 34 – Crack arrest length A_{ca} obtained from PST simulations as a function of the shear strength gradient θ, and for different a) tensile strengths σ_t (E = 4 MPa and L_{ss} = 20 m), b) elastic modulus values E (σ_t = 6 kPa and L_{ss} = 20 m), and c) steady-state lengths L_{ss} (σ_t = 6 kPa and E = 4 MPa). These PST simulations were done with a softening coefficient δ of 1. The symbols represent cases in which there was only one slab tensile fracture (cross) needed to stop the crack and in which multiple slab fracture were needed (circles).

compares the slab tensile strength σ_t to the slope parallel shear stress τ_g. A low σ_t/τ_g ratio implies a low crack arrest length A_{ca}. We report in Figure 35-a the result of this scaling analysis showing in log-scale a linear data collapse, thus suggesting a power-law relationship of the following form:

$$\frac{A_{ca}}{L_t} \propto \left(\frac{\tau_g}{\theta\Lambda\sqrt{1+\delta}}\right)\sqrt{\left(\frac{\sigma_t}{\tau_g}\right)} \tag{3.10}$$

Note that simulations with large values of tensile strength in which the arrest of the crack occurred without slab tensile fracture (arrest purely due to weak layer strength variations) were added to Figure 35-b. These data points deviate significantly from the previously reported data collapse. Likewise, in Figure 32-b, we introduced additional data points with slab fractures atop the scaling law established for an elastic slab. Once more, it appears that distinct mechanisms are in action, with varying factors influencing arrest in cases with and without slab fractures, as these additional data points fall outside the range of the data collapse out of the data collapse.

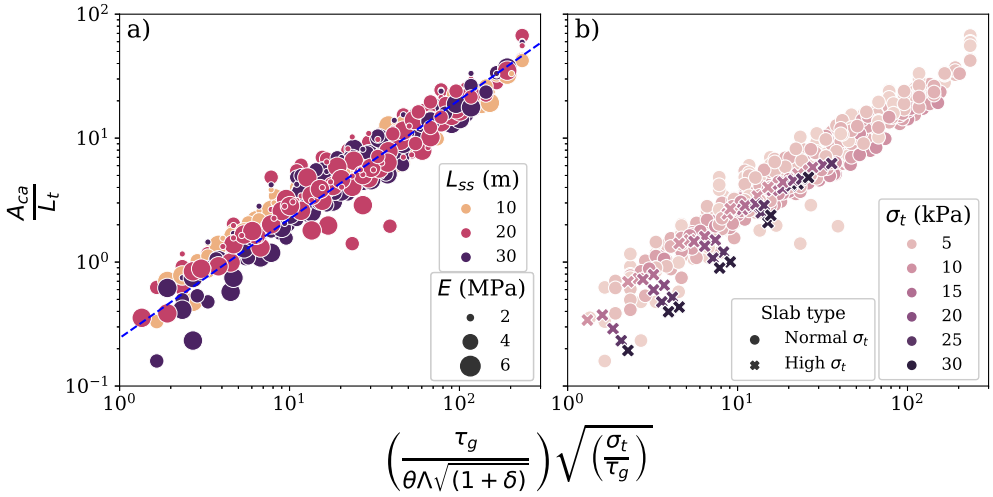

Figure 35 – Crack arrest length A_{ca} (normalized with $L_t = \sigma_t/(\rho g \sin\psi(1-\frac{\tan\phi}{\tan\psi}))$) from all our PST elasto-plastic-simulations in relation to the product between two dimensionless numbers. The scaling takes into account all the parameters tested in this study, which are the shear strength gradient θ, the tensile strength σ_t, the steady-state length L_{ss}, elastic modulus of the slab E, and the softening coefficient δ. a) PST elasto-plastic simulations with realistic values of σ_t with respect to snow, with a 1:1 slope line in blue. b) PST elasto-plastic simulations with added simulations with very high σ_t values, that demonstrated a transition regime from our elasto-plastic scaling to our pure elastic scaling.

3.5.4 Application to a real case with shear strength gradient θ measured *in-situ*

The values of θ used in the previous elasto-plastic simulations were selected in order to obtain crack arrest within our 100 m PST length. In this section, instead, model parameters are input on the basis of field measurements. Meloche *et al.* (2024) performed *in-situ* measurements of snow mechanical properties in order to derive snow strength and stability maps at the slope scale. We sampled their weak layer shear strength maps in the slope parallel direction from a weaker area to the top of the slope to obtain a shear strength gradient. Figures 36-a and 37-a show the sample location of the gradient (red rectangles) in two different study sites. We then interpolated the *in-situ* gradient in order to get a longer distance that will match our 100 m PST length. We applied these interpolated gradient after a steady-state length of 20 m to obtain the same elasto-plastic PST simulation set-up but with the *in-situ*

gradient (Figures 36-c and 37-c). The first *in situ* θ value was obtained at a forested site called Jim Bay corner JBC, and exhibited a linear gradient of 15 Pa m^{-1}. The crack speed from the simulation with the JBC gradient is shown in Figure 36-d, demonstrating that four slab fractures (vertical dotted lines) were needed to stop the crack propagation. This *in-situ* gradient from JBC is rather small and is located in the lower range of the θ values tested in

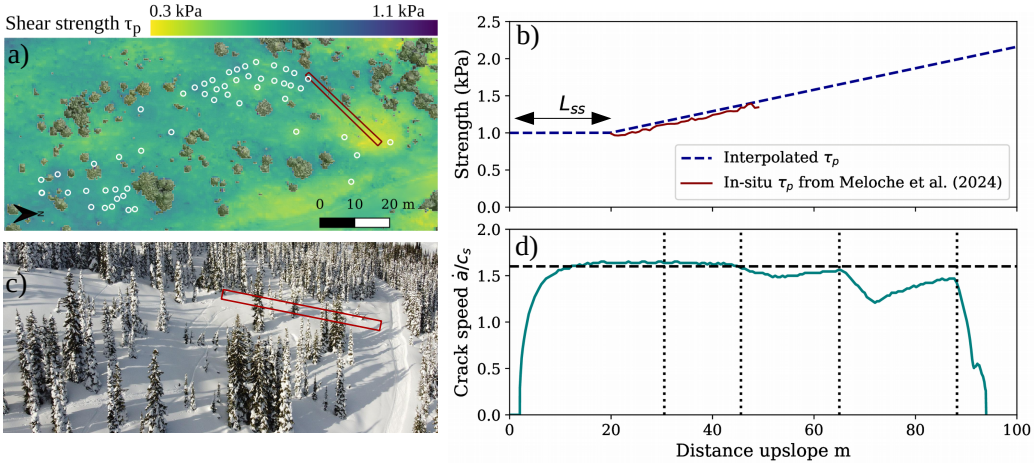

Figure 36 – PST simulation based on *in-situ* measurement of shear strength τ_p and shear strength gradient θ according to measurements made by Meloche *et al.* (2024) at a forested site Jim Bay Corner. The other parameters were the same as for the elasto-plastic simulations described in Table 5, with $L_{ss} = 20$ m, $E = 4$ MPa, $\sigma_t = 6$ kPa and $\delta = 1$. a) Shear strength map of Meloche *et al.* (2024) at the Jim Bay corner, with the sample location in the red rectangle. b) *In-situ* shear strength τ_p fitted at 1 kPa with the interpolated gradient θ, note that the shear strength values were fitted to start at 1 kPa in order to match our simulation parameters. c) Aerial photography of the site from UAV imagery. d) Crack speed $\dot{a}$ normalized by c_s from the simulation with slab tensile fractures (vertical dotted lines).

The second *in-situ* shear strength was sampled in a wind-affected alpine site from Meloche *et al.* (2024). The shear strength map had more important variations as well as larger maximum shear strength values compared to the first site. This second site exhibited a non-linear gradient, and a power-law was fitted to these values in order to apply the nonlinear

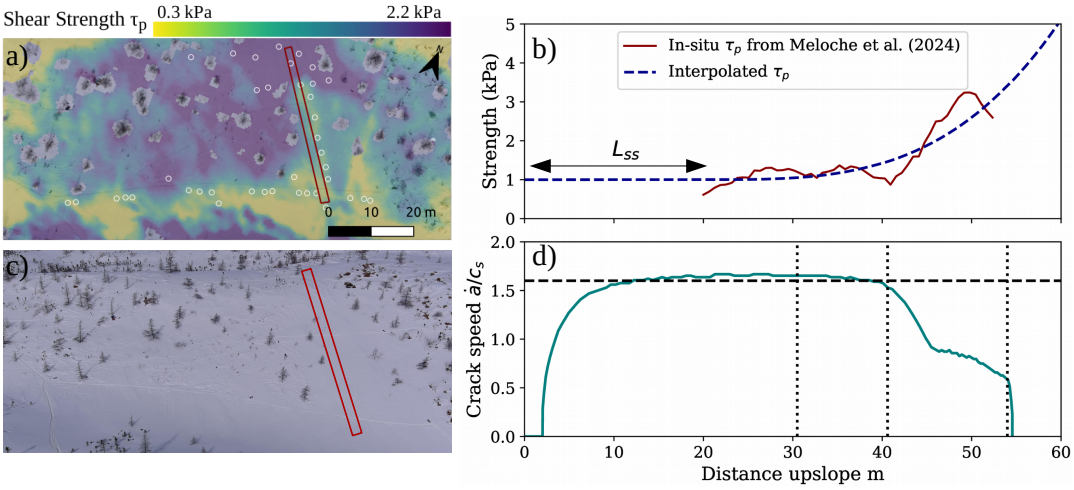

Figure 37 – PST simulation based on *in-situ* measurement of shear strength τ_p and shear strength gradient θ according to measurements made by Meloche *et al.* (2024) at an alpine site called Arête de Roc. The other parameters were the same as for the elasto-plastic simulations described in Table 5, with $L_{ss} = 20$ m, $E = 4$ MPa, $\sigma_t = 6$ kPa and $\delta = 1$. a) Shear strength map of Meloche *et al.* (2024) at the Arête de Roc, with the sample location in the red rectangle. b) *In-situ* shear strength τ_p fitted at 1000 Pa with the interpolated gradient θ, note that the shear strength values were fitted to start at 1000 Pa in order to match our simulation parameters. c) Aerial photography of the site from UAV imagery. d) Crack speed $\dot{a}$ normalized over c_s from the simulation with slab tensile fractures (vertical dotted lines).

gradient to match our longer PST (Figure 37-b). This simulation needed three slab fractures in order to stop the propagation. The first slab fracture did not affect the propagation in the weak layer. However, the second fracture, which occurred at the same location where the gradient is starting to increase rapidly, significantly slowed down the crack speed below c_s at around 40 m. A third slab fracture was needed to completely stop the crack propagation at 55 m. This nonlinear gradient observed at the alpine site was much larger than that obtained in the previous forested site, thus leading to a shorter crack arrest distance of around 55 m.

3.5.5 Slope scale analysis on three-dimensional terrain

The last result section is to explore the slope scale crack propagation with a weak layer heterogeneity in both slope parallel and the cross-slope direction. Figure 38-a demonstrates the applicability of the model on a fictional slope of 50 m by 60 m wide. Using a Gaussian Random Field approach (GRF), a 2D natural variability was generated, showing a shear strength gradient of 20 Pa m^{-1}, with an increase of around 400 Pa over 20 m up-slope (Figure 38-a). We initiated a crack at the bottom of the slope in the weak zone (black star) which propagated up-slope and stopped near the upper and stronger part of the slope. The DA-MPM column height was used to visualize slab tensile fractures in blue ($h < 0.49$), and the compressive fractures within the slab in red ($h > 0.51$). The most important slab tensile failure in blue represents the so-called avalanche crown where the crack propagation stopped. In contrast, the most important area in red (compressive failure) represents the so-called stauchwall of the avalanche. The crack propagation also stopped in the cross-slope direction at the right corner of the slope. Figure 38-a shows that crack propagation stopped between 40-50 m, approximately the same values of A_{ca} that were obtained in our PST experiment for the same value of θ (Figure 34). However, the crown is also starting at the beginning of the artificial convex roll where the slope angle is starting to reduce. The arrest of the crack might be caused by a combination of the increase in shear strength but also by the decrease in slope angle. Furthermore, Figure 38-b is showing a crack propagation in the cross-slope direction with a weak layer heterogeneity mostly oriented in the cross-slope direction. The initiation was at the top right corner of the slope (black star), and it propagated in the cross and down slope direction until the middle of the slope where the shear strength locally increases. The arrest in the cross-slope direction can only be related to the heterogeneity of the weak layer because the slope angle is constant in that part of the slope. However, it is known that the crack propagation speed in the cross-slope direction is lower than the downslope propagation speed, and is approximately around the shear wave speed of the slab c_s (Guillet *et al.*, 2023; Trottet *et al.*, 2022; Simenhois *et al.*, 2023; Gaume *et al.*, 2019). This slower speed in crack

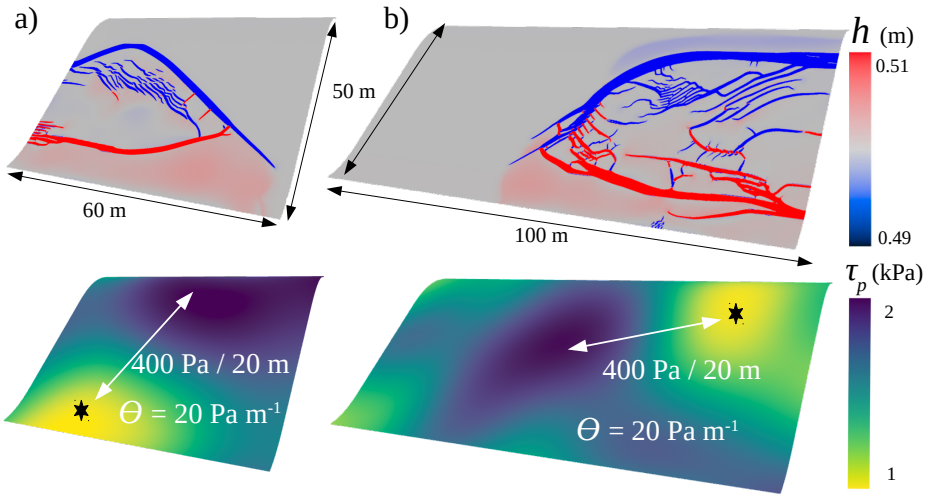

Figure 38 – Slope scale crack propagation simulation with weak layer heterogeneity mostly oriented in the a) slope-parallel direction and in the b) cross-slope direction. The particle height h represent the tensile fractures ($h < 0.49$) and the compressive fractures ($h > 0.51$) within the slab. The shear strength gradient was generated with Gaussian Random Field GRF, corresponding to a θ of 20 Pa m^{-1} in slope parallel direction and cross-slope direction, a slab elastic modulus E of 4 MPa, and a tensile strength of 4 kPa. We initiated a crack in the weak zone, denoted by a black star, at the weaker area with the same procedure as in the PST.

propagation is easier to stop, as shown in the previous section. In the up-slope direction, terrain variations (reduction in slope angle) induce the arrest of the crack and the slab tensile failure.

3.6 Discussion

In this study, we investigated the mechanical drivers of crack arrest during dynamic crack propagation in snow slab avalanche release. For this purpose, we used a depth-averaged Material Point Method (DA-MPM, Guillet *et al.* (2023)) which relies on a strain-softening shear failure model for the weak layer, and an elasto-plastic model for the overlaying slab. Two types of crack arrest were investigated: i) crack arrest induced by heterogeneity of weak layer mechanical properties (here the strength) and ii) crack arrest induced by slab fracture.

Initial findings with a pure-elastic slab regarding the effect of softening and shear strength gradient were rather intuitive, but had not been quantified yet. An increasing weak layer shear strength gradient implied a decreasing crack arrest length, as expected. In addition, we showed that increasing weak layer fracture energy dissipated during the softening phase, resulted in reduced propagation distances. We also report a strong dynamic effect on the slab tensile stress state with higher crack propagation speeds leading to lower slab tensile stress compared to quasi-static predictions. This stress reduction, observed in numerical simulations has been verified on the basis of analytical developments (see Appendix A). This result suggests that fast cracks in the weak layer are likely to produce larger release areas. In the context of the anticrack to supershear transition reported by Trottet *et al.* (2022) and Bobillier *et al.* (2024a,b), this also implies that slab fractures in the supershear regime are likely to occur at larger distances from the initiation point compared to the anticrack propagation regime which involve much lower crack speeds (below c_s). Gaume *et al.* (2015b) made similar observations with smaller PST experiment of 2 m long in DEM. They observed a lower tensile stress in dynamic crack propagation compared to the quasi-static tensile stress. This resulted in a longer propagation distance compared to predictions from beam theory. Furthermore, although they did not study the interplay between crack dynamics and slab fracture in details, Gaume *et al.* (2015a) reported a reduction in slab tensile fracture propensity with increasing slab density (and thus stiffness). They attributed this reduction to smoothing effects which could however be exacerbated by the dynamic effects revealed here.

In a second step, PST simulations with an elasto-plastic slab demonstrated that crack arrest could occur for much lower shear strength gradients compared to pure elastic slabs because of the occurrence of slab fracture. More precisely, slab fracture significantly reduced the crack arrest length for the same the shear strength gradient. Although the positive shear strength gradient induced a reduction of the crack speed, slab fracture had the most significant effect and appeared to be the main driver of crack arrest (Figure 33). In numerous of the presented simulations, multiple slab fractures were needed to stop the crack and the number of slab fractures decreased with increasing shear strength gradient. These multiple

fractures are reminiscent of the ”en-echelon” slab fracture mechanism reported in Gauthier and Jamieson (2016) and further discussed in Gaume *et al.* (2019); Trottet *et al.* (2022). It is important to note that slab fractures alone are insufficient to arrest the crack in this supershear regime, as reported by Trottet *et al.* (2022). It is really the interplay between slab fracture and spatial variability that ultimately contribute to crack arrest. In our study, heterogeneity is represented by a weak layer strength increase. In principle, variability of topography and/or other mechanical properties could induce a similar effect and should be studied in the future.

The stopping of the crack propagation by tensile fracture was previously observed by many in smaller PST experiment (Birkeland *et al.*, 2014; Gaume *et al.*, 2015b; van Herwijnen, 2005; Bergfeld *et al.*, 2023). However, the crack arrest conditions explored in our study are not comparable to the ones reported in smaller PST experiments by the latter authors. The tensile fracture reported in their work originated mostly from the top of the slab caused by the bending of the slab due to collapse weak layer. Because our model relies on a pure shear weak layer failure model, following ideas of Guillet *et al.* (2023) and results of Trottet *et al.* (2022), our model, by nature, cannot reproduce such observations. However, Gaume *et al.* (2019) observed in 3D MPM slab avalanche simulations that some slab fractures originated from the bottom of the slab. Trottet *et al.* (2022) corroborated these observations and added that this slab tensile fracture were related to the shear band propagation in the supershear propagation regime. Crack arrest resulting from slab fractures branching from the bottom of the slab was also reported in Bair *et al.* (2016) and McClung (2021) based on avalanche crown observations. Hence, our study focuses on such slab fracture originating from weak layer shear band propagation and influencing wide-spread propagation and not on slab fractures reported at small-scale related to the anticrack mechanism.

The applicability of the proposed model was tested in three ways. First, scaling laws for the crack arrest length were proposed and could be implemented in operational snow cover and forecasting models as avalanche size indicators (Durand *et al.*, 1999; Lehning *et al.*, 1999; Reuter and Schweizer, 2018). Second, it was applied to PST cases in which spatial variability

of weak layer shear strength was obtained directly from *in-situ* measurements (Meloche *et al.*, 2024). Third, simulations over 3D topography with realistic weak layer strength spatial variability. While most of the present study focused on up-slope and mode II crack propagation, these simulations showed significantly lower crack propagation speeds in the cross-slope direction and thus in mode III. This corroborates recent findings Guillet *et al.* (2023); Trottet *et al.* (2022); Simenhois *et al.* (2023) as well as theoretical bounds (Broberg, 1989). Although these applications bring us a step closer towards estimating avalanche release sizes, further research is needed to investigate the complex three-dimensional interplay between mode II (up/down-slope), mode III (cross-slope) shear band propagation, slab fracture and crack arrest in order to fully understand the mechanical and geometrical drivers of the shape and size of avalanche release zones.

Regarding limitations, we recall that the nature of the numerical (depth-averaged) and mechanical (weak layer mode II failure) models employed in this study only allows us to simulate the supershear crack propagation regime (Trottet *et al.*, 2022) and prevents us from modeling weak layer volumetric collapse and associated slab bending. As a consequence, our model is well suited to evaluate the release sizes of rather large avalanches, and may overestimate the size of small soft slabs with lower densities. The validity of this DA-MPM model for soft slab avalanche modeling could be further assessed by comparing results with 3D MPM which can simulate both anticrack and supershear crack propagation regimes. However, in view of risk management, we believe that this model can provide conservative estimates that can be used as input of avalanche dynamics models for hazard mapping purposes. In fact, in principle, the present model could be extended to simulate, in a unified way, both the release and the flow of the avalanche, in a similar manner as in Zhang and Puzrin (2021) for submarine landslides. The model already captures slab fragmentation after the release of the slab but additional work is required to modify the extent of the material to simulate after the release (deletion of particles outside the release zone), the rheological model which should incorporate rate-dependent behavior (Gaume *et al.*, 2020; Blatny, 2023) as well as entertainment and centrifugal laws.

Finally, although the present application focused on crack arrest mechanisms in snow slab avalanches, similar analyses have been proposed to evaluate failure extension in landslides (Zhang *et al.*, 2021) and earthquakes (Barras *et al.*, 2023) using closed-form criteria and analytical solutions. With process-specific modifications, we believe that the model presented here could be broadly applicable to other geophysical processes as well, providing a robust framework for understanding and predicting failure dynamics across a range of natural phenomena.

3.7 Conclusion

This study provides a comprehensive exploration of dynamic crack propagation on inclined slopes, particularly focusing on factors affecting crack arrest in the recently discovered supershear propagation regime. By initially examining pure-elastic slabs and then incorporating elasto-plastic behavior, critical factors such as the softening coefficient, shear strength gradient, crack propagation speed and steady-state distance were identified as influential in determining crack behavior and arrest distances. Importantly, the study revealed that crack dynamics and arrest mechanisms differ significantly from quasi-static predictions, with implications for understanding slab fracture propensity and avalanche release sizes. By conducting sensitivity analysis, proposing scaling laws and performing field data-informed simulations over 2D and 3D topographies, the research offers valuable insights for potential avalanche release size parameterizations based on terrain and snow properties. While highlighting practical implications for avalanche forecasting and risk assessment, the study also points to the need for further investigation, particularly in understanding crack arrest drivers in different fracture propagation modes and in complex 3D scenarios. Ultimately, this study advances our understanding of crack propagation dynamics and arrest in snow slab avalanches and lays the groundwork for future research in this field, contributing to avalanche risk management. For instance, the findings could inform the development of targeted mitigation strategies in avalanche release zones, aimed at preventing widespread crack propagation and reducing the

avalanche size and its impact.

3.8 Acknowledgements

This project was funded by the Quebec Research Funds - Nature and Technologies (FRQNT) and the Swiss National Science Foundation. We would like to thank all members of the chair of Alpine Mass movements ALMO, and also Guillaume Meyrat at SLF, who shared ideas during team meetings and coffee breaks.

CONCLUSION GÉNÉRALE

Cette conclusion synthétise les avancées réalisées tout au long de cette thèse, explorant la variabilité spatiale des propriétés mécaniques de la neige, son influence sur le danger d'avalanche, et pour terminer avec les mécanismes d'arrêt de la propagation dynamique des fissures pour déterminer la taille finale d'une avalanche. L'objectif principal de cette thèse est de comprendre l'influence de la variabilité spatiale de la neige sur le danger d'avalanche. Le premier chapitre a approfondi notre compréhension de la variabilité spatiale de la neige et a testé de nouvelles méthodes pour prédire celle-ci. Il a également fourni des connaissances et des données qui seront essentielles afin de bien paramétrer les méthodes utilisées dans les chapitres subséquents. Le deuxième chapitre représente le chapitre phare de cette thèse puisqu'il répond à l'objectif principal en s'appuyant sur des éléments du premier chapitre. Il explore en détail l'influence de la variabilité spatiale des propriétés mécaniques de la neige sur le danger d'avalanche, offrant ainsi des contributions significatives à la compréhension de ce phénomène complexe. Le troisième chapitre, basé sur les limites identifiées dans le deuxième chapitre, a permis d'approfondir nos connaissances sur l'effet de la variabilité spatiale de la couche faible et sur la propagation de la fissure déterminant la taille d'une avalanche. Cette conclusion présente une synthèse de ces trois chapitres, une discussion sur le fil conducteur de la thèse et les liens entre les chapitres, ainsi que des perspectives de recherches futures.

Variabilité spatiale de la neige

Tout d'abord, un des apports majeurs de cette étude réside dans l'analyse approfondie de la variabilité spatiale des propriétés mécaniques de la neige. Les patrons spatiaux, représentés à l'aide des variogrammes (Figure 10-11) et des dimensions fractales (Figure 12), révèlent des patrons spécifiques, distinguant clairement les caractéristiques de la plaque et de la couche faible sous-jacente. Bien que Kronholm et Schweizer (2003) et Bellaire et Schweizer (2011) aient déjà mis en évidence cette distinction, leur étude reposait sur des étendues

d'échantillonnages limitées, susceptibles de biaiser les résultats. Cette thèse, avec une étendue d'échantillonnage plus important, confirme que la corrélation spatiale de l'épaisseur et de la masse volumique de plaque diffère significativement de celle de la résistance de la couche faible, indiquant des variations distinctes dans la structure spatiale. Plus précisément, les propriétés de la plaque présentent des longueurs de corrélations spatiales plus courtes et des dimensions fractales plus élevées, démontrant des patrons spatiaux caractérisés par une rugosité plus prononcée. Il est donc évident que les modèles mécaniques doivent prendre en compte les différentes patrons spatiaux de la plaque et de la couche faible pour obtenir des simulations réalistes. Ce résultat a un impact significatif sur les deux chapitres subséquents et sera discuté dans les prochaines sections.

Le premier chapitre visait également à utiliser des indicateurs microtopographiques pour prédire spatialement les propriétés mécaniques de la neige. Les erreurs d'estimation démontrent que les indicateurs microtopographiques contribuent significativement à la prédiction spatiale. Cependant, l'utilisation des indicateurs microtopographiques était spécifique à chaque site d'étude, ainsi qu'à chaque propriété modélisée (Table 3-4). Ce constat indique qu'aucune extrapolation des modèles et des résultats à d'autres sites d'étude n'est possible. Par conséquent, l'application de ces résultats est très limitée et aucune tendance ou relation n'a pu être établie entre la variabilité spatiale d'une propriété et un indicateur microtopographique spécifique. Néanmoins, ce premier chapitre montre tout de même que ces indicateurs peuvent être utiles pour la prédiction spatiale. Une application possible serait d'utiliser ces indicateurs microtopographiques pour inférer sur la variabilité spatiale intra-grille d'un modèle de simulation de couverture de neige, tel SNOWPACK et ALPINE3D.

Danger d'avalanche

Le deuxième chapitre présente une approche statistico-mécanique novatrice visant à comprendre l'influence de la variabilité spatiale de l'épaisseur de la plaque sur la probabilité

de déclenchement par skieur et la taille probable de l'avalanche. Cette approche repose sur des patrons spatiaux de l'épaisseur de la plaque générés artificiellement par un algorithme nommé *Gaussian Random Field* GRF. Contrairement aux résultats obtenus au chapitre 1, il est important de noter ici que la résistance de la couche faible a été paramétrée en fonction de l'épaisseur de la plaque, donnant lieu à des patrons spatiaux identiques entre la plaque et la couche faible. Ce choix méthodologique peut sembler surprenant, étant donné que la recommandation du chapitre 1 est d'avoir deux patrons spatiaux différents. Cependant, la décision de choisir un patron spatial identique visait à simplifier les simulations afin de limiter l'effet uniquement d'une variation de l'épaisseur de la plaque. Bien que des patrons spatiaux différents aient été testés initialement, cela ajoutait une complexité qui rendait difficile l'analyse exclusive de l'effet de la variation de l'épaisseur de la plaque sur la probabilité de déclenchement et la taille de l'avalanche.

L'analyse de sensibilité a révélé des relations distinctes entre les paramètres définissant la variabilité spatiale de l'épaisseur de la plaque : la moyenne, la variance et la longueur de corrélation. Alors qu'une augmentation de la probabilité de déclenchement par skieur est inversement corrélée à l'épaisseur moyenne de la plaque, la longueur de tension et la taille potentielle de l'avalanche montrent une proportionnalité directe avec l'épaisseur moyenne de la plaque. Ce résultat s'aligne avec des études antérieures mettant en avant le rôle des plaques plus épaisses (donc plus résistantes en tension) dans la promotion d'avalanches plus importantes (Gaume *et al.*, 2015a). Ensuite, l'augmentation de la variance crée des zones où la plaque est plus mince et plus susceptible à un déclenchement et une propagation sur la pente, ce qui augmente la probabilité de déclenchement par skieur. Les variations à courtes distances augmentent le nombre de zones faibles de propagation, ce qui augmente la probabilité de déclenchement par le skieur. Le contraire s'applique aux longues variations qui diminuent la probabilité de déclenchement car il y a moins des zones de déclenchement, mais celles-ci sont plus grandes sur l'ensemble de la pente. Il est à noter que cette relation est inverse pour le déclenchement naturel, puisque les variations longues déstabilisent la pente contrairement aux courtes variations (p.ex. : Gaume *et al.*, 2014; Schweizer *et al.*, 2008a). L'influence de

la variance et de la longueur de corrélation sur la propagation et la taille de l'avalanche est plus nuancée, car cela engendre des fluctuations de contraintes en tension dans la plaque qui mène généralement à des avalanche plus petites lorsque la plaque est mince et plus grandes lorsque la plaque est épaisse. Ces résultats doivent aussi être nuancés puisque les simulations démontrant cette relation possède un montant considérable de variabilité.

De plus, le deuxième chapitre a utilisé cette même approche statistico-mécanique pour vérifier certaines connaissances développées par les guides de ski, notamment sur l'impact significatif de la trajectoire du skieur sur la probabilité de déclenchement. Il a été démontré qu'une trajectoire linéaire diminue la probabilité de déclenchement, contrairement à une trajectoire traversant la largeur de la pente, comme par exemple une trajectoire de montée. L'étude examine également l'effet de skier près de traces existantes par rapport à une approche aléatoire de style de ski. Les résultats démontrent que de skier près de traces établies peut réduire significativement la probabilité de déclenchement. Cette stratégie de ski peut augmenter considérablement la taille d'un groupe de skieur, en moyenne un groupe avec 10 skieurs de plus qu'une approche aléatoire, validant quantitativement des pratiques déjà établies chez les guides professionnels de ski. Ces résultats ont des implications pratiques significatives dans le domaine de la sécurité et de la prévention des avalanches.

En terme d'applicabilité des résultats, la variabilité spatiale de l'épaisseur de la plaque introduit un aspect aléatoire et imprévisible, créant des zones fragiles où la trajectoire du skieur détermine s'il y aura une avalanche ou non. À titre personnel, ce résultat vient influencer mon comportement futur en ski d'arrière-pays, puisqu'il démontre qu'il y aura toujours un aspect de probabilité et d'aléatoire introduit par le skieur et sa trajectoire. Pour finir, le deuxième chapitre répond à l'objectif principal avec une figure synthèse (Figure 25), qui présente l'effet de l'épaisseur moyenne de la plaque et de la variance sur le danger d'avalanche, définit par la probabilité de déclenchement et la taille de l'avalanche. Cette figure illustre la relation inverse entre les probabilités et les conséquences, mais démontre également que l'ajout d'une variabilité dans l'épaisseur de la plaque permet des avalanches de taille plus

importantes qui ne pourraient pas être déclenchées par un skieur sur un manteau neigeux plus homogène.

Bien que les méthodes novatrices utilisées dans cette étude offrent une nouvelle perspective, certaines limitations et hypothèses nécessitent d'être approfondies par de futures recherches. La méthode analytique utilisée pour le déclenchement du skieur suppose que la charge du skieur est statique le long des traces, négligeant les variations potentielles de pression lors des virages. L'ajout d'une profondeur de pénétration du skieur et d'une pression supplémentaire à l'apex des virages pourraient influencer les résultats. L'étude néglige également l'effondrement volumétrique dans la couche faible et la flexion de la plaque en raison des hypothèses de la méthode 2D moyennée en épaisseur *DAMPM*. Une étude comparative avec une méthode MPM en 3D pourrait permettre de valider ces résultats et de mieux comprendre l'influence de la variation de la neige sur la propagation de la fissure.

Malgré la suggestion du premier chapitre d'inclure différents patrons spatiaux entre la plaque et la couche faible, le modèle présenté dans le deuxième chapitre de cette thèse est basé sur un patron spatial identique entre la plaque et la couche faible. Il est probable que l'intégration d'une telle différence n'aurait pas un impact significatif sur les résultats concernant le déclenchement par skieur, car une telle paramétrisation créerait sensiblement les mêmes zones faibles susceptibles à la propagation sur la pente. Cependant, une paramétrisation avec des patrons spatiaux différents pourrait modifier les résultats concernant la propagation des fissures et la taille de l'avalanche. Dans la paramétrisation utilisée dans le chapitre 2, l'épaisseur de la plaque augmente avec la résistance de la couche faible, ce qui crée des zones où les contraintes en cisaillement (épaisseur de plaque) diminue au même endroit que la résistance au cisaillement de la couche faible diminue. Ceci crée donc une variation identique entre la contrainte de la plaque et la résistance de la couche faible, ce qui semble peu affecter la propagation de la fissure. Cependant, l'inverse, c'est-à-dire des zones avec une plaque mince et une résistance élevée, pourrait ralentir suffisamment la propagation pour causer l'arrêt de la propagation. Cette paramétrisation avec des patrons spatiaux différents

n'a jamais été testé pour la propagation des fissures et les futures recherches devraient se concentrer sur ce sujet. Comme démontré dans le premier chapitre, ces patrons spatiaux se retrouvent sur le terrain. Une paramétrisation avec des patrons spatiaux différents pourrait mener à des simulations de propagation plus réalistes pour estimer la taille de l'avalanche.

Mécanisme d'arrêt de propagation des fissures dans la neige

Une des limites du deuxième chapitre a motivé l'élaboration du troisième et dernier chapitre. La première apparition d'une fracture en tension dans la plaque a été utilisée comme proxy pour déterminer la longueur de propagation et la taille potentielle de l'avalanche. Dans la réalité, un arrêt complet de propagation est nécessaire pour déterminer la taille finale de l'avalanche, mais ceux-ci n'ont presque pas été observés dans les simulations du deuxième chapitre. Cette absence d'arrêt de propagation a motivé l'élaboration du dernier chapitre qui est basé sur l'hypothèse suivante : seulement deux facteurs peut arrêter une propagation de fissure en régime *supershear*, soit une hétérogénéité dans la couche faible ou un changement de l'angle de pente. Cette hypothèse est également basée sur l'observation de Trottet *et al.* (2022), qui a démontré que les fractures en tension dans la plaque n'affectaient pas la vitesse de propagation lorsque celle-ci avait atteint le régime *supershear*. Le dernier chapitre explore la propagation de fissures en régime *supershear* sur des pentes inclinées, mettant en lumière des paramètres clés qui influent sur les mécanismes d'arrêt des fissures. Il présente des analyses basées sur des simulations avec des plaques purement élastiques (sans fracture de tension), des simulations de plaques élastoplastiques (avec fracture de tension), et une simulation à l'échelle de la pente avec une variabilité naturelle mesurée au chapitre 1.

Les simulations de plaques purement élastiques ont révèlé des facteurs cruciaux affectant le comportement de propagation des fissures et la longueur d'arrêt des fissures (L_{ca}). Les résultats de ces simulations permettent d'identifié le coefficient d'adoucissement ou *softening* (δ), le gradient de résistance au cisaillement (θ) et la longueur de régime permanent

(L_{ss}) comme étant cruciaux pour déterminer la longueur d'arrêt. De plus, les simulations ont montré un régime «sous-contrainte» ou «*under-stress*» en tension, caractérisé par une différence entre l'accumulation de contrainte en tension quasi-statique et dynamique. Ce régime «sous-contrainte» démontre une relation inverse entre la vitesse de propagation de la fissure et l'accumulation des contraintes en tension dans la plaque. Cette observation suggère que les avalanches liées au régime *supershear* seraient responsables des plus grosses avalanches.

Ensuite, les simulations de plaques élastoplastiques ont démontré que des valeurs plus basse de gradients de résistance au cisaillement étaient nécessaires pour obtenir sensiblement les mêmes distances d'arrêt (50-100 m) que les simulations élastiques. Les gradients nécessaires pour obtenir un arrêt étaient plus petit d'un ordre de magnitude, passant environ de 100 à 10 Pa m^{-1}. L'interaction entre la résistance au cisaillement et les fractures de plaques influence significativement la vitesse de propagation, soulignant d'abord la nécessité d'un "ralentissement" relatif dans la couche fragile, suivie ensuite d'un arrêt complet causé par les fractures en tension de la plaque. Il est important de mentionner que seules les fractures en tension ne peuvent arrêter la propagation tel que démontrer par Trottet *et al.* (2022). Une analyse de sensibilité sur le gradient de résistance au cisaillement (θ), la résistance en tension de la plaque (σ_t), le module élastique de la plaque (E) et la longueur de régime permanent (L_{ss}) a montré les rôles dominants du gradient de résistance au cisaillement et de la résistance en tension de la plaque dans la détermination de la longueur d'arrêt de propagation de la fissure. Une analyse dimensionnelle a introduit deux nombres sans dimension cruciaux, "*Strain*" (S) et "*relative weak layer increase*" (T_{wl}), offrant une compréhension du système et des perspectives pour des solutions analytiques. Ces solutions pourraient mener à d'éventuelles méthodes de détermination de la taille finale de l'avalanche basées sur la topographie et des sorties de modèles de couvertures de neige comme SNOWPACK et ALPINE3D. Pour y arriver, d'autres études sont nécéssaires pour valider si les mécanismes d'arrêt sont similaires avec une changement d'angle de pente au lieu du gradient de résistance de la couche faible.

À la lumière des résultats de ce dernier chapitre, il est crucial de discuter des résultats du chapitre 2 concernant l'influence de la variation de l'épaisseur de la plaque sur la propagation de la fissure. Il a été démontré qu'une variation d'épaisseur de plaque modifie les contraintes en tension dans la plaque, ce qui influence l'emplacement où se produit la fracture en tension sans pour autant entraîner un arrêt de propagation. Il est donc évident qu'une variation de l'épaisseur de la plaque à elle seule ne peut pas provoquer des arrêts, considérant une variation identique entre la plaque et la couche faible. Comme discuter précédemment, cette paramétrisation est cruciale car elle peut entraîner une augmentation de la vitesse de propagation (en réduisant les contraintes et la résistance). Alors qu'un ralentissement significatif est nécessaire, combiné à une fracture en tension, pour obtenir un arrêt de propagation. Cependant, dans la réalité, il a souvent été observé qu'une plaque mince provoque une fracture en tension et l'arrêt de la propagation. Il est donc contre-intuitif de penser que seule l'épaisseur de la plaque va varier sur le terrain, tandis que tous les autres paramètres restent constants, y compris l'angle de la pente. Il est plus réaliste de penser qu'une diminution de l'épaisseur de la plaque pourrait être liée, par exemple, à la proximité d'une crête qui entraîne une diminution de l'angle de la pente, et probablement une exposition au vent qui pourrait augmenter la résistance de la couche fragile. Ce scénario de variations des paramètres peut entraîner un ralentissement de la vitesse de propagation et causer un arrêt lorsque la plaque est mince. Ainsi, une multitude de paramètres pourrait provoquer l'arrêt de la propagation. L'élément clé à retenir est qu'un ralentissement de la vitesse de propagation, combiné à une fracture en tension, doit survenir pour entraîner l'arrêt. Ce ralentissement survient lorsque les contraintes en cisaillement diminuent ou que la résistance au cisaillement de la couche fragile augmente.

Une limite importante du dernier chapitre mérite une discussion approfondie, car celui-ci se concentre sur la propagation en régime *supershear* sur des pentes inclinées, par opposition au mode de propagation d'effondrement *anticrack* possible sur un terrain plat à des vitesses plus faibles. Une question majeure découle de cette limitation concernant les arrêts obtenus avec la méthode DAMPM qui peut uniquement représenter une propagation en ci-

saillement :

— Est-ce que les arrêts obtenus auraient simplement continué à se propager en mode de propagation d'effondrement *anticrack* ?

Cette question légitime nécessiterait une validation avec une méthode 3D MPM, qui peut simuler le mode de propagation d'effondrement *anticrack*. Cependant, la majorité des arrêts obtenus sont survenus lors de vitesses supérieures aux ondes élastiques de la plaque (c_s). Ces vitesses sont impossibles lors d'un mode de propagation d'effondrement *anticrack*, ce qui augmente la confiance concernant les arrêts observés en régime *supershear*. Néanmoins, plusieurs questions subsistent, notamment sur la cause de ces arrêts, qui pourraient être liés au décalage lors de la propagation entre la position du maximum de contrainte en cisaillement et le maximum des contraintes en tension de la plaque. Cette piste de réflexion devrait également être exploré avec une validation s'appuyant sur des simulations MPM en 3D pour discerner la nature de l'arrêt de propagation fissures.

Les investigations sur la propagation de la fissure dans le sens de la pente a révélé une propagation de fissures en mode II (cisaillement) due au glissement de la plaque vers le bas de la pente. Les perspectives de recherche pourraient porter sur l'arrêt de la propagation dans la direction transversale à la pente en mode III, qui est un mode de propagation en déchirement rotationel. Les vitesses de propagation observées en direction transversale sont significativement plus lentes (sub-Rayleigh) que les vitesses du régime *supershear*, et pourrait causer des arrêts plus facilement (Trottet *et al.*, 2022; Guillet *et al.*, 2023; Simenhois *et al.*, 2023). En plus d'avoir un aspect fondamental sur la mécanique de propagation, ces futures recherches pourraient mener au développement de nouvelles structures d'atténuation du danger d'avalanche, notamment des structures qui pourraient limiter la propagation transversale des fissures et la taille des avalanches. Ce type de structure représentent un énorme potentiel pour la gestion des avalanches le long des tronçons routiers, puisqu'elles pourraient créer, par exemple, deux petites avalanches qui n'atteindront pas la route, au lieu potentiellement d'une grosse avalanche avec une plus grande distance d'arrêt sur la route. Ces mêmes recherches ont également le potentiel d'améliorer l'aménagement des forêts en montagne, en

suggérant par exemple des masse volumiques minimales d'arbres pour limiter la propagation des avalanches dans des pentes nouvellement ouvertes pas les coupes forestières. La gestion des arbres morts et débris ligneux en montagne est également un enjeux qui est intéressant, car ces débris pourraient limiter la taille des avalanche en laissant une rugosité naturelle et créer une hétérogénéité dans la neige.

Pour conclure, cette thèse a été inspirée par de nombreuses publications scientifiques de qualité à travers le monde durant les dernières décennies. Ce projet vient rajouter des connaissances sur ce sujet passionnant, en espérant qu'il inspira d'autres chercheurs à poursuivre la recherche dans ce domaine.

ANNEXE I

LOG-LOG VARIOGRAMS

The log-log variograms needed to calculate the fractal dimension in Figure 12 are presented below (Figure 39).

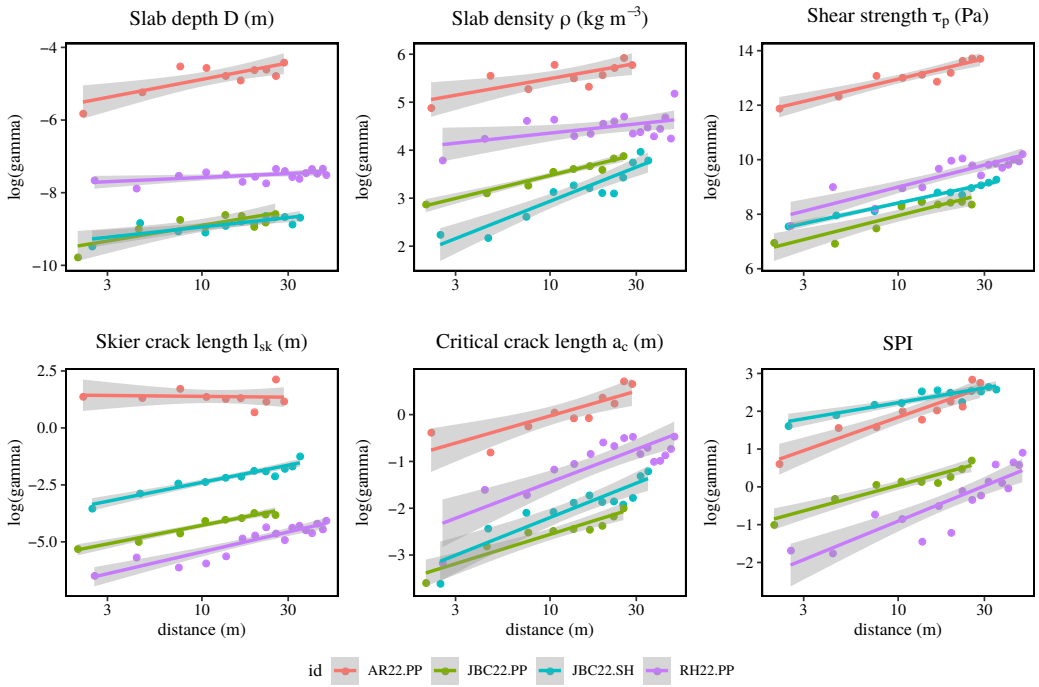

Figure 39 – Log-Log variogram of snow mechanical properties and stability metrics for every snow spatial surveys. The fractal dimension is computed from the slope of the regression line. The gamma represented the variance for each variable. The unit is specified in each title.

ANNEXE II

NUMBER OF SKIER TO CONVERGENCE

The number of skiers on the slope to compute the skier-triggering probability is important in order to get a stable result. The convergence over the total number of skiers was checked and presented in Figure 40. Forty was chose to be the amount of skier on the slope for this study.

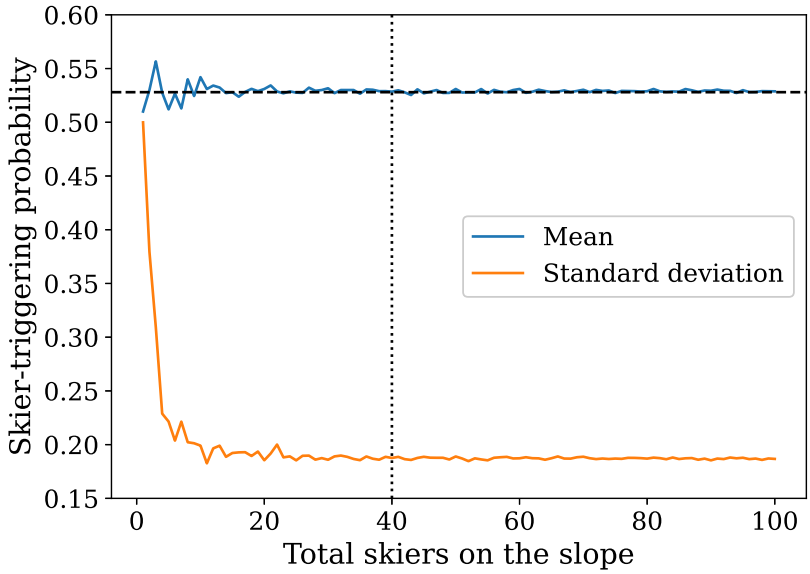

Figure 40 – Convergence of the total number of skiers used to compute the probability of skier-triggering for GRF parameters of 0.7 m mean slab depth, 0.0075 m^2 variance and 20 m correlation length. The blue line shows the convergence of the mean after 100 realizations and the orange line shows the standard deviation after 100 realizations.

ANNEXE III

GRF TENSILE LENGTH

The use of GRF for the PST simulations resulted in different values of tensile length for the same GRF parameters. The use of GRF also smooths the variation and, therefore, the fluctuation in tensile stress in the slab (Figure 41).

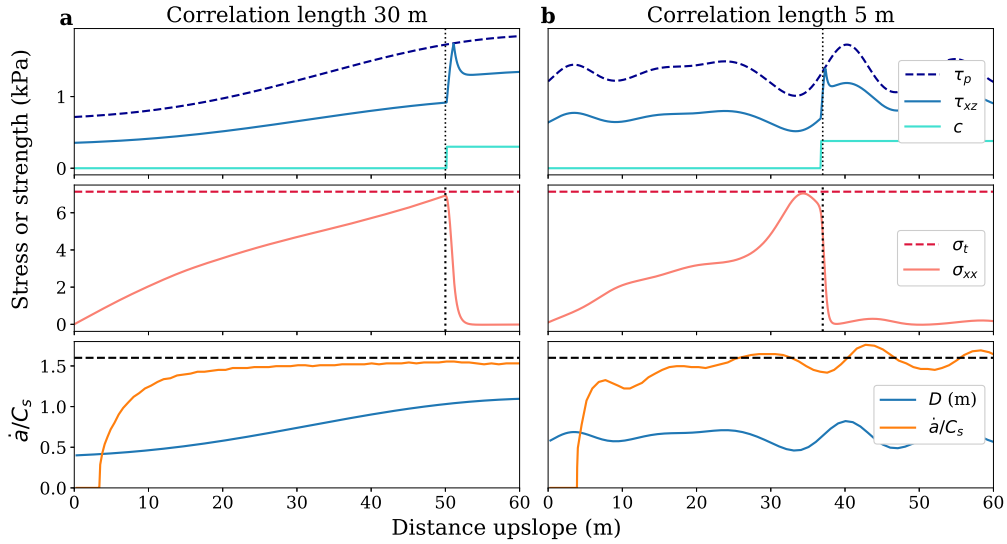

Figure 41 – Two different regimes of tensile fracture for a 0.7 m slab depth $\overline{D}$ and 0.025 m variance S_D^2. These three simulations show the last frame saved just before the tensile fracture occurs when $\sigma_{xx} = \sigma_t$. The shear stress τ_{xz} and the weak layer shear strength τ_p and the cohesion c are also represented. The crack tip (dotted line) is located just behind the peak of τ_{xz} at the loss of cohesion c. The distance between the crack tip and the τ_{xz} peak is due to the softening δ. The bottom plot shows the corresponding crack speed $\dot{a}$ which is normalized over the shear wave speed $C_s = \sqrt{\frac{G}{\rho}}$, and the slab depth D in m. (a) PST simulation with a ϵ of 30 m just before a tensile fracture occurs. (b) PST simulation using GRF with a ϵ of 5 m just before a tensile fracture occurs.

ANNEXE IV

ANALYTICAL SOLUTION FOR THE "CONTROLLED" REGIME WITH PURELY ELASTIC SLAB

Let's consider a classic one dimensional model. We recall that we qualify the regime as "controlled" if the shear strength of the WL tends toward infinity (which means that there is no critical length) and the speed of the crack is manually imposed and constant. The failure only occurs by setting the cohesion to 0 (damaged weak layer) and the shear stress to the residual friction stress τ_r. Even in this case, the time derivative of the displacement is not null and we need to consider the dynamic equation instead of the quasi-static ones, more commonly used. The displacement $u(x,t)$ must satisfy

$$-\frac{1}{c_p^2}\frac{\partial^2 u}{\partial t^2} + \frac{\partial^2 u}{\partial x^2} = \frac{\tau_g}{E'h} + \frac{\tau(u)}{E'h}. \tag{11.1}$$

where $c_p = \sqrt{\frac{E'}{\rho}}$ is the longitudinal wave speed in 1 dimension and E' is the apparent Young's modulus. The function τ is defined in the "controlled" regime by

$$\tau(u(x,t)) = \tau_r \text{ if } x \leq \dot{a}t \text{ (Zone 1 : No Cohesion)} \tag{11.2}$$

$$\tau(u(x,t)) = K_{WL}u(x,t) \text{ if } x > \dot{a}t \text{ (Zone 2 : Cohesion).} \tag{11.3}$$

We can then rewrite Eq. (11.1) as

$$\text{if } x \leq \dot{a}t, \quad -\frac{1}{c_p^2}\frac{\partial^2 u}{\partial t^2} + \frac{\partial^2 u}{\partial x^2} = \frac{k_f}{E'} \tag{11.4}$$

$$\text{if } x > \dot{a}t, \quad -\frac{1}{c_p^2}\frac{\partial^2 u}{\partial t^2} + \frac{\partial^2 u}{\partial x^2} = \frac{1}{\Lambda^2}u(x,t) + \frac{\tau_g}{E'h} \tag{11.5}$$

with $k_f = \frac{\tau_g - \tau_r}{h}$ the quasi-static stress slope and $\Lambda = \sqrt{\frac{E'h}{K_{WL}}}$ the caracteristic elastic length. The differential system given by Eqs. (11.4) and (11.5) is highly nonlinear and by itself difficult to solve. However with two minor assumptions we can compute an analytical solution for the stress in Zone 1.

— In Zone 1, the stress has a constant slope in space : the second space derivative $\frac{\partial^2 u}{\partial x^2}$ and

depends only on $\dot{a}$ and k_f.

— The displacement at the frontier is proportional to the time : $u(\dot{a}t, t) \propto t$

Note that these two hypotheses do not rely on purely mathematical development but are very reasonable regarding the physical model and the output of our simulations. We then denote by k the stress slope in zone 1, $k_x = E' \frac{\partial^2 u}{\partial x^2}$. By integrating two times and injecting in Eq. (11.4) we have that

$$u(x,t) = \frac{1}{2}k_x x^2 + \frac{1}{2}c_p^2(k_x - k_f)t^2 + \alpha_1 t + \alpha_2 \tag{11.6}$$

where α_1 and α_2 are two integration constant. The second hypothesis gives that

$$\frac{1}{2}k_x(\dot{a}t)^2 + \frac{1}{2}c_p^2(k_x - k_f)t^2 + \alpha_1 t + \alpha_2 \propto t \tag{11.7}$$

which implies that the term before t^2 must be equals to zero. It then reduces to

$$k_x\dot{a}^2 + \frac{1}{2}c_p^2(k_x - k_f) \iff k_x = \frac{c_p^2 k_f}{\dot{a}^2 + c_p^2} \tag{11.8}$$

Note that when $\dot{a} = c_p$, the slope is just half as the slope in quasi-static regime with $k_x = \frac{k_f}{2}$. Even if the 'controlled' regime has no real physical value when $\dot{a}$ is comparable to c_p, it can gives a strong insight of what must be the value of convergence of the stress slope in self propagating regime.

RÉFÉRENCES

Bair, E. H., J. Gaume,and. Van Herwijnen (2016), The role of collapse in avalanche release: review and implications for practitioners and future research, in International Snow Science Workshop, Breckenridge, Colorado, pp. 24–31.

Barras, F., K. Thøgersen, E. Aharonov,and. Renard (2023). How Do Earthquakes Stop? Insights From a Minimal Model of Frictional Rupture, *Journal of Geophysical Research: Solid Earth*, 128(8), doi:10.1029/2022JB026070.

Bažant, Z. P., G. Zi,and. McClung (2003). Size effect law and fracture mechanics of the triggering of dry snow slab avalanches, *Journal of Geophysical Research: Solid Earth*, 108(B2), doi:10.1029/2002jb001884.

Bellaire, S.,and. Schweizer (2011). Measuring spatial variations of weak layer and slab properties with regard to snow slope stability, *Cold Regions Science and Technology*, 65(2), 234–241, doi:10.1016/J.COLDREGIONS.2010.08.013.

Benedetti, L., J. Gaume,and. T. Fischer (2019). A mechanically-based model of snow slab and weak layer fracture in the Propagation Saw Test, *International Journal of Solids and Structures*, 158, 1–20, doi:10.1016/J.IJSOLSTR.2017.12.033.

Bergfeld, B., A. Van Herwijnen, G. Bobillier, P. L. Rosendahl, P. Weißgraeber, V. Adam, J. Dual,and. Schweizer (2023). Temporal evolution of crack propagation characteristics in a weak snowpack layer: conditions of crack arrest and sustained propagation, *Hazards Earth Syst. Sci*, 23, 293–315, doi:10.5194/nhess-23-293-2023.

Bergfeld, B., *et al.* (2021). Crack propagation speeds in weak snowpack layers, *Journal of Glaciology*, 68(269), 557–570, doi:10.1017/jog.2021.118.

Birkeland, K. W. (2001). Spatial patterns of snow stability throughout a small mountain range, *Journal of Glaciology*, 47(157), 176–186, doi:10.3189/172756501781832250.

Birkeland, K. W., E. Bair,and. Chabot (2014). Proceedings of the 2014 International Snow Science Workshop, Banff, Alberta, , pp. 1–4.

Blatny, L. (2023), Modeling the mechanics and rheology of porous and granular media: an elastoplastic continuum approach, Ph.D. thesis, EPFL, Lausanne.

Blöschl, G.,and. Sivapalan (1995). Scale issues in hydrological modelling: A review, *Hydrological Processes*, 9(3-4), 251–290, doi:10.1002/hyp.3360090305.

Bobillier, G., B. Bergfeld, J. Dual, J. Gaume, A. Van Herwijnen,and. Schweizer (2021). Micro-mechanical insights into the dynamics of crack propagation in snow fracture experiments, *Scientific Reports — Nature*, 11(11711), doi:10.1038/s41598-021-90910-3.

Bobillier, G., B. Bergfeld, J. Dual, J. Gaume, A. Van Herwijnen,and. Schweizer (2024a). Numerical investigation of crack propagation regimes in snow fracture experiments, *Granular Matter*, 26(58), 1–15, doi:10.1007/s10035-024-01423-5.

Bobillier, G., B. Trottet, B. Bergfeld, R. Simenhois, A. Van Herwijnen, J. Schweizer,and. Gaume (2024b). Supershear crack propagation in snow slab avalanche release: new insights from numerical simulations and field measurements, *Natural Hazards and Earth System Sciences Discussion*, pp. 1–15, doi:10.5194/nhess-2024-70.

Broberg, K. B. (1989), The near-tip field at high crack velocities, in Structural Integrity, pp. 1–13, Springer Netherlands, Dordrecht, doi:10.1007/978-94-009-0927-4{_}1.

Calonne, N., B. Richter, H. Löwe, C. Cetti, Judith, A. V. Herwijnen, C. Fierz, M. Jaggi,and. Schneebeli (2019). The RHOSSA campaign: Monitoring the seasonal evolution of an alpine snowpack up to daily resolution, *in Prep.*, (December), 1–30.

Campbell, C.,and. Jamieson (2007). Spatial variability of slab stability and fracture characteristics within avalanche start zones, *Cold Regions Science and Technology*, 47(1-2 SPEC. ISS.), 134–147, doi:10.1016/j.coldregions.2006.08.015.

Canadian Avalanche Association (2016), Observations guidelines and recording standards for weather, snowpack and avalanches, Tech. rep., Revelstoke.

Chilès, J.-P.,and¶. Delfiner (1999), *Geostatistics: Modelling Spatial Uncertainty*, 695 pp., John Wiley & Sons, Ltd, New-York.

Conrad, O., B. Bechtel, M. Bock, H. Dietrich, E. Fischer, L. Gerlitz, J. Wehberg, V. Wichmann,and. Böhner (2015). System for Automated Geoscientific Analyses (SAGA) v. 2.1.4, *Geoscientific Model Development*, 8(7), 1991–2007, doi:10.5194/GMD-8-1991-2015.

Conway, H.,and. Abrahamson (1984). Snow Stability Index, *Journal of Glaciology*, 30(106), doi:10.3189/S002214300000616X.

Dale, M. R. T.,and.-J. Fortin (2014), *Spatial Analysis : A guide for Ecologists*, 2nd ed., 438 pp., Cambridge University Press.

Deems, J. S., S. R. Fassnacht,and. J. Elder (2006). Fractal distribution of snow depth from lidar data, *Journal of Hydrometeorology*, 7(2), 285–297, doi:10.1175/JHM487.1.

Durand, Y., G. Giraud, E. Brun, L. Mérindol,and. Martin (1999). A computer-based system simulating snowpack structures as a tool for regional avalanche forecasting, *Journal of Glaciology*, 45(151), 469–484, doi:10.1017/S0022143000001337.

Duvillier, C., N. Eckert, G. Evin,and. Deschâtres (2023). Development and evaluation of a method to identify potential release areas of snow avalanches based on watershed delineation, *Natural Hazards and Earth System Sciences*, 23(4), 1383–1408, doi:10.5194/nhess-23-1383-2023.

Faillettaz, J., F. Louchet,and.-R. Grasso (2004). Two-Threshold Model for Scaling Laws of Noninteracting Snow Avalanches, *Physical review letters*, 93(20), doi:10.1103/PhysRevLett.93.208001.

Feick, S., K. Kronholm,and. Schweizer (2007). Field observations on spatial variability of surface hoar at the basin scale, *Journal of Geophysical Research: Earth Surface*, 112(2), 1–16, doi:10.1029/2006JF000587.

Fletcher, R. C.,and. D. Pollard (1981). Anticrack model for pressure solution surfaces, *Geology*, 9(9), 419–424, doi:10.1130/0091-7613(1981)9⟨419:AMFPSS⟩2.0.CO;2.

Föhn, P. (1987). The stability index and various triggering mechanisms, *IAHS*, 162, 195–214.

Fyffe, B.,and. Zaiser (2004). The effects of snow variability on slab avalanche release, *Cold Regions Science and Technology*, 40(3), 229–242, doi:10.1016/j.coldregions.2004.08.004.

Gao, J.,and. G. Xia (1996). Fractals in physical geography, *Progress in Physical Geography*, 20(2), 178–191, doi:10.1177/030913339602000204.

Gaume, J.,and. M. Puzrin (2021). Mechanisms of slab avalanche release and impact in the Dyatlov Pass incident in 1959, *Communications Earth & Environment*, 2(1), 10, doi:10.1038/s43247-020-00081-8.

Gaume, J.,and. Reuter (2017). Assessing snow instability in skier-triggered snow slab avalanches by combining failure initiation and crack propagation, *Cold Regions Science and Technology*, 144, 6–15, doi:10.1016/j.coldregions.2017.05.011.

Gaume, J., G. Chambon, N. Eckert,and. Naaim (2013). Influence of weak-layer heterogeneity on snow slab avalanche release: Application to the evaluation of avalanche release depths, *Journal of Glaciology*, 59(215), 423–437, doi:10.3189/2013JoG12J161.

Gaume, J., J. Schweizer, A. Herwijnen, G. Chambon, B. Reuter, N. Eckert,and. Naaim (2014). Evaluation of slope stability with respect to snowpack spatial variability, *Journal of Geophysical Research: Earth Surface*, 119(9), 1783–1799, doi:10.1002/2014jf003193.

Gaume, J., G. Chambon, N. Eckert, M. Naaim,and. Schweizer (2015a). Influence of weak layer heterogeneity and slab properties on slab tensile failure propensity and avalanche release area, *Cryosphere*, 9(2), 795–804, doi:10.5194/tc-9-795-2015.

Gaume, J., A. van Herwijnen, G. Chambon, K. Birkeland,and. Schweizer (2015b). Modeling of crack propagation in weak snowpack layers using the discrete element method, *The Cryosphere*, 9(5), 1915–1932, doi:10.5194/tc-9-1915-2015.

Gaume, J., A. Van Herwijnen, G. Chambon, N. Wever,and. Schweizer (2017). Snow fracture in relation to slab avalanche release: Critical state for the onset of crack propagation, *Cryosphere*, 11(1), 217–228, doi:10.5194/tc-11-217-2017.

Gaume, J., G. Chambon, A. v. Herwijnen,and. Schweizer (2018a). Stress Concentrations in Weak Snowpack Layers and Conditions for Slab Avalanche Release, *Geophysical Research Letters*, 45(16), 8363–8369, doi:10.1029/2018GL078900.

Gaume, J., T. Gast, J. Teran, A. van Herwijnen,and. Jiang (2018b). Dynamic anticrack propagation in snow, *Nature Communications*, 9(1), doi:10.1038/s41467-018-05181-w.

Gaume, J., A. van Herwijnen, T. Gast, J. Teran,and. Jiang (2019). Investigating the release and flow of snow avalanches at the slope-scale using a unified model based on the material point method, *Cold Regions Science and Technology*, 168(102847), doi:10.1016/j.coldregions.2019.102847.

Gaume, J., G. Chambon,and. Naaim (2020). Microscopic Origin of Nonlocal Rheology in Dense Granular Materials, *Physical Review Letters*, 125(18), 188,001, doi:10.1103/PhysRevLett.125.188001.

Gauthier, D.,and. Jamieson (2008). Evaluation of a prototype field test for fracture and failure propagation propensity in weak snowpack layers, *Cold Regions Science and Technology*, 51(2-3), 87–97, doi:10.1016/J.COLDREGIONS.2007.04.005.

Gauthier, D.,and. Jamieson (2016), On the sustainability and arrest of weak layer fracture in Whumpfs and avalanches., in International Snow Science Workshop, Breckenridge, Colorado, pp. 224–231.

Green, H. W., T. E. Young, D. Walker,and. H. Scholz (1990). Anticrack-associated faulting at very high pressure in natural olivine, *Nature*, 348(6303), 720–722, doi:10.1038/348720a0.

Grünewald, T., M. Schirmer, R. Mott,and. Lehning (2010). Spatial and temporal variability of snow depth and ablation rates in a small mountain catchment, *Cryosphere*, 4(2), 215–225, doi:10.5194/tc-4-215-2010.

Grünewald, T., *et al.* (2013). Statistical modelling of the snow depth distribution in open alpine terrain, *Hydrology and Earth System Sciences*, 17(8), 3005–3021, doi:10.5194/hess-17-3005-2013.

Guillet, L., L. Blatny, B. Trottet, D. Steffen,and. Gaume (2023). A Depth-Averaged Material Point Method for Shallow Landslides: Applications to Snow Slab Avalanche Release, *Journal of Geophysical Research: Earth Surface*, p. e2023JF007092, doi:10.1029/2023JF007092.

Guy, Z. M.,and. W. Birkeland (2013). Relating complex terrain to potential avalanche trigger locations, *Cold Regions Science and Technology*, 86, 1–13, doi:10.1016/j.coldregions.2012.10.008.

Habermann, M., J. Schweizer,and. B. Jamieson (2008). Influence of snowpack layering on human-triggered snow slab avalanche release, *Cold Regions Science and Technology*, 54(3), 176–182, doi:10.1016/j.coldregions.2008.05.003.

Hägeli, P.,and. M. McClung (2003). Avalanche characteristics of a transitional snow climate-Columbia Mountains, British Columbia, Canada, *Cold Regions Science and Technology*, 37(3), 255–276, doi:10.1016/S0165-232X(03)00069-7.

Hägeli, P.,and. M. McClung (2004). Hierarchy theory as a conceptual framework for scale issues in avalanche forecast modeling, *Annals of Glaciology*, 38(July 2016), 209–214, doi:10.3189/172756404781815266.

Hagenmuller, P., G. Chambon,and. Naaim (2015). Microstructure-based modeling of snow mechanics: a discrete element approach, *The Cryosphere*, 9, 1969–1982, doi:10.5194/tc-9-1969-2015.

Hamre, D., R. Simenhois,and. W. Birkeland (2014), Fractures speeds of triggered avalanches, in International Snow Science Workshop, Banff, Canada, pp. 174–178.

Harper, J. T.,and. H. Bradford (2003). Snow stratigraphy over a uniform depositional surface: Spatial variability and measurement tools, *Cold Regions Science and Technology*, 37(3), 289–298, doi:10.1016/S0165-232X(03)00071-5.

Harvey, S., H. Rhyner,and. Schweizer (2023), *Lawinen: Verstehen, beurteilen und risikobasiert entscheiden*, Bruckman, München.

Heierli, J., P. Gumbsch,and. Zaiser (2008). Anticrack nucleation as triggering mechanism for snow slab avalanches, *Science*, 321(5886), 240–243, doi:10.1126/science.1153948.

Hesterberg, T., N. H. Choi, L. Meier,and. Fraley (2008). Least angle and l1 penalized regression: A review, *Statistics Surveys*, 2, 61–93, doi:10.1214/08-SS035.

Hubbard, A., D. F. Porter, N. Cullen, R. Mott mott, R. Mott, V. Vionnet,and. Grünewald (2018). The Seasonal Snow Cover Dynamics: Review on Wind-Driven Coupling Processes, *Frontiers in Earth Science*, 6, doi:10.3389/feart.2018.00197.

Jamieson, B. (1999). The Compression Test after 25 Years, *Avalanche Review*, 18(1), 10–12.

Jamieson, J.,and. Johnston (1990). In-Situ Tensile Tests of Snow-Pack Layers, *Journal of Glaciology*, 36(122), 102–106, doi:10.3189/S002214300000561X.

Johnson, B. C. (2000), Remotely Triggered Slab Avalanches, Ph.D. thesis, University of Calgary, Calgary.

Johnson, B. C., J. B. Jamieson,and. R. Stewart (2004). Seismic measurement of fracture speed in a weak snowpack layer, *Cold Regions Science and Technology*, 40(1-2), 41–45, doi:10.1016/J.COLDREGIONS.2004.05.003.

Johnson, J. B.,and. Schneebeli (1999). Characterizing the microstructural and micromechanical properties of snow, *Cold Regions Science and Technology*, 30(1-3), 91–100, doi:10.1016/S0165-232X(99)00013-0.

Knight, C. A.,and. C. Knight (1972). Superheated Ice: True Compression Fractures and Fast Internal Melting, *Science*, 178(4061), 613–614.

Kronholm, K. (2004), Spatial Variability of Snow Mechanical Properties with regard to avalanche formation, Ph.D. thesis, University of Zurich, Zurich.

Kronholm, K.,and. W. Birkeland (2005). Integrating spatial patterns into a snow avalanche cellular automata model, *Geophysical Research Letters*, 32(19), doi:10.1029/2005GL024373.

Kronholm, K.,and. W. Birkeland (2007). Reliability of sampling designs for spatial snow surveys, *Computers and Geosciences*, 33(9), 1097–1110, doi:10.1016/j.cageo.2006.10.004.

Kronholm, K.,and. Schweizer (2003). Snow stability variation on small slopes, *Cold Regions Science and Technology*, 37(3), 453–465, doi:10.1016/S0165-232X(03)00084-3.

Kronholm, K., J. Schweizer, M. Schneebeli,and. Pielmeier (2004). Spatial variability of snowpack stability on small slopes studied with the stuffblock test, *Data of Glaciological studie*, 97, 180–188.

Landry, C., K. Birkeland, K. Hansen, J. Borkowski, R. Brown,and. Aspinall (2004). Variations in snow strength and stability on uniform slopes, *Cold Regions Science and Technology*, 39(2-3), 205–218, doi:10.1016/j.coldregions.2003.12.003.

Lehning, M., P. Bartelt, B. Brown, T. Russi, U. Stockli,and. Zimmerli (1999). SNOWPACK model calculations for avalanche warning based upon a new network of weather and snow stations, *Cold Regions Science and Technology*, 30, 145–157.

Löwe, H.,and. van Herwijnen (2012). A Poisson shot noise model for micro-penetration of snow, *Cold Regions Science and Technology*, 70, 62–70, doi:10.1016/j.coldregions.2011.09.001.

Lutz, E.,and. W. Birkeland (2011). Spatial patterns of surface hoar properties and incoming radiation on an inclined forest opening, *Journal of Glaciology*, 57(202), 355–366, doi:10.3189/002214311796405843.

Lutz, E., K. W. Birkeland, K. Kronholm, K. Hansen,and. Aspinall (2007). Surface hoar characteristics derived from a snow micropenetrometer using moving window statistical operations, *Cold Regions Science and Technology*, 47(1-2 SPEC. ISS.), 118–133, doi:10.1016/j.coldregions.2006.08.021.

Mackenzie, D., J. Shi,and. Boyle (1994). Finite element modelling for limit analysis by the elastic compensation method, *Computers & Structures*, 51(4), 403–410, doi:10.1016/0045-7949(94)90325-5.

Marra, G.,and§. N. Wood (2011). Practical variable selection for generalized additive models, *Computational Statistics and Data Analysis*, 55(7), 2372–2387, doi:10.1016/j.csda.2011.02.004.

McClung, D.,and¶. Schaerer (2006), *The avalanche Hanbook*, The Mountaineers Books.

McClung, D. M. (1981). Fracture mechanical models of dry slab avalanche release, *Journal of Geophysical Research: Solid Earth*, 86(B11), 10,783–10,790, doi:10.1029/JB086IB11P10783.

McClung, D. M. (2009). Dimensions of dry snow slab avalanches from field measurements, *Journal of Geophysical Research: Earth Surface*, 114(1), doi:10.1029/2007JF000941.

McClung, D. M. (2021), Dynamic fracture mechanics in dry snow slab avalanche release, in EGU General Assembly, Vienna.

Mede, T., G. Chambon, F. Nicot,and¶. Hagenmuller (2020). Micromechanical investigation of snow failure under mixed-mode loading, *International Journal of Solids and Structures*, 199, 95–108, doi:10.1016/J.IJSOLSTR.2020.04.020.

Meloche, F., F. Gauthier, A. Langlois,and. Boucher (2018), The Northeastern Rainy Continental snow climate: A snow climate classification for the Gaspé Peninsula, Québec, Canada, in International Snow Science Workshop, Innsbruck, Austria, pp. 1025–1029.

Meloche, F., F. Gauthier,and. Langlois (2024). Snow mechanical property variability at the slope scale – implication for snow mechanical modelling, *The Cryosphere*, 18(3), 1359–1380, doi:10.5194/TC-18-1359-2024.

Meloche, J., A. Langlois, N. Rutter, D. McLennan, A. Royer, P. Billecocq,and§. Ponomarenko (2022). High-resolution snow depth prediction using Random Forest algorithm with topographic parameters: A case study in the Greiner watershed, Nunavut, *Hydrological Processes*, 36(3), e14,546, doi:10.1002/HYP.14546.

Miller, Z. S., E. H. Peitzsch, E. A. Sproles, K. W. Birkeland,and. T. Palomaki (2022). Assessing the seasonal evolution of snow depth spatial variability and scaling in complex mountain terrain, *Cryosphere*, 16(12), 4907–4930, doi:10.5194/TC-16-4907-2022.

Monti, F., J. Gaume, A. Van Herwijnen,and. Schweizer (2016). Snow instability evaluation: Calculating the skier-induced stress in a multi-layered snowpack, *Natural Hazards and Earth System Sciences*, 16(3), 775–788, doi:10.5194/nhess-16-775-2016.

Mott, R., M. Schirmer,and. Lehning (2011). Scaling properties of wind and snow depth distribution in an Alpine catchment, *Journal of Geophysical Research Atmospheres*, 116(6), 1–8, doi:10.1029/2010JD014886.

Mullen, R. S.,and. W. Birkeland (2008). Mixed Effect and Spatial Correlation Models for Analyzing a Regional Spatial dataset, *International snow science workshop*, (406), 8.

Müller, S., L. Schüler, A. Zech,and. Heße (2022). GSTools v1.3: A toolbox for geostatistical modelling in Python, *Geoscientific Model Development*, 15(7), 3161–3182, doi:10.5194/GMD-15-3161-2022.

Nussbaum, M., L. Walthert, M. Fraefel, L. Greiner,and. Papritz (2017). Mapping of soil properties at high resolution in Switzerland using boosted geoadditive models, *SOIL*, 3(4), 191–210, doi:10.5194/SOIL-3-191-2017.

Pebesma, E. J. (2004). Multivariable geostatistics in S: the gstat package, *Computers & Geosciences*, 30, 683–691, doi:10.1016/j.cageo.2004.03.012.

Pielmeier, C.,and P. Marshall (2009). Rutschblock-scale snowpack stability derived from multiple quality-controlled SnowMicroPen measurements, *Cold Regions Science and Technology*, 59(2-3), 178–184, doi:10.1016/j.coldregions.2009.06.005.

Podolskiy, E., G. Chambon, M. Naaim,and. Gaume (2013). A review of finite-element modelling in snow mechanics, *Journal of Glaciology*, 59(218), 1189–1201, doi:10.3189/2013JoG13J121.

Proksch, M., H. Löwe,and. Schneebeli (2015). Density, specific surface area, and correlation length of snow measured by high-resolution penetrometry, *Journal of Geophysical Research: Earth Surface*, 120(2), 346–362, doi:10.1002/2014JF003266.

Pulwicki, A., G. E. Flowers, V. Radic,and. Bingham (2018). Estimating winter balance and its uncertainty from direct measurements of snow depth and density on alpine glaciers, *Journal of Glaciology*, 64(247), 781–795, doi:10.1017/JOG.2018.68.

Puzrin, A.,andŁ. Germanovich (2005). The growth of shear bands in the catastrophic failure of soils, *Proceedings of the Royal Society A: Mathematical, Physical and Engineering Sciences*, 461(2056), 1199–1228, doi:10.1098/rspa.2004.1378.

R Core (2013), R : A language and environment for statistical computing.

Reuter, B.,and. Schweizer (2018). Describing Snow Instability by Failure Initiation, Crack Propagation, and Slab Tensile Support, *Geophysical Research Letters*, 45(14), 7019–7027, doi:10.1029/2018GL078069.

Reuter, B., A. V. Herwijnen,and. Schweizer (2015a). Simple drivers of snow instability, *Cold Regions Science and Technology*, 120(July 2015), 168–178.

Reuter, B., J. Schweizer,and. Van Herwijnen (2015b). A process-based approach to estimate point snow instability, *Cryosphere*, 9(3), 837–847, doi:10.5194/tc-9-837-2015.

Reuter, B., B. Richter,and. Schweizer (2016). Snow instability patterns at the scale of a small basin, *Journal of Geophysical Research: Earth Surface*, 121(2), 257–282, doi:10.1002/2015JF003700.

Reuter, B., M. Proksch, H. Löwe, A. Van Herwijnen,and. Schweizer (2019). Comparing measurements of snow mechanical properties relevant for slab avalanche release, *Journal of Glaciology*, 65(249), 55–67, doi:10.1017/jog.2018.93.

Revuelto, J., P. Billecocq, F. Tuzet, B. Cluzet, M. Lamare, F. Larue,and. Dumont (2020). Random forests as a tool to understand the snow depth distribution and its evolution in mountain areas, *Hydrological Processes*, (April), 1–18, doi:10.1002/hyp.13951.

Richter, B., J. Schweizer, M. Rotach,and. van Herwijnen (2019). Validating modeled critical crack length for crack propagation in the snow cover model SNOWPACK, *The Cryosphere Discussions*, (June), 1–21, doi:10.5194/tc-2019-97.

Rosendahl, P. L.,and¶. Weißgraeber (2020). Modeling snow slab avalanches caused by weak-layer failure - Part 2: Coupled mixed-mode criterion for skier-triggered anticracks, *Cryosphere*, 14(1), 131–145, doi:10.5194/tc-14-131-2020.

Sappington, J. M., K. M. Longshore,and. B. Thompson (2007). Quantifying Landscape Ruggedness for Animal Habitat Analysis: A Case Study Using Bighorn Sheep in the Mojave Desert, *The Journal of Wildlife Management*, 71(5), 1419–1426, doi:10.2193/2005-723.

Scapozza, C., F. Bucher, P. Amann, W. J. Ammann,and¶. Bartelt (2004). The temperature- and density-dependent acoustic emission response of snow in monoaxial compression tests, *Annals of Glaciology*, 38, 291–298, doi:10.3189/172756404781814861.

Schirmer, M.,and. Lehning (2011). Persistence in intra-annual snow depth distribution: 2.Fractal analysis of snow depth development, *Water Resources Research*, 47(9), 1–14, doi:10.1029/2010WR009429.

Schirmer, M., V. Wirz, A. Clifton,and. Lehning (2011). Persistence in intra-annual snow depth distribution: 1.Measurements and topographic control, *Water Resources Research*, 47(9), 1–16, doi:10.1029/2010WR009426.

Schweizer, J.,and. Kronholm (2007). Snow cover spatial variability at multiple scales: Characteristics of a layer of buried surface hoar, *Cold Regions Science and Technology*, 47(3), 207–223, doi:10.1016/j.coldregions.2006.09.002.

Schweizer, J.,and. Reuter (2015). A new index combining weak layer and slab properties for snow instability prediction, *Natural Hazards and Earth System Sciences*, 15(1), 109–118, doi:10.5194/nhess-15-109-2015.

Schweizer, J., J. B. Jamieson,and. Schneebeli (2003). Snow avalanche formation, *Reviews of Geophysics*, 41(4), doi:10.1029/2002RG000123.

Schweizer, J., K. Kronholm, J. B. Jamieson,and. W. Birkeland (2008a). Review of spatial variability of snowpack properties and its importance for avalanche formation, *Cold Regions Science and Technology*, 51(2-3), 253–272, doi:10.1016/j.coldregions.2007.04.009.

Schweizer, J., I. McCammon,and. B. Jamieson (2008b). Snowpack observations and fracture concepts for skier-triggering of dry-snow slab avalanches, *Cold Regions Science and Technology*, 51(2-3), 112–121, doi:10.1016/J.COLDREGIONS.2007.04.019.

Schweizer, J., B. Reuter, A. van Herwijnen,and. Gaume (2016), Avalanche Release 101, in International Snow Science Workshop, Breckenridge, Colorado, pp. 1–11, Breckenridge.

Sigrist, C. (2006), Measurement of fracture mechanical properties of snow and application to dry snow slab avalanche release, Ph.D. thesis, ETH Zürich, Zürich, doi:10.3929/ETHZ-A-005282374.

Simenhois, R.,and. Birkeland (2014), Observations of fracture arrest at slab avalanche boundaries, in International Snow Science Workshop, Banff, pp. 179–184.

Simenhois, R., K. W. Birkeland, J. Gaume, A. Van Herwijnen, B. Bergfeld, B. Trottet,and. Greene (2023). Using video detection of snow surface movements to estimate weak layer crack propagation speeds, *Annals of glaciology*, pp. 1–11, doi:10.1017/aog.2023.36.

Siron, M., B. Trottet,and. Gaume (2023). A theoretical framework for dynamic anticrack and supershear propagation in snow slab avalanches, *Journal of the Mechanics and Physics of Solids*, 181, 105,428, doi:10.1016/j.jmps.2023.105428.

Skøien, J. O.,and. Blöschl (2006). Sampling scale effects in random fields and implications for environmental monitoring, *Environmental Monitoring and Assessment*, 114(1-3), 521–552, doi:10.1007/s10661-006-4939-z.

Statham, G., *et al.* (2018). A conceptual model of avalanche hazard, *Natural Hazards*, 90(2), 663–691, doi:10.1007/s11069-017-3070-5.

Stethem, C., B. Jamieson, P. Schaerer, D. Liverman, D. Germain,and§. Walker (2003). Snow avalanche hazard in Canada - A review, *Natural Hazards*, 28(2-3), 487–515, doi:10.1023/A:1022998512227.

Sulsky, D., Z. Chen,and↽ L. Schreyer (1994). A particle method for history-dependent materials, *Computer Methods in Applied Mechanics and Engineering*, 118(1-2), 179–196, doi:10.1016/0045-7825(94)90112-0.

Techel, F., F. Jarry, G. Kronthaler, S. Mitterer, P. Nairz, M. Pavšek, M. Valt,and. Darms (2016). Avalanche fatalities in the European Alps: Long-term trends and statistics, *Geographica Helvetica*, 71(2), 147–159, doi:10.5194/gh-71-147-2016.

Techel, F., M. Karsten,and. Schweizer (2020). On the importance of snowpack stability, the frequency distribution of snowpack stability, and avalanche size in assessing the avalanche danger level, *Cryosphere*, 14(10), 3503–3521, doi:10.5194/TC-14-3503-2020.

Trottet, B., R. Simenhois, G. Bobillier, B. Bergfeld, A. van Herwijnen, C. Jiang,and. Gaume (2022). Transition from sub-Rayleigh anticrack to supershear crack propagation in snow avalanches, *Nature Physics*, 18(9), 1094–1098, doi:10.1038/s41567-022-01662-4.

Trujillo, E., J. A. Ramírez,and. J. Elder (2007). Topographic, meteorologic, and canopy controls on the scaling characteristics of the spatial distribution of snow depth fields, *Water Resources Research*, 43(7), doi:10.1029/2006WR005317.

van Herwijnen, A. (2005), Fractures in weak snowpack layers in relation to slab avalanche release, Ph.D. thesis, University of Calgary, Calgary.

van Herwijnen, A.,and. Jamieson (2007). Snowpack properties associated with fracture initiation and propagation resulting in skier-triggered dry snow slab avalanches, *Cold Regions Science and Technology*, 50(1-3), 13–22, doi:10.1016/J.COLDREGIONS.2007.02.004.

Veitinger, J., B. Sovilla,and. S. Purves (2014). Influence of snow depth distribution on surface roughness in alpine terrain: A multi-scale approach, *Cryosphere*, 8(2), 547–569, doi:10.5194/tc-8-547-2014.

Veitinger, J., R. Stuart Purves,and. Sovilla (2016). Potential slab avalanche release area identification from estimated winter terrain: A multi-scale, fuzzy logic approach, *Natural Hazards and Earth System Sciences*, 16(10), 2211–2225, doi:10.5194/nhess-16-2211-2016.

Weiss, a. (2001). Topographic position and landforms analysis, *Poster presentation, ESRI User Conference, San Diego, CA*, 64, 227 – 245.

Westoby, M. J., J. Brasington, N. F. Glasser, M. J. Hambrey,and. M. Reynolds (2012). 'Structure-from-Motion' photogrammetry: A low-cost, effective tool for geoscience applications, *Geomorphology*, 179, 300–314, doi:10.1016/J.GEOMORPH.2012.08.021.

Winstral, A., K. Elder,and. E. Davis (2002). Spatial snow modeling of wind-redistributed snow using terrain-based parameters, *Journal of Hydrometeorology*, 3(5), 524–538, doi:10.1175/1525-7541(2002)003⟨0524:SSMOWR⟩2.0.CO;2.

Wirz, V., M. Schirmer, S. Gruber,and. Lehning (2011). Spatio-temporal measurements and analysis of snow depth in a rock face, *Cryosphere*, 5(4), 893–905, doi:10.5194/tc-5-893-2011.

Wood, S. N. (2006), *Generalized Additive Models*, Chapman and Hall, doi:10.1201/9781420010404.

Xia, K., A. J. Rosakis,and. Kanamori (2004). Laboratory Earthquakes: The Sub-Rayleigh-to-Supershear Rupture Transition, *Science*, 303(5665), 1859–1861, doi:10.1126/SCIENCE.1094022.

Zhang, W.,and. M. Puzrin (2021). Depth integrated modelling of submarine landslide evolution, *Landslides*, 18, 3063–3084, doi:10.1007/s10346-021-01655-z.

Zhang, W., B. Klein, M. F. Randolph,and. M. Puzrin (2021). Upslope Failure Mechanisms and Criteria in Submarine Landslides: Shear Band Propagation, Slab Failure and Retrogression, *Journal of Geophysical Research: Solid Earth*, 126(9), doi:10.1029/2021JB022041.